博士論文

Shape and Optical Parameters Determination of Thin Film Objects

(薄膜物体の形状と光学パラメータの推定に関する研究)

by

Yoshie Kobayashi
小林由枝

A Doctoral Dissertation

Submitted to the Graduate School of
the University of Tokyo

in Partial Fulfillment of the Requirements
for the Degree of
Doctor of Information Science and Technology

December 2015

Thesis Supervisor: Yoichi Sato　佐藤　洋一

Committee:

Takeshi NAEMURA (Chair)
Katsushi IKEUCHI
Kiyoharu AIZAWA
Takeshi OISHI
Toshihiro YAMASAKI
Yoichi SATO

Supervisor:

Yoichi Sato

Abstract

Modeling shapes and appearances of real world objects is one of the important research topics in computer graphics and computer vision fields. Such modeling results are widely used to games, movies and cultural heritage digitization to name a few. Appearances of many objects include several complex reflectance properties such as scattering, absorption, diffraction, refraction and interference. These properties make it difficult to model the shapes and appearances of such objects.

Interference is one of the most intractable effects since its color varies iridescence along the viewing and lighting directions. Various objects have interference optical properties, such as laminated materials, soap bubbles and oil films. Yet, modeling shapes and appearances of these objects with interference effects would be useful for diverse applications in industry, biology, archeology and medicine. For example, realizing the digitization of thin film objects, we can obtain more realistic appearance of new coating products in digital space. Several Japanese art crafts such as Tamamushi Shrine were made of wings of green buprestids with interference.

The interference effects are due to interactions between incoming and reflected lights, and depend mainly on geometric parameters such as film thickness and refractive indexes. Once we can establish a method to estimate those geometric parameters, we can generate appearances of such objects relatively easily using a rendering program.

For appearance modeling, it is necessary to estimate those geometric parameters from a non-planar surface. For example, appearance modeling of a heritage object requires a nondestructive measurement method. We cannot peel out a part of the surface from a priceless heritage asset for modeling purposes. Such objects often have a complicated shape with non-planar surfaces. Thus, we have to establish a method to measure those geometric parameters without destroying or deforming original non-planar objects.

The goal of this dissertation is to model thin film objects. To achieve this goal, we have three issues. The first issue is how to estimate refractive index and film thickness using hyper-spectral images. In optics fields, several methods were proposed to estimate film thickness, however these method estimate film thickness on one point of object surfaces at once. So it is difficult to represent spatially varying appearances by these methods. In addition, these methods assume that a refractive index is known. Therefore, we should develop a novel method to estimate a refractive index and spatially varying

film thickness to model a thin film accurately.

The second issue is how to reconstruct shapes of thin film objects. The appearance of thin film objects is deeply depend on not only optical parameters but also shapes. However, conventional methods can not reconstruct shapes of thin film objects, because appearances of thin film objects changes drastically like rainbow along viewing and liting directions. Therefore, we need a novel method to reconstruct shapes of thin film objects.

The third issue is a new equipment to measure reflectance of thin film objects. Reflectance of thin film objects can be observed when incoming and reflected angle become equal. So we should illuminate thin film objects from various directions, however it is time consuming. We can acquire whole reflectance at once if we illuminate thin film objects omnidirectionally. Therefore, we develop an omnidirectional illumination environment and measure reflectance of thin film objects at once.

論文要旨

コンピュータビジョンやコンピュータグラフィックス分野において、実世界の物体をモデリングすることは重要な課題となっている。実物体のモデリングはゲームや映画、文化遺産のデジタル保存などに用いられている。しかし、実世界の物体は散乱、吸収、回折、屈折、干渉といった様々な反射特性を持っており、一概にモデリングといっても反射特性によってモデル化が困難なものがある。

様々な反射特性の中でも干渉はその色が光源・視線方向に対して大きく変化することから、モデル化が非常に困難な反射特性の一つである。干渉はラミネートフィルム、シャボン玉や油膜の表面で観測することが出来る。しかし、干渉をモデル化できれば、工業製品、バイオ分野、考古学といった様々な分野で応用が可能であり、干渉のモデル化は非常に有用である。例えば、薄膜を表面に有する物体 (薄膜物体) のデジタル化が行えると、薄膜がコーティングされた物体のより実物体に近い見えがデジタルデータとして再現できる。一般的に薄膜干渉は入射光と反射光の間で生じる光の強めあい、弱めあいと膜厚や屈折率といった光学的なパラメータによって生じるものである。これらのパラメータを推定することが出来れば、レンダリングプログラムによって再構成することは比較的容易に実現できる。

薄膜物体をモデル化するには、3 次元形状を有する薄膜物体から膜厚と屈折率を推定する必要がある。貴重な文化遺産では、従来手法のモデル化のように表面を削り取って反射特性の計測を行うことはできないため、文化遺産のデジタル化においては、複雑な形状を有する文化遺産を非破壊で計測するためである。そのため、文化遺産の非破壊なモデル化手法として複雑な三次元形状を有する薄膜物体から膜厚や屈折率といったパラメータを推定する手法が必要となる。

本論文では薄膜物体のモデル化手法について提案する。提案手法では主に以下の 3 点について取り組んだ。まず、平面の薄膜物体の屈折率、膜厚をハイパースペクトル画像を用いて、画像ベースで推定する手法を提案する。次に、複雑な三次元形状を有する薄膜物体の形状、屈折率、膜厚をハイパースペクトル画像、RGB 画像それぞれを用いて推定する手法を提案する。最後に、三次元形状を有する薄膜物体のスペクトル画像や RGB 画像を計測する際に、対象となる薄膜物体に様々な方向から光源を照射し、計測するための装置を開発する。

Acknowledgements

First of all, I would like to thank my advisor Prof. Katsushi Ikeuchi for strong support and encouragement. I have greatly benefited from the knowledge and ideas through many meetings and discussions. He gave me the great opportunity of research experiences to think hard about the essence of problems. I feel honored to be a member of the Computer Vision Laboratory.

I also would like to express my gratitude to my supervisor Prof. Yoichi Sato. He gave me so kind support even though I joined to Sato Laboratory last one year of my doctoral course.

I owe my deepest gratitude to Dr. Tetsuro Morimoto(Toppan Printing Co. Ltd.) , Prof. Imari Sato(National Institute of Informatics), Prof. Yasuhiro Mukaigawa(Nara Institute of Science and Technology), and Dr. Takao Tomono(Toppan Printing Co. Ltd.) . They have always allowed me to discuss and provided me helpful advice and ideas. Through the corroborative research with them, I have learned how they carefully consider and approach research issue.

I am also very grateful to Toppan Printing for making my Ph. D. study possible by the financial support, providing devices and material objects.

I would like to thank the members of the committee, Prof Takeshi Naemura, Prof. Kiyoharu Aizawa, Prof. Takeshi Oishi, Prof. Toshihiro Yamasaki for providing ideas and advice on this thesis. I also would like to express my gratitude to Prof. Kiyoharu Aizawa and Prof. Yoshihiro Yamasaki again for discussing my research at advisor meetings. I also would like to thank Prof. Takeshi Oishi again for supporting research environment.

Many thanks to the current and former members of Ikeuchi and Oishi Laboratory. I could spend so wonderful time and have research environment at laboratory. They always allow me to discuss research problems and support me at my difficult times.

I also appreciate to Masataka Kagesawa, Kiminori Hasegawa, Keiko Motoki, Yoshiko Matsuura, Yamaba Mikiko, and Yuko Nishine for kindness supports.

I would like to thank Dr. Joan Knapp and Dr. Patricia Knapp for english proofreading of my manuscripts.

Finally, it would have been impossible to have my research career without the love, understanding, and support of my parent, Shigeo, Kiyoko, and my grandmother, Kazuko. This dissertation is dedicated to them.

December 2015

Contents

List of Figures

List of Tables

Chapter 1

Introduction

1.1 Background

Motivation

There are various cultural heritages in the world which face the danger of deterioration by collapse, weathering, and so on. Several projects were carried out to protect these cultural heritages by recording them as digital data. For example, Stanford's Michelangelo Project[46], IBM's Pieta Project[76], Digital Bayon Project[96], Great Buddha Project[36] are famous projects. Digitized data of cultural heritages is useful not only for preservation but also for conveying to posterity. Exhibiting digital data of cultural heritages as CGs, people will be able to see cultural heritages which have already been deteriorate. We can also show these data as internet contents, and then people can see and learn cultural heritages accurately even though people are in a distant place from cultural heritages.

3D modeling needs shapes, and appearances. Usually, 3D shapes are acquired by a laser range sensor. The laser range sensor can measure 3D shape of a target object from one view point by point of cloud data, so we need to measure from several view points to acquire the whole shapes of a target object. Appearances are generally captured by a digital still camera and mapping to 3D shapes as a texture. Another methods to acquire shapes and appearances simultaneously are binocular stereo[35, 77, 19, 23, 86, 54],multi

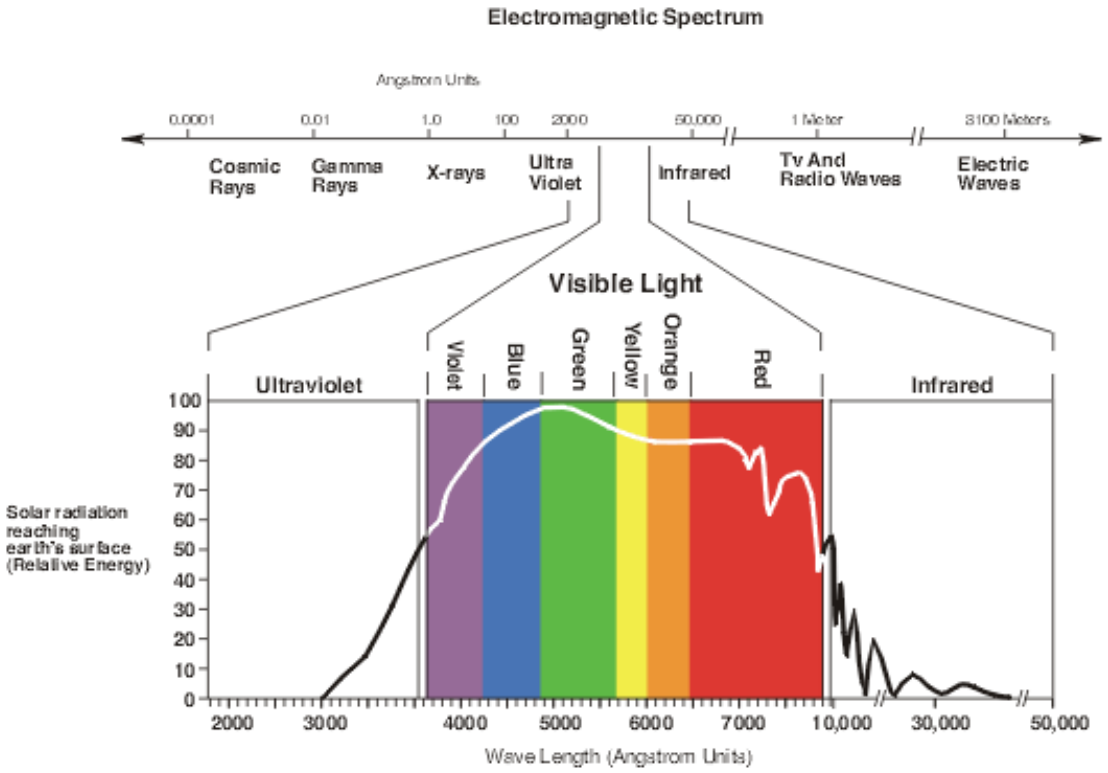

Figure 1.1: Relation between spectral information and RGB color space.

view stereo[44, 18, 47, 68, 81], visual hull[66] and photometric stereo[67, 79, 30]. These methods work well for diffuse surfaces, however, objects in the real world have various reflection which change appearance along viewing and lighting directions such as specularity, isotropy, anisotropy, and scattering.

The reflection along viewing and lighting directions is described by Bidirectional Reflectance Distribution Function (BRDF). Generally, we can acquire BRDF by measuring reflectance of whole viewing and lighting directions[75], but it takes a long time, for example, it takes 33 years assuming that the shutter speed and moving speed of light and a camera is one second. Therefore, methods to shorten measuring time were proposed by using an ellipsoidal mirror[82, 13, 14] or fitting captured appearances to BRDF models[80]. These methods can accurately model objects in the real world, however, there is more complicated reflectance property called "structural color".

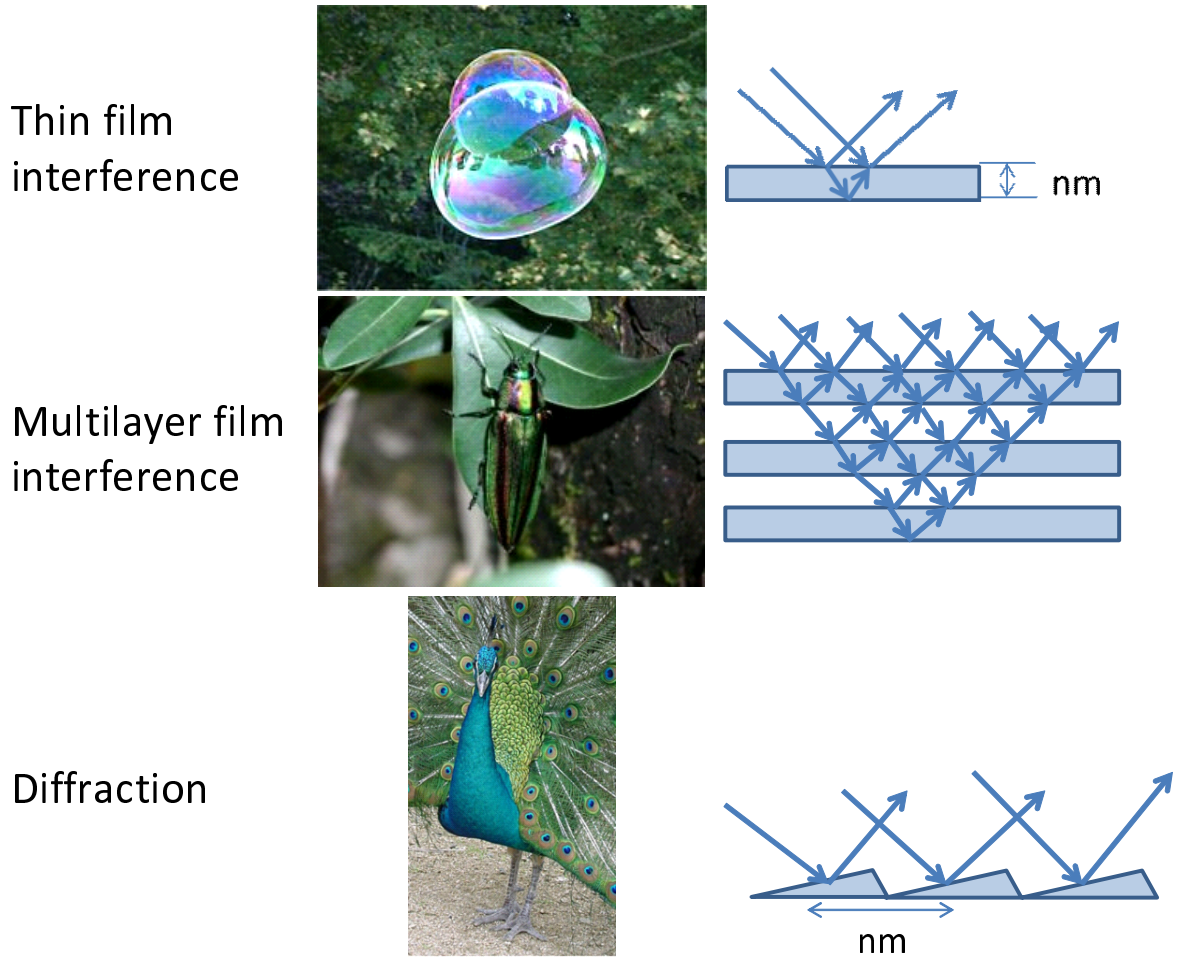

Figure 1.2: Examples of structural color and their physical structure.

The structural color can be observed on soap bubbles, wings of jewel beetles, and feathers of peacocks as shown in Fig. 1.2. These appearances generally change drastically like a rainbow along viewing and lighting directions. This color change is caused by a nano scale structure on an object surface which brings about interference, diffraction grating, refraction and so on. Therefore, this color is called "structural color".

In computer graphics fields, several methods were proposed to render structural color[37, 21, 20, 85, 84, 27, 70]. These methods are based on a physical model and showed that the model can represent structural color realistically by setting optical parameters of structural color manually. The physical model is described by spectral information which handles color as light wave and provides intensity at each wavelength as shown in Fig. 1.1. This reflectance property is called Wavelength BRDF (WBRDF)[34]. To model structural color, we need to acquire shapes and WBRDF[34]. However, method to model structural color objects has not yet proposed. Modeling structural color objects can be applied to many fields including industrial inspection, biological analysis, archeology research, fabrication and so on. Therefore, it is an important and challenging issue for computer vision fields to model objects with structural color.

Goal

The goal of this dissertation is to model a structural color object in the real world. Among structural colors, we focus on thin film interference which is basic structure and changes its color most drastically. We have three issues to achieve our goal.

The first issue is the estimation of optical parameters which have a deep effect on reflectance property of a thin film object. Optical parameters of a thin film are refractive indexes and film thickness. In optics fields, film thickness can be acquired by ellipsometry or interference spectroscopy. These methods acquire the film thickness on only one point at once, and then it is time consuming to acquire the spatially varying film thickness on the object surface. Therefore, it is difficult for these methods to represent spatially varying appearances. Furthermore, in these methods, a refractive index is usually known to estimate film thickness stably. In this dissertation, we propose a method to estimate film thickness distribution by using hyper-spectral images. We also estimate the refractive index and film thickness simultaneously.

The second issue is the shape reconstruction of thin film objects. As mentioned in the previous paragraph, not only optical parameters but also shapes are deeply dependent on appearances of thin film objects. In addition, it is difficult for conventional methods such as ,multi view stereo[44, 18, 47, 68, 81], visual hull[66] and photometric stereo[67, 79, 30] to apply to thin film objects because the color of a thin film changes drastically along viewing and lighting directions, then we can not take a corresponding point. Therefore, it is so challenging an issue to reconstruct shapes of thin film objects for reconstructing and analyzing reflectance properties of thin film objects. In this dissertation, we propose a novel method to reconstruct the shapes of thin film objects focusing on characteristics of the extremal intensity of a thin film reflectance.

The third issue is new equipment to measure reflectance of thin film objects. The reflection of thin film objects can be observed when incoming and reflected angles become equal. We can acquire whole reflectance at once if we illuminate thin film objects omnidirectionally. Therefore, we develop an omnidirectional illumination environment and measure reflectance of thin film objects at once.

1.2 Related Work

In this section, we explain the previous works related to structural color, shapes and appearance acquisition, and optical parameters estimation of a thin film. First, we introduce biological approaches to analyze structure of natural objects which have structural color. These methods showed important issues to fabricate structural color. Second, we explain shapes and appearances estimation methods in computer vision fields. We mention approaches and target of these methods to reveal the difference of the target in this dissertation:thin film objects. Third, we introduce methods to render structural color based on physical models. These works showed important parameters to reconstruct appearances of structural color objects. Finally, we explain methods to estimate film thickness as rendering methods pointed out that it is an important parameter for appearance modeling of thin film objects.

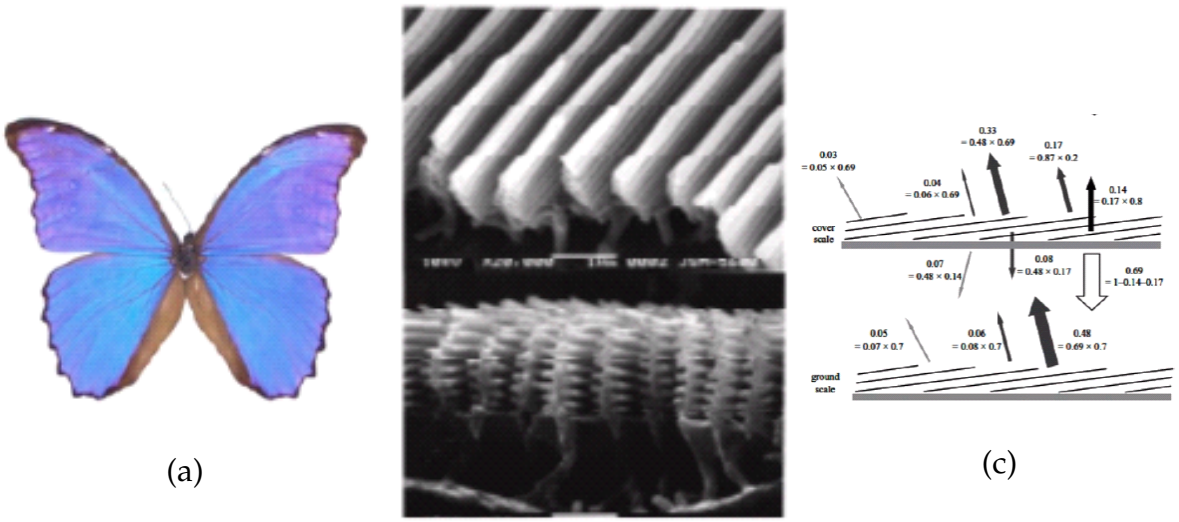

(a) (b) (c)

Figure 1.3: Images from Kinoshita et al. Science 2008. (a) Example of morpho butterfly. (b) Structure of morpho butterfly observed by electron microscope. (c) Structure diagram of morpho butterfly.

1.2.1 Analysis of Structural Color in Biological Research

In biological research, there are several researches to analyze physical structure of objects which have structural color. The structural color is caused by microscopically structured surfaces such as scattering, interference, diffraction and so on. Usually, these structures change color drastically along viewing and lighting directions, like soap bubbles. Analyzing these structures is important to understand reflection properties of structural color.

In the natural world, we can observe structural color on various object surfaces, for example, feathers of pigeons and peacocks, wings of jewel beetles and the morpho butterfly and so on. Kinoshita et al.[95, 39, 41, 61, 90, 91, 89, 65] analyzed the micro structure of feathers of pigeons and peacocks, wings of the morpho butterfly and so on by the electronic microscope. They analyzed that structures of these objects are combinations of interference, diffraction grating, and scattering. For example, the feather of peacock consists of multi-layer thin film and diffraction grating. The color of wings of a molpho butterfly is caused by multi-layer interference, diffraction grating, and scattering.

These analysis results ware applied to some devices. Saito et al.[98] developed a device which has the same spectra as a morpho butterfly. This device is able to color like molpho butterfly by reflecting incoming light on its surface. For further application, Yue et al.[87] developed a novel display with hydrogels which change transmitted wavelength by pressure to hydrogels.

1.2.2 Shape and Appearance Reconstruction

In computer vision fields, there are several methods to estimate shapes and appearances simultaneously. Multi-view stereo [44, 18, 47, 68, 81] uses several images captured from various view points with fixed target objects. This method explores corresponding points among images, and then estimates depth from parallax. Recently, this method was applied to large scale outside objects to digitize cultural heritages from internet images [81, 48, 74, 57]. However, the reconstructed appearance of an outdoor scene has influences of illumination, thus appearances change with different illumination effects.

Several methods to remove illumination effects from RGB images [52, 17] were proposed, but these methods became unstable by noise or metamerism. Metamerism is color matching among different color under a certain illumination in an RGB space. However, it can be recognized as different color in a spectrum space. To remove illumination effects more stably, methods using spectral information were proposed[72, 33, 8, 55, 15]. Spectral information handles color as light wave and provides intensity at each wavelength. As shown in Fig. 1.1, we can get RGB information through RGB filter whose spectrum has each peak of Red, Green, and Blue colors. So spectrum has much color information than RGB information, then we can recognize the different color under metamerism by spectrum. However, these methods can get reflectance from one light and view direction. Usually, reflectance changes along light and view directions, so we need to estimate reflectance among whole light and view directions to get the accurate model of target objects.

To reconstruct more accurate appearances, we can use photometric stereo methods. Photometric stereo methods estimate shapes, and BRDF which describes appearance to light and view directions. Silver[67] and Woodham [79] proposed a method for diffuse surfaces whose reflectance property is defined as Lambertian reflection [45]. They

determined surface orientation using images under illumination of different directions. Ikeuchi et al. [30] reconstructed shapes with a single image using occluding boundary and reflectance which becomes a cosine curve along the zenith angle. However, objects in the real world have various reflection properties such as specular, isotropic, and anisotropic reflection, so several methods were proposed to apply to these reflections [7, 26, 29, 10, 83, 28]. Generally, they capture images under a controlled environment, like a dark room, so they can not measure large scale objects such as buildings.

Outdoor photometric stereo was proposed for application to large scale objects [32, 1, 92]. However, in the outdoors it takes a long time to capture data from more than three different illumination directions because the Sun moves on an elliptic orbit. So photometric stereo with laser range sensor or kinect [97, 93, 63] was proposed to make measurement costs smaller.

To handle more complicated reflectance properties, the methods of reconstructing shapes of transparent objects were proposed. For transparent objects, based on polarization analysis, Wolff et al.[78], Saito et al.[51] and Miyazaki et al.[11][12] estimated the shapes of transparent objects. They used polarization analysis in basic idea. Inoshita et al. [94] reconstructed translucent objects like white plastics by fitting with a single scattering model [69].

1.2.3 Model and Acquiring Method of Reflectance Properties

In computer graphics, several methods were proposed to represent reflectance properties which define appearances of target objects. There are various parametric models to represent various appearances such as diffuse, specular, and isotropic surfaces [16, 5, 9, 75, 56, 2, 59, 73]. The basic model is the Phong model [59]. The representation is simple and practical, but this model is not physically accurate. To represent physically accurate reflectance, Torrance-Sparrow model [73] was proposed. However, this model has complicated parameters. Ward et al. [75] proposed a novel and practical model based on Torrance-Sparow model. Lafortune et al. [16] proposed a model which can represent more general reflectance. These models do represent BRDF well, however it is difficult to reconstruct BRDF of non-planar surfaces.

Image based BRDF measurement [64] was proposed to acquire BRDF of non-planar surfaces. Borshukov et al. [6] modeled human faces realistically which have compli-

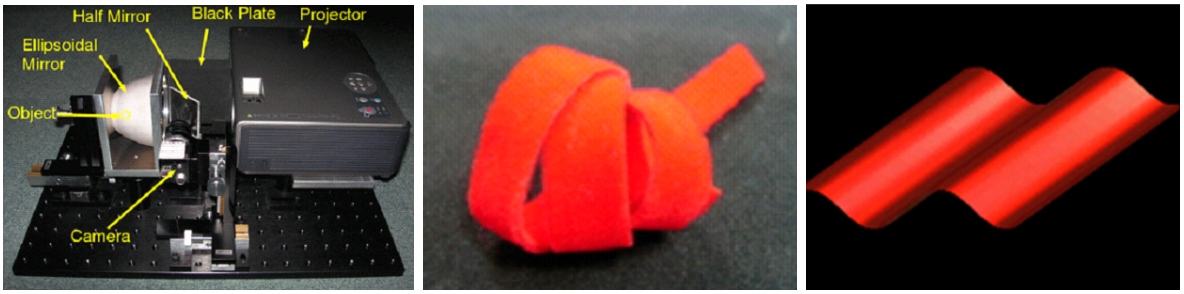

(a) (b) (c)

Figure 1.4: Measurement device using ellipsoidal mirror[82]. (a) shows setup of device.(b) shows red velvet. (c) shows a rendering result of red velvet which reectance property is measured by device shown in (a).

cated combinations of diffuse and specular reflections. BRDF can represent only one reflectance property. Therefore, if target surfaces consist of more than two reflectances, BRDF can not represent it well. To represent BRDF for each reflectance, Spatially Varying BRDF (SVBRDF) [22] was proposed. Holroyd et al. [49] and Dana et al. [38] control the illumination and view directions by the sequential and mutual positioning of the light, sensor, and sample. Mukaigawa et al. [82] and Dana et al. [13, 14] used mirrors to simultaneously acquire complicated reflectance properties, but data from this method is a high dimension to handle. Dong et al. [80] developed a new hand-held BRDF capturing device, and acquired the SVBRDF using the boosting technique. Morimoto et al. [71] analyzed the layer structure of painting material. However, these methods' main concern is about the reflection mechanism; the methods cannot be applied to handle appearance variance in thin film layers.

1.2.4 Rendering Methods of Structural Color

Several structural colors, such as interference diffraction, were realistically rendered as CG. Iwasaki et al.[37] proposed rendering methods for soap bubbles. Imura et al. [50] rendered soap bubbles on real time. Hirayama et al. [21, 20] proposed a method to render multilayer interference. By modeling the micro-structure of CDs, Sun et al. [85, 84] rendered CDs more realistically. Sadeghi et al. [27] rendered rainbow images realistically by ray tracing. Cuypers et al.[70] showed that Wigner distribution

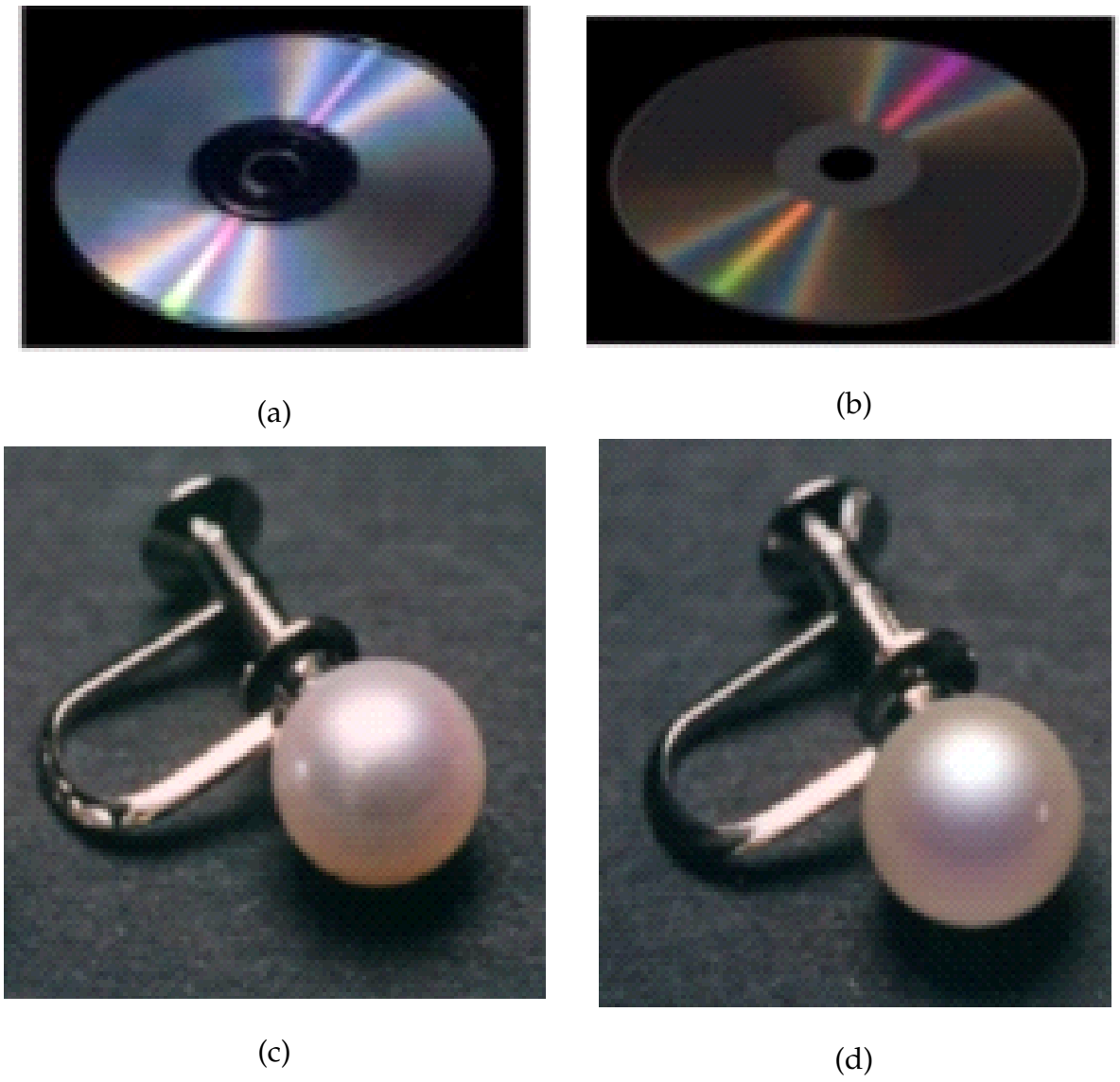

(a) (b)

(c) (d)

Figure 1.5: Real object images and rendering result. (a) and (c) are real objects. (b) and (d) are synthesized images. CD is rendered by Sun et al.'s method, Mother-of-pearl is rendered by Nagata et al.'s method.

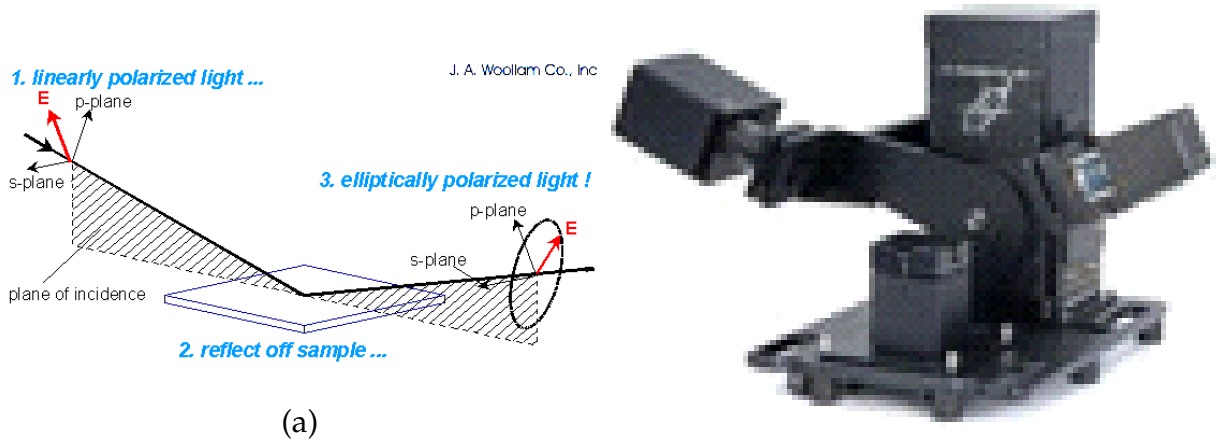

(a) (b)

Figure 1.6: Ellipsometry. (a) Device diagram. (b) Product of ellipsometry from J. C. Woollam Japan.

function can represent the BRDF of diffraction grating as accurately as a physical model. All these methods showed that physical models represent appearance well, but they set optical parameters manually. Therefore, we need to estimate these parameters to reconstruct the appearance.

1.2.5 Film Thickness Estimation in Optics Fields

As mentioned in the previous section, a refractive index and film thickness are important parameters for appearances of thin film objects. Several methods exist for estimating parameters of a physical model, such as a refractive index and film thickness for a planar patch. Interference spectroscopy[53] and ellipsometry[3, 31, 4] are representative methods to estimate film thickness with a known refractive index. The ellipsometry is usually most popular for measuring the thin films on a plane substrate. On the other hand, the method is applied to a thin film on a non-planar plastic substrate. There, each layer on the device structure is measured and the measurement is performed on the plane condition [88]. The thin film on plastic sheets is measured in the monitoring of roll to roll process. In this case, the measurement plane is the direction of the length of a cylinder drum [62]. Therefore, we have not seen an example of a non-planar object such as a spherical object or a convex body, etc. Kitagawa [42, 43]

proposed an image-based method, which utilizes RGB values along the film thickness, but the method requires a known refractive index. However, the limitation of this method is that it can only be applied to planar surfaces.

1.3 Overview

The rest of this dissertation is as follows.

In Chapter 2, we propose a method to estimate the refractive index and film thickness of planar objects simultaneously. We focus on a peak wavelength where the spectrum of a thin film has extreme intensity, because we can simply define a refractive index and film thickness at this wavelength. The previous methods only estimate at one point, however, we use hyper-spectral images, then we can acquire distribution of film thickness. We also synthesize appearances from estimated parameters and compare with target objects.

The method in Chapter 2 is difficult to apply to non-planar objects because reflectance is also deeply dependent on the shape of the target object. Therefore, in Chapter 3, we introduce a method to estimate the shapes and optical parameters of thin film objects from reflectance spectra. In the experiment, we set up a rotation table and a spectrometer, and measure reflectance for each angle between the spectrometer and the light source. We evaluate and discuss the accuracy of the estimated incident angle and the optical parameters.

In Chapter 3, we only measure one point for each incident angle because of the limitation of the experimental device. Furthermore, we also only estimate the incident angle, so we can not get the whole shape of the target objects. To solve these problems, we develop novel equipment for measuring the whole reflectance image at once. We also introduce a method to estimate azimuth angle for reconstructing surface normals.

The methods described above need reflectance spectra to reconstruct shapes and appearances. However, acquiring reflectance spectra requires complicated device settings and expensive devices. In Chapter 5, we propose a simpler method to estimate shapes and film thickness using RGB images.

In Chapter 6, we summarize our dissertation to discuss the contribution and future work.

Chapter 2

Refractive Index and Film Thickness Estimation of Planar Objects

2.1 Overview

Refractive indexes and film thickness are important parameters to reconstruct appearances of thin film objects. In optics fields, there are several methods to estimate film thickness such as ellipsometory[3, 31, 4] and interference spectroscopy[53]. However, these methods can measure only one point at once and assume that a refractive index is known. To solve these problems, we propose a method to estimate refractive index and spatially varying film thickness by using hyper-spectral images.

The rest of this chapter is as follows. In Section 2.2, we explain a model of thin film reflectance. In Section 2.3, we introduce a method to estimate a refractive index and film thickness. In Section 2.4, we conduct an experiment to verify the accuracy of our method. In Section 2.5, we discuss the cause of experimental errors. In Section 2.6, we summarize this chapter.

2.2 Reflectance Model

In this section, we explain reflectance model of thin film which is proposed in optics fields. This model can represent appearance of thin film as accurate as real objects as

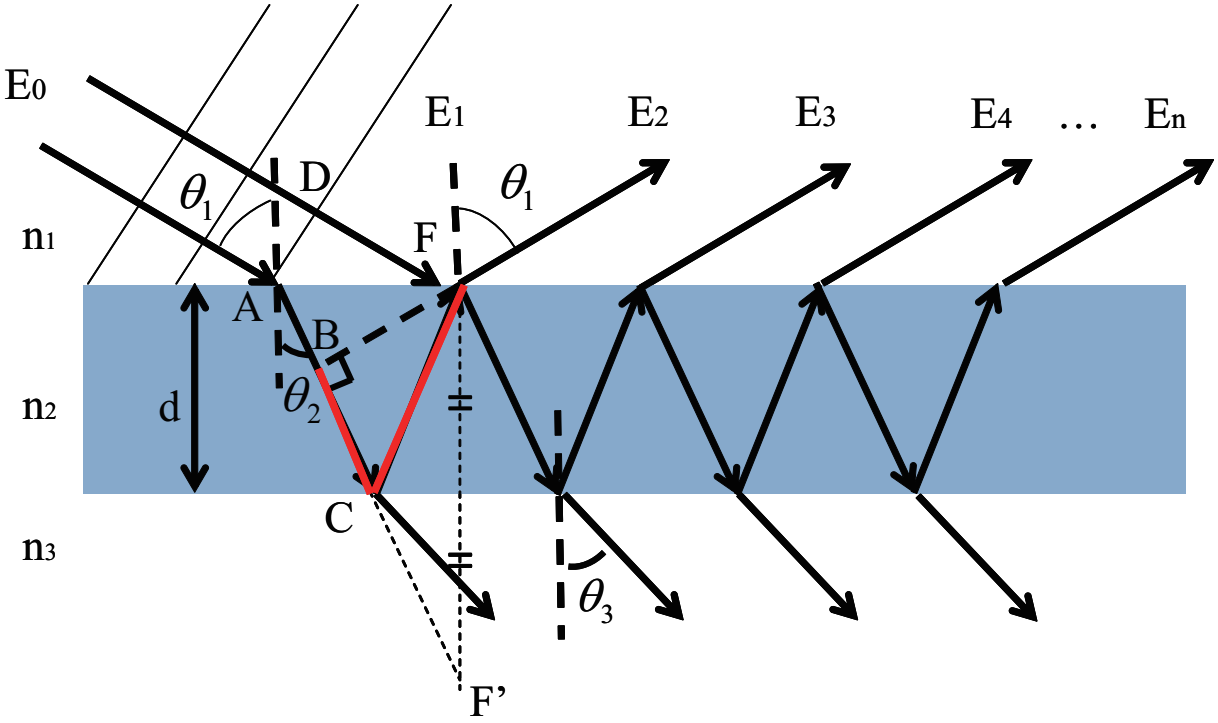

Figure 2.1: Schematic diagram of thin film interference considering multiple reflections. n_1, n_2 and n_3 are refractive indices, d is the film thickness, θ_1 is the incident angle and θ_2 is the refracting angle. θ_3 is the outgoing angle.

shown in previous research[50]. We introduce the definition of reflectance in spectral and RGB information in following.

In optics field, the reflectance model of thin film interference[40] was proposed. In Fig. 2.1, n_1,n_2 and n_3 are refractive indices of the top layer, thin film and bottom layer respectively. θ_1 is the incident angle. θ_2 is the refracting angle. θ_3 is an angle of outgoing light transmitting through the thin film and going into the bottom layer. Here, we ignore the absorption of the light in bottom layers. d is film thickness. Considering

multi-reflection in Fig. 2.1, the observed light E can be defined by .

$$\begin{aligned} E &= E_1 + E_2 + E_3 + E_4 + \cdots \\ &= E_0(r_{12} + t_{12}t_{21}r_{23}e^{i\Delta} + t_{12}t_{21}r_{23}^2 r_{21}e^{2i\Delta} \\ &\quad + t_{12}t_{21}r_{23}^3 r_{21}^2 e^{3i\Delta} + \cdots \\ &= E_0(r_{12} + t_{12}t_{21}r_{23}e^{i\Delta}(1 + r_{23}r_{21}e^{i\Delta} \\ &\quad + r_{23}^2 r_{21}^2 e^{2i\Delta} + \cdots)) \\ &= E_0(r_{12} + \frac{t_{12}t_{21}r_{23}e^{i\Delta}}{1 - r_{23}r_{21}e^{i\Delta}}) \end{aligned} \tag{2.1}$$

where r_{12}, r_{23} and r_{21} are Fresnel reflectance coefficients, t_{12} and t_{21} are Fresnel transmittance coefficients. Δ is the phase difference and is represented by

$$\Delta = \frac{2\pi\varphi}{\lambda} \tag{2.2}$$

Here, incoming light E_0 reflect or transmit on the surface. The phase of reflected light at A does not shift since the light goes from high refractive media to low refractive media. On the other hand , the phase of transmitted at A, reflected at C, and outgoing light at F shifts by π since the light goes from low refractive media to high refractive media. The phase difference depends on the optical path difference between reflected light at A and outgoing light at F. The distance between them is $ACF - DF$. However, the optical difference path φ can be represented $n_2 ACF - n_1 DF$ as shown in Fig. 2.1. Here, the refractive index of air is $n_1 = 1$, and $DF = n_2 AB$.

$$n_2 ACF - DF = n_2 BCF \tag{2.3}$$

Considering symmetrical point F' of F, BCF is equal to $BCF' = 2d\cos\theta_2$. φ is the optical path difference shown as follow in Fig. 2.1.

$$\varphi = n_2 BCF = 2dn_2\cos\theta_2 \tag{2.4}$$

Canceling the incoming light E_0 from Eq. (2.1), we can define the amplitude of the reflectance as follows.

$$\begin{aligned} r &\equiv \frac{E}{E_0} \\ &= r_{12} + \frac{t_{12}t_{21}r_{23}e^{i\Delta}}{1 - r_{23}r_{21}e^{i\Delta}} \end{aligned} \tag{2.5}$$

Substituting $r_{21} = -r_{12}$ and $t_{21}t_{12} + r_{12}^2 = 1$ to Eq. (2.5), the amplitude of reflectance can be rewritten as Eq. (2.6).

$$\begin{aligned} r &= r_{12} + \frac{t_{12}t_{21}r_{23}e^{i\Delta}}{1 - r_{23}r_{21}e^{i\Delta}} \\ &= \frac{r_{12} - r_{12}r_{23}r_{21}e^{i\Delta} + (1 - r_{12}^2)r_{23}e^{i\Delta}}{1 - r_{23}r_{21}e^{i\Delta}} \\ &= \frac{r_{12} + r_{23}e^{i\Delta}}{1 + r_{23}r_{12}e^{i\Delta}} \end{aligned} \tag{2.6}$$

The reflectance is given by the square of the absolute value of Eq. (2.6).

$$R = \left| \frac{r_{12} + r_{23}e^{i\Delta}}{1 + r_{23}r_{12}e^{i\Delta}} \right|^2 \tag{2.7}$$

In this paper, we define this reflectance model Eq. (2.7) as reflectance of thin film objects.

Fresnel reflection coefficients r_{12} and r_{23} are defined for perpendicular polarization (S-wave) and parallel polarization (P-wave) as follows.

$$r_{12}^s = \frac{n_1 \cos\theta_1 - n_2 \cos\theta_2}{n_1 \cos\theta_1 + n_2 \cos\theta_2} \tag{2.8}$$

$$r_{12}^p = \frac{n_2 \cos\theta_1 - n_1 \cos\theta_2}{n_2 \cos\theta_1 + n_1 \cos\theta_2} \tag{2.9}$$

$$r_{23}^s = \frac{n_2 \cos\theta_2 - n_3 \cos\theta_3}{n_2 \cos\theta_2 + n_3 \cos\theta_3} \tag{2.10}$$

$$r_{23}^p = \frac{n_3 \cos\theta_2 - n_2 \cos\theta_3}{n_3 \cos\theta_2 + n_2 \cos\theta_3} \tag{2.11}$$

The reflectance in RGB space is represented by multiplication of camera sensitivity and reflectance spectra Eq. (2.5) as follows.

$$R_{RGB} = \int S_{RGB}(\lambda) R(\lambda) d\lambda \tag{2.12}$$

$S_{RGB}(\lambda)$ is camera sensitivity function. $R(\lambda)$ is reflectance spectra. We define Eq. (2.5) and (2.12) as reflectance of thin film in this paper.

2.3 Optical Parameters Estimation

The refractive index and film thickness are important parameters to determine appearances of thin film objects. Therefore, we need to estimate these parameters to

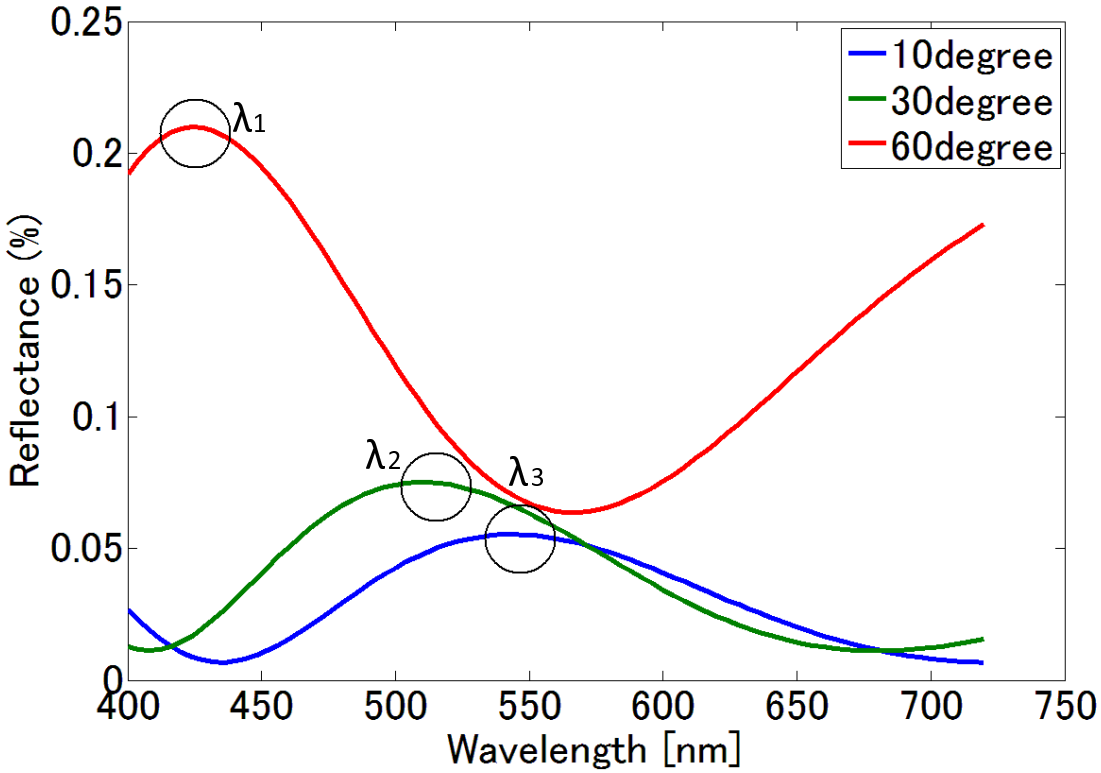

Figure 2.2: Reflectance of Thin Film Interference at 10, 30, and 60 degrees Wavelengths of areas enclosed by circles are peak wavelengths. The refractive index of this reflectance is 1.37 and the film thickness is 400 nm. Blue, green, and red lines are reflectance at 10, 30, and 60 degree, respectively.

reconstruct appearances of thin film objects. In this section, we propose a novel method to estimate these parameters using hyper-spectral images.

We focus on the peak wavelength which is enclosed by circles in Fig. 2.2. At peak wavelength, the phase difference becomes an integral multiple of π, and by formula deformation, the optical path difference also becomes an integral multiple of the peak wavelength. By deforming optical path difference at the peak wavelength, we can easily define the refractive index and film thickness.

We estimate the following procedure. Firstly, we estimate the refractive index with the peak wavelength which enhances the spectrum intensity. Secondly, we pick up the candidate of the film thickness with the estimated refractive index and determine by the least mean square error between the reflectance model and the measured reflectance. The order of this method is $O(ml)$. l is the number of candidates of the film thickness.

We have three assumptions for our method. First, the incident angle is known. As mentioned in Chapter 2, parameters of appearance are not only the refractive index and film thickness but also an incident angle. If all incident angles of measured reflectance are unknown, the number of parameters becomes larger than that of measured reflectance spectra, and then it is difficult to estimate from equation of reflectance spectra. Second, the refractive index is consistent at all the points of a reflectance image. Third, the thin film thickness is different at each pixel but changes smoothly.

2.3.1 Refractive Index Estimation

In this section, we explain a method to estimate a refractive index. The optical path difference can be rewritten as Eq. (2.13) with an incident angle θ_1 by Snell's law.

$$\varphi = 2d\sqrt{n_2^2 - \sin^2\theta_1} \tag{2.13}$$

where d is film thickness, n_2 is a refractive index and θ_1 is an incident angle. It becomes an integral multiple of the peak wavelength and rewritten as follows.

$$m\lambda = \varphi \tag{2.14}$$

Assuming a refractive index and film thickness are consistent at two different incident angles, θ_{1_1}, θ_{1_2}, the optical path difference is integral multiple of the peak

wavelengths shown in Eq. (2.15) and (2.16).

$$m\lambda_1 = 4\pi d\sqrt{n^2 - \sin^2\theta_{1_1}} \tag{2.15}$$

$$m\lambda_2 = 4\pi d\sqrt{n^2 - \sin^2\theta_{1_2}} \tag{2.16}$$

where m is a natural number, θ_{1_1} and θ_{1_2} are incident angles, and λ_1, λ_2 are peak wavelengths. Combining Eq. (2.15) and (2.16), the refractive index is defined as Eq. (2.17).

$$n_2 = \sqrt{\frac{\lambda_2^2\sin^2\theta_{1_1} - \lambda_1^2\sin^2\theta_{1_2}}{\lambda_2^2 - \lambda_1^2}} \tag{2.17}$$

2.3.2 Film Thickness Estimation

We also introduce the estimation method for the film thickness with the estimated refractive index. By combining Eq. (2.15) and (2.16), the film thickness, d, is defined by Eq. (3.12).

$$d = \frac{m\lambda_{1,2}}{2\sqrt{n_2^2 - sin^2\theta_{1_{1,2}}}} \tag{2.18}$$

In Eq. (3.12), the natural number, m, is unknown; unless we determine the natural number, m, we are not able to get the film thickness. As shown in Eq. (2.19), we determine m by minimizing the squared error between the measured reflectance and the reflectance model shown in Eq. (2.7).

$$Arg\min_m \left| \sum_\lambda (R_{model}(\lambda) - R_{measured}(\lambda))^2 \right| \tag{2.19}$$

2.4 Experiment

To evaluate the accuracy of the reconstructed appearance, we conducted an experiment with thin films with known parameters. We investigated the accuracy of the estimated refractive index and film thickness. Using the estimated parameters, we evaluate the color difference and RMSE along an incident angle. We also simulate the thin film appearance by CG and compare it with real object images.

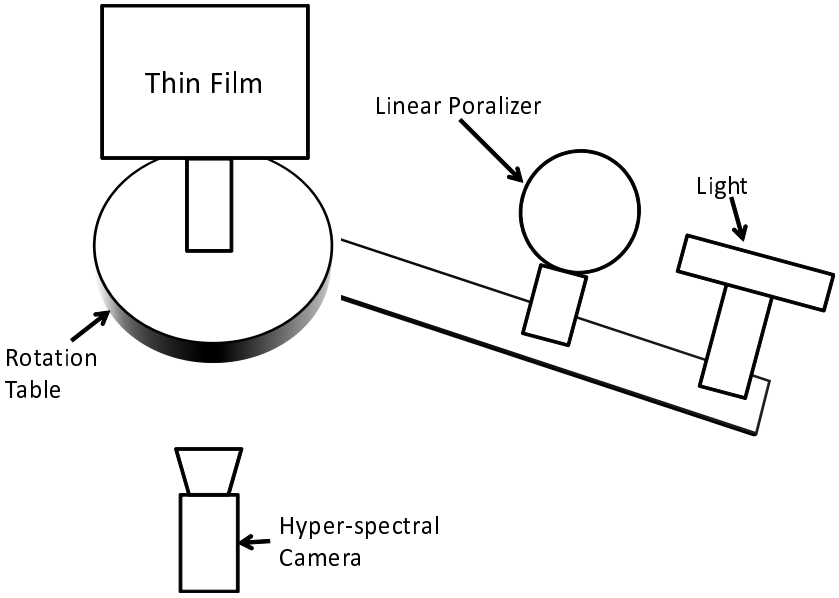

(a) Schematic Diagram of Setup

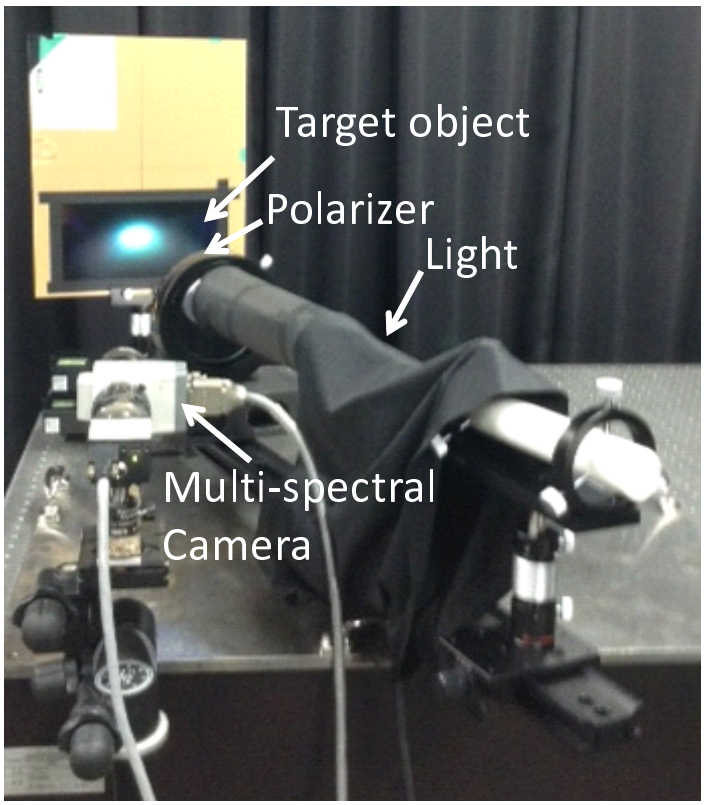

(b) Actual Setup

Figure 2.3: Experimental Setup for Measuring Reflectance of Thin Film (a) shows the schematic diagram of the setup. (b) shows the actual setup.The distance between light and thin film is 0.8[m]. The distance between camera and thin film is 0.6[m].

(a) Physical Vapor Deposition

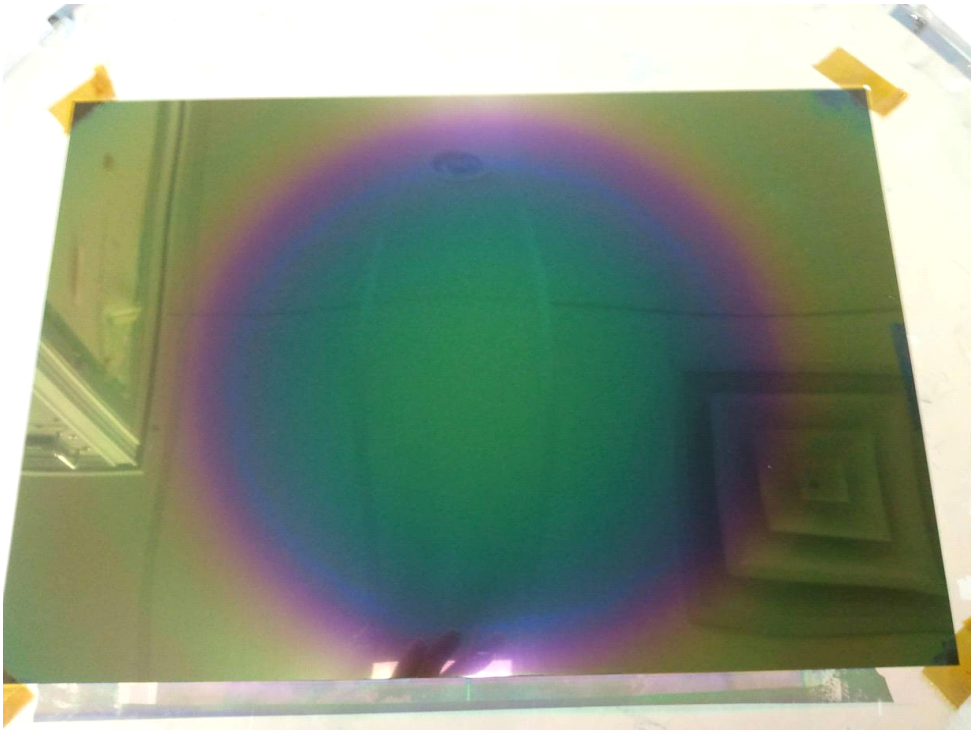

(b) 600 nm MgF_2 in thickness

Figure 2.4: (a) physical vapor deposition to evaporate metal on PET film and (b) Evaporated film thickness of MgF_2 is 600 nm.

2.4.1 Experimental Setup

Table 2.1: Estimated refractive index and average film thickness of Fig. 5.8. The BRDF error is the average color difference among all incident angles at all pixels of Fig. 5.8. RMSE is average among all incident angles of 5.8.

Target	Ground truth of refractive index	Estimated refractive index		
Sample 1	1.370	1.374		
Sample 2	1.370	1.367		
Sample 3	2.370	2.674		
Target	Ground truth of thickness[nm]	Estimated thickness[nm]	BRDF error	RMSE
Sample 1	400	370	0.72	0.04
Sample 2	600	551	1.21	0.07
Sample 3	500	541	5.63	0.18

The experimental setup is shown in Fig. 2.3. A target object and a light source are attached on the rotation table which adjusts an incident angle. The incident angle is changed from 10 to 50 degrees by 10 degrees. The reflectance of the thin film is measured by the hyper-spectral camera which transmits linearly polarized light. The hyper-spectral camera is composed of Liquid Crystal Tunable Filter (vari spec cri) and the monochrome camera. The LCTF can change its transmitted wavelength electrically. The viewing angle of the camera is about 30 degrees. The band width in this experiment is 4 [nm]. We set a linear polarizer and LCTF to transmit only S-wave, so the hyper-spectral camera observes only S-wave reflectance.

As a target object, we use three samples of the thin film where the metal is evaporated onto the polyethylene terephthalate (PET) film.

- Sample 1 Material: MgF_2 Thickness: 400 nm
- Sample 2 Material: MgF_2 Thickness: 600 nm
- Sample 3 Material: ZnS Thickness: 500 nm

To evaporate these materials as the above film thickness, we use the physical vapor deposition as shown in Fig. 2.4 (a). The physical vapor deposition can control the thickness by the Quartz Crystal Microbalance. The example of evaporated thin film is shown in Fig. 2.4 (b).

2.4.2 Evaluation

Fig 5.8 (a), (c) and (e) are the distribution maps of estimated film thickness of each sample. We also show the error maps of estimated film thickness in Fig. 5.8 (b), (d) and (f). The error is calculated by $\mid d_{true} - d_{estimated} \mid$. In Table 2.1, the estimated refractive index and the average film thickness of Fig. 5.8 (a), (c) and (e) are shown. The ground truth of refractive indexes in Table 2.1 which is acquired from the material information. Comparing these data the error of the refractive index is approximately 0.02 for Sample 1 and Sample 2. It becomes 0.30 for Sample 3. The error of average film thickness is about 30 nm and 50 nm for Sample 1 and Sample 2, respectively. It is about 40 nm for Sample 3.

Table 2.1 also shows the average color difference and RMSE among all incident angles of all the reflectance image pixels. The color difference is defined as Eq. (2.20).

$$\Delta E^*ab = \sqrt{(\Delta L^*)^2 + (\Delta a^*)^2 + (\Delta b^*)^2} \tag{2.20}$$

Table 2.2 shows the levels of color differences; human eyes perceive how different two colors are. The difference of Sample 1 and Sample 2 is 0.72 and 1.21, respectively. This is slightly different as shown in Table 2.2. It becomes 5.63 for Sample 3, and this is an appreciable difference.

We also show the RMSE in Table 2.1. The RMSE is calculated by Eq. (2.21).

$$RMSE = \sqrt{\sum_{\lambda} (R_{true}(\lambda) - R_{estimated}(\lambda))^2 / N} \tag{2.21}$$

N is the dimension of the reflectance spectra. The reflectance is not greater than 1.0. The RMSE of Sample 1 is 4 % and that of Sample 2 is 7 %. In case of Sample 3, it becomes 18 %.

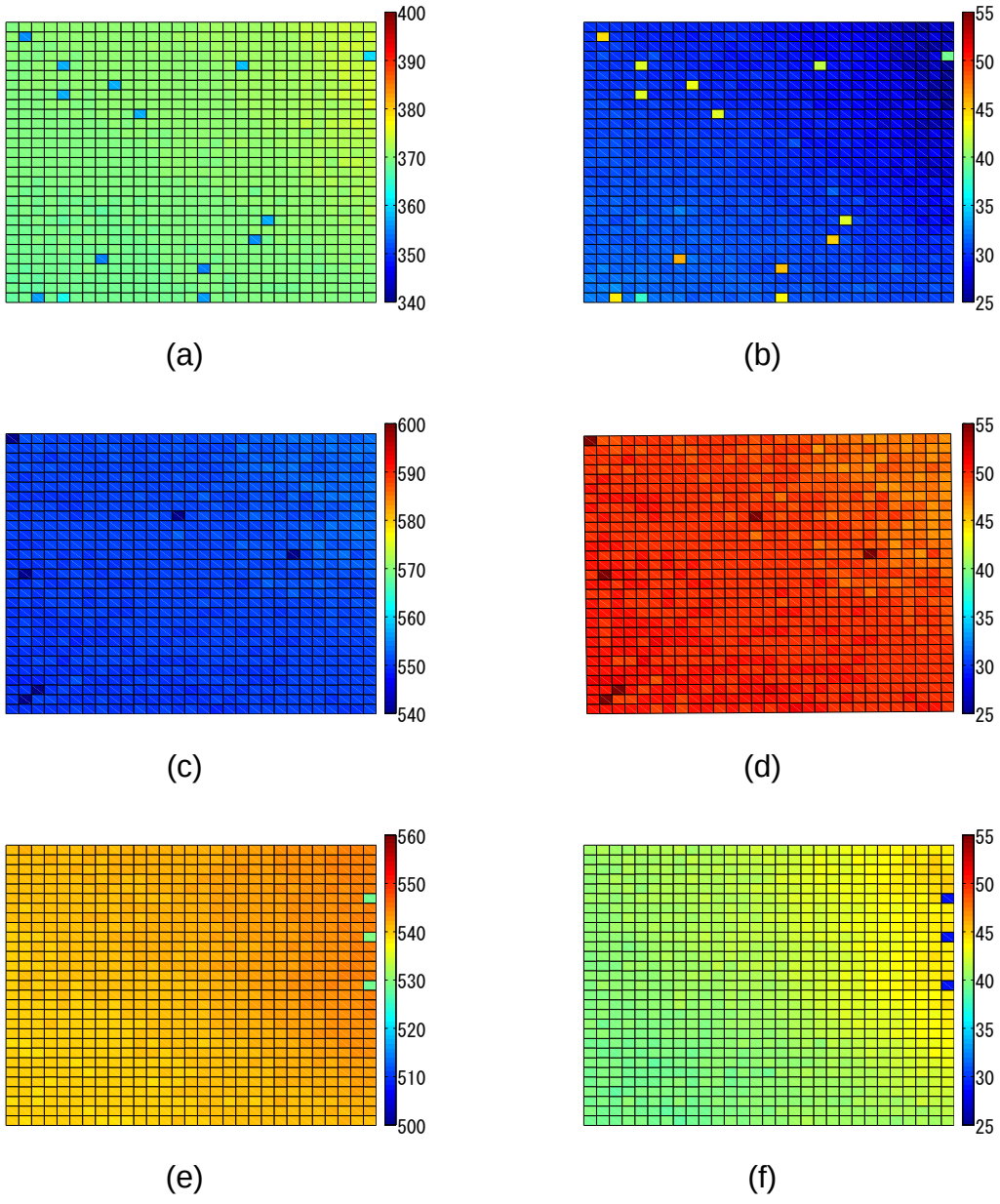

Figure 2.5: Images on upper side are distribution maps of the estimated film thickness of each target. Images on bottom side are the error maps of the estimated film thickness. (a) and (d) are distribution maps for Sample 1 (b) and (e) are distribution maps for Sample 2 (c) and (f) are distribution maps for Sample 3.

2.4.3 Rendering image

We render CG images with the estimated refractive indexes and film thickness in Table 2.1. The renderer is PBRT [58]. The right side images of Fig. 2.6 show rendering images. In these images we use the environment map and Teapot as a rendering object. We also show the target object images on the left side of Fig. 2.6. Comparing the images on the left and right sides, the color change is very similar in the case of Sample 1 and Sample 2. The rendering image of Sample 3 is slightly different from the color of the real object because of the estimation error of BRDF parameters.

Table 2.2: Level of Difference or Distance among Two Color

Level of color difference	ΔE^*ab
trace	0 ~ 0.5
slight	0.5 ~ 1.5
noticable	1.5 ~ 3.0
appreciable	3.0 ~ 6.0
much	6.0 ~ 12.0
very much	over 12.0

2.5 Discussion

In the previous section, the film thickness error of Sample 2 is the largest. However, the color difference and RMSE are small enough among Sample 1 and Sample 2. Regarding Sample 3, the color difference is appreciable and RMSE becomes about 18 %. In this section, we discuss the reason for these errors.

Firstly, we discuss the reason why the color difference and RMSE are small enough in spite of the largest thickness error for Sample 2. The error of the color difference and RMSE is due to the optical path difference which causes the color change of the thin film interference. The optical path difference can be defined by the multiplication of the refractive index and film thickness. Comparing with the error of optical path difference, the error of Sample 2 is small enough because the error of the refractive

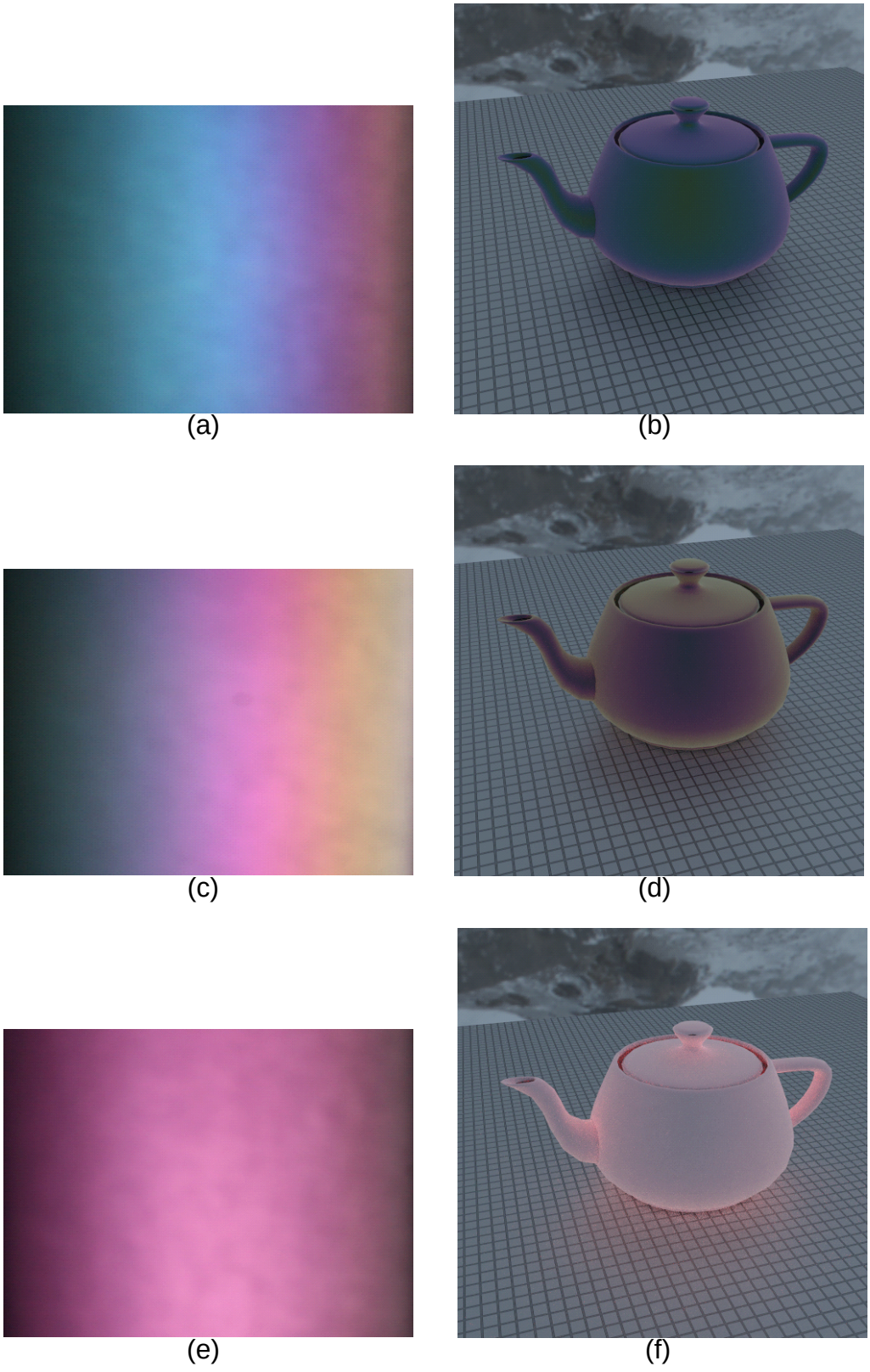

Figure 2.6: Left side of images are real objects on evaporated thin film. Right side images are rendered images with parameters estimated from real objects. (a) MgF_2 400 nm. (b) refractive index:1.374 and film thickness:370 nm (c)MgF_2 600 nm. (d) refractive index:1.367 and film thickness:551 nm (e)ZnS 500 nm. (f) refractive index:2.674 and film thickness:541 nm

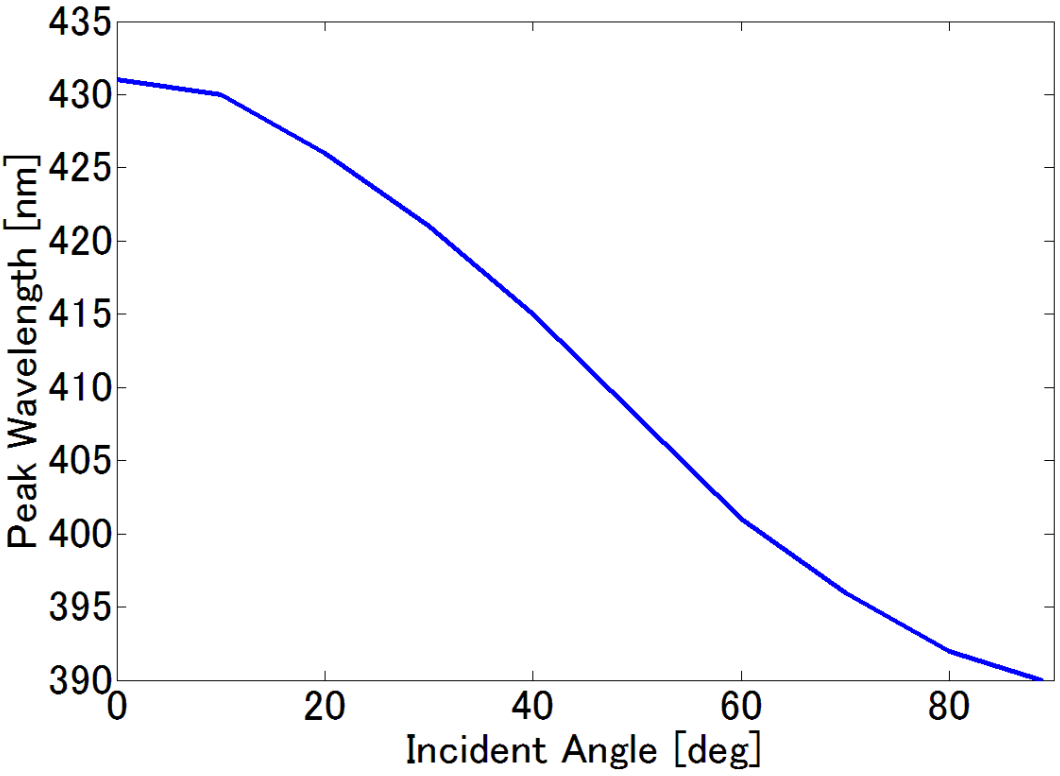

Figure 2.7: Peak Wavelength along Incident Angles. The film material is ZnS. The film thickness is 500 nm.

index is small enough. Therefore, the color difference and RMSE of Sample 2 become smaller.

Secondly, we discuss the reason why the estimation error is so large for Sample 3. The larger estimation error for Sample 3 is due to narrow interval of the peak wavelengths between nearby incident angles. Fig. 2.7 shows the peak wavelengths of Sample 3 along incident angles. As shown in Fig. 2.7, the interval between nearby incident angles by 10 degree is about 4.1 nm. This interval is very close to the wavelength sampling rate by the hyper-spectral camera which is 4 nm in this experiment. Due to the measurement noise of the reflectance, it is difficult to detect the peak wavelength correctly, and then the estimation error of the refractive index and film thickness becomes large. Therefore the estimation error of the BRDF becomes appreciable.

The solution of this large estimation error is to use the hyper-spectral camera whose wavelength sampling rate is small enough compared with the interval of the

peak wavelength between nearby incident angles. However, this solution shows the limitation of our method. From Eq. (2.23), the scale of γ greatly affects the interval of peak wavelengths between nearby incident angles. As shown in Eq. (2.22), the scale of γ is almost determined by the refractive index. The larger the refractive index is, the smaller the rate of change of Eq. (2.22) is. Therefore, there is a limit to the refractive index with high estimation accuracy.

$$\gamma = \sqrt{n_2^2 - \sin^2 \theta_{1_1}} - \sqrt{n_2^2 - \sin^2 \theta_{1_2}} \tag{2.22}$$

$$\lambda_1 - \lambda_2 = \frac{2d\gamma}{m} \tag{2.23}$$

2.6 Summary

This chapter proposed a novel method for estimating BRDF of thin film interference and representing the appearance accurately. In the estimation of the refractive index, we focus on the peak wavelength where the optical path difference is equal to an integral multiple. With the peak wavelength, the refractive index can be defined in a compact way. Using the peak wavelength and the estimated refractive index, we can narrow down the candidates, and easily estimate the film thickness with them. The experiment showed that the accuracy of the proposed method is adequate and it can represent the color change of the thin film well. The results also shows the limitation of our method that we can not estimate with high accuracy with larger refractive index which make the interval of the nearby peak wavelength smaller than the wavelength sampling rate.

Chapter 3

Shape, Refractive Index, and Film Thickness Estimation of Non-Planar Objects Using Hyper-Spectral Images

3.1 Overview

Reflectance of thin film objects deeply concerns object shapes. In Chapter 2, we introduce a methods to estimate refractive index and spatially varying film thickness by using hyper-spectral images. However, this method assumes that a target thin film object has a planar surface. In this chapter, we propose a novel method to estimate not only optical parameters but also shapes by reflectance spectra.

The rest of this chapter consists as follows. In Section 3.2, we propose a method to estimate an incident angle focusing on the characteristics of thin film reflectance. In Section 3.3, we introduce a method to estimate refractive index and film thickness. In Section 3.4, we conduct experiments by the simulation and real data to evaluate the accuracy of our method. In Section 3.5, we discuss the experimental error. In Section 3.6, we summarize this chapter.

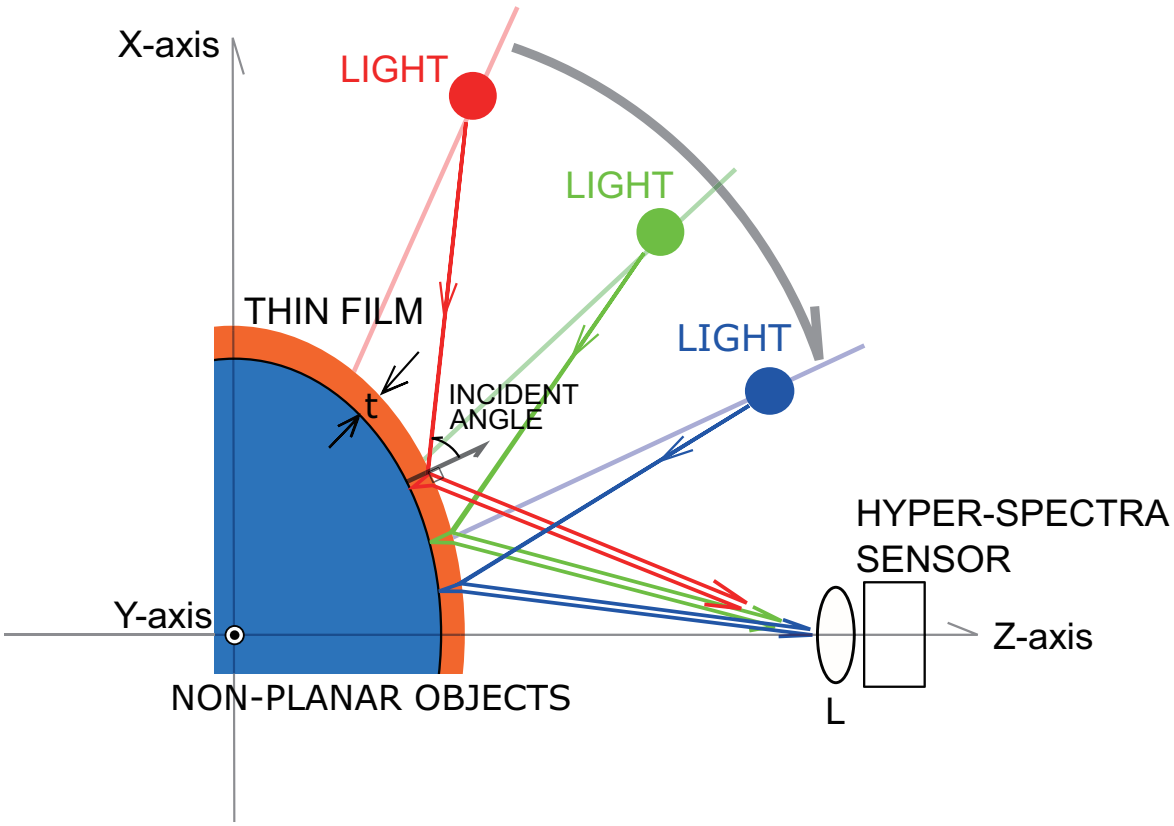

Figure 3.1: Measurement setup. The setup consists of a white light source, a rotation stage, a hyper-spectra sensor, and a stand for the non-planer object. The position of the sensor is fixed and the light is swept toward the sensor. For example, light moves from red position to green position, or from green position to blue position.

3.2 Shape Estimation

Appearance of thin film objects deeply depends on shapes. First, we estimate incident angles focusing on extremal intensity. Second, we estimate azimuth angles by the characteristics strip expansion method. Finally, we estimate a refractive index and film thickness.

In Section 3.2.1, we introduce a measurement setup for thin film objects in this chapter. In Section 3.2.2, we explain a method to estimate incident angles. In Section 3.2.3, we propose a method to estimate azimuth angles, and then estimate surface normals combining with the estimated incident angles. In Section 3.3, we introduce a method to estimate a refractive index and film thickness.

3.2.1 Measurement Setup

Fig. 3.1 shows a setup for measuring the thin film reflectance. The setup consists of a white light source, a rotation stage, a hyper-spectra sensor, and a stand for the non-planar object. The position of the sensor is fixed and the light is swept toward the sensor. For example, the light moves from red position to green position, or from green position to blue position.

The principal of measurement is as follows. Light advances to a non-planar object. One light is reflected off the thin film and the other light transmits through the thin film and reflects off the object. The angle between the light and the sensor changes as we measure the non-planar object. The viewing angle of the sensor is approximately 30 degrees along the Z-axis in Fig. 3.1. The band width in this experiment was 4 nm. When we measure the sample, a linear polarizer is placed in front of the light and sensor, as polarizer and analyzer.

3.2.2 Estimation of Incident Angle

We focus on the peak wavelengths as extreme values on spectra generated by interference, to estimate incident angles. At some peak wavelength, the phase difference Δ is $2\pi m$, $e^{i\Delta}$ becomes 1, and then m becomes a natural number. The peak wavelength is determined by the refractive index of the bottom layer and incident angle, in this

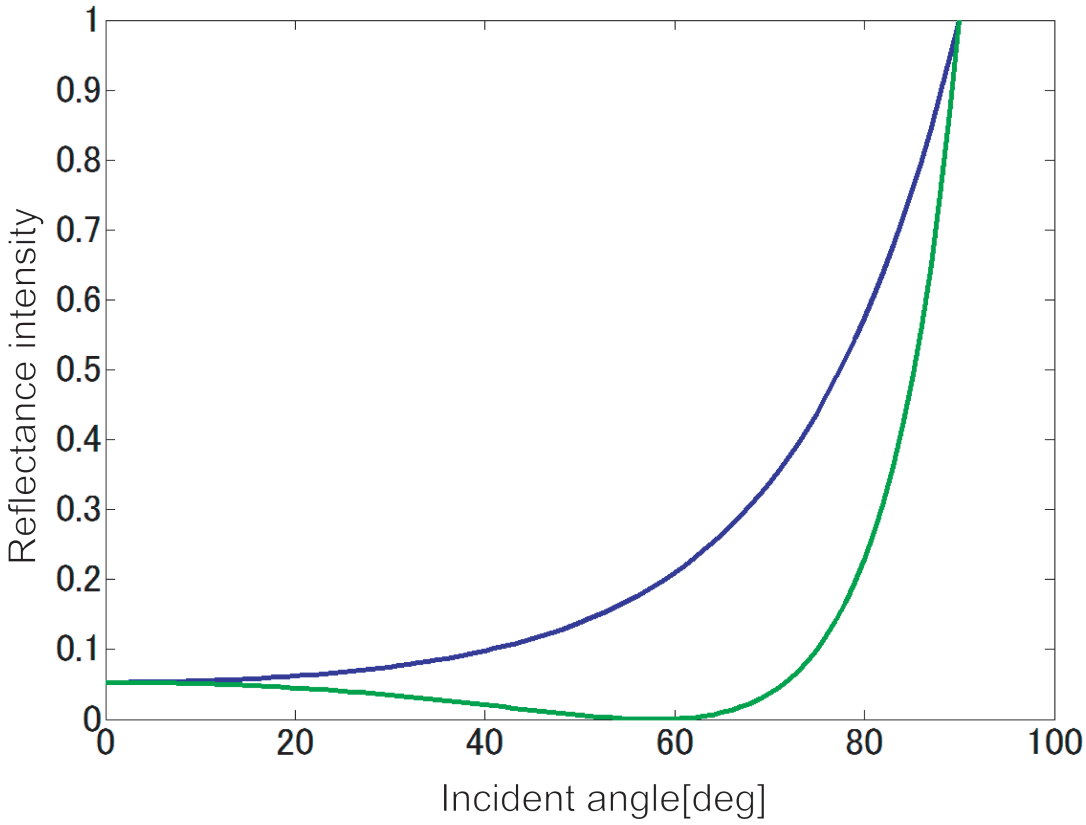

Figure 3.2: S- and P-polarization reflection intensity versus incident angle. Blue line is perpendicular polarization (S-polarization wave). Green line is parallel polarization (p-polarization wave).

phenomenon. We can estimate the incident angle by these peak wavelengths, if we know the refractive index of the bottom layer.

Fig. 2.2 shows reflection intensity for S-wave and P-wave versus wavelength. As shown in Fig. 2.2, we can observe several peak wavelengths as wavelengths of first peak values (extreme values) among the whole visual wavelengths. Here, we use local maximum or local minimum depending on the relation between the refractive index of thin film and that of the bottom layer. When the refractive index of the bottom layer is larger than that of the thin film, we can use the local maximum intensity. On the other hand, when the refractive index of the bottom layer is smaller than that of the thin film, we can use the local minimum intensity. In the case of the P-wave, the phase difference is reversed again at Brewster's angle. For this case we should use the local minimum intensity instead of the local maximum intensity, and local maximum intensity instead of the local minimum intensity.

The extremal intensity is defined by Eq. (3.1), substituting $\Delta = 2\pi m$ to Eq. (2.7).

$$R(\lambda_t) = \left| \frac{r_{12} + r_{23}}{1 + r_{12} r_{23}} \right|^2 \tag{3.1}$$

where λ_t is the first peak wavelength as shown with a circle in Fig. 2.2. Substituting these coefficients r_{12} and r_{23} to Eq. (3.1), the reflectance is as follows.

$$\begin{aligned} R_s(\lambda_t) &= \left| \frac{cos\theta_1 - n_3 cos\theta_3}{cos\theta_1 + n_3 cos\theta_3} \right|^2 \\ &= \left| \frac{cos_1 - n_3 \sqrt{1 - sin^2\theta_3}}{cos_1 + n_3 \sqrt{1 - sin^2\theta_3}} \right|^2 \end{aligned} \tag{3.2}$$

$$\begin{aligned} R_p(\lambda_t) &= \left| \frac{n_3 cos\theta_1 - cos\theta_3}{n_3 cos\theta_1 + cos\theta_3} \right|^2 \\ &= \left| \frac{n_3 cos\theta_1 - \sqrt{1 - sin^2\theta_3}}{n_3 cos\theta_1 + \sqrt{1 - sin^2\theta_3}} \right|^2 \end{aligned} \tag{3.3}$$

By Snell's law, $n_1 sin\theta_1 = n_2 sin\theta_2 = n_3 sin\theta_3$ and $n_1 = 1$, Eq. (3.2) and (3.3) becomes as

follows.

$$
\begin{aligned}
R_s(\lambda_t) &= \left| \frac{cos\theta_1 - n_3 \sqrt{1 - \frac{1}{n_3^2} sin^2\theta_1}}{cos\theta_1 + n_3 \sqrt{1 - \frac{1}{n_3^2} sin^2\theta_1}} \right|^2 \\
&= \left| \frac{\cos\theta_1 - \sqrt{n_3^2 - \sin^2\theta_1}}{\cos\theta_1 + \sqrt{n_3^2 - \sin^2\theta_1}} \right|^2
\end{aligned} \tag{3.4}
$$

$$
R_p(\lambda t) = \left| \frac{n^3 \cos\theta_1 - \sqrt{1 - \frac{1}{n_3^2} \sin^2\theta_1}}{\cos\theta_1 + \sqrt{1 - \frac{1}{n_3^2} \sin^2\theta_1}} \right|^2 \tag{3.5}
$$

Fig. 3.2 shows the reflection intensities for S-wave and P-wave versus the incident angle. We determine incident angles by least square between the observed and model intensity.

$$
\underset{\theta_1}{\text{Arg min}} \, |R_O(\lambda_t) - R_M(\lambda_t)|^2 \tag{3.6}
$$

where $R_O(\lambda_t)$ is the observed intensity, and $R_M(\lambda_t)$ is the model intensity. Depending on the polarization of reflectance, we determine whether $R_M(\lambda_t)$ is Eq. (3.4) $R_s(\lambda_t)$ or Eq. (3.5) R_p.

3.2.3 Surface Normal Estimation

We estimate the surface normal of the thin film by using the characteristic strip expansion method proposed by Horn[24]. This method uses the monotonically increasing intensity and steepest ascent in the gradient space. As mentioned in the previous section, the peak intensity monotonically increases. We find that the peak intensity corresponds to the gradient. We explain about the correspondence below.

In the image coordinate, an object point (x, y, z) is mapped to a pixel (u, v), for which $u = x$ and $v = y$ under the orthographic projection. If the object surface z is represented as follows,

$$
z = f(x, y) \tag{3.7}
$$

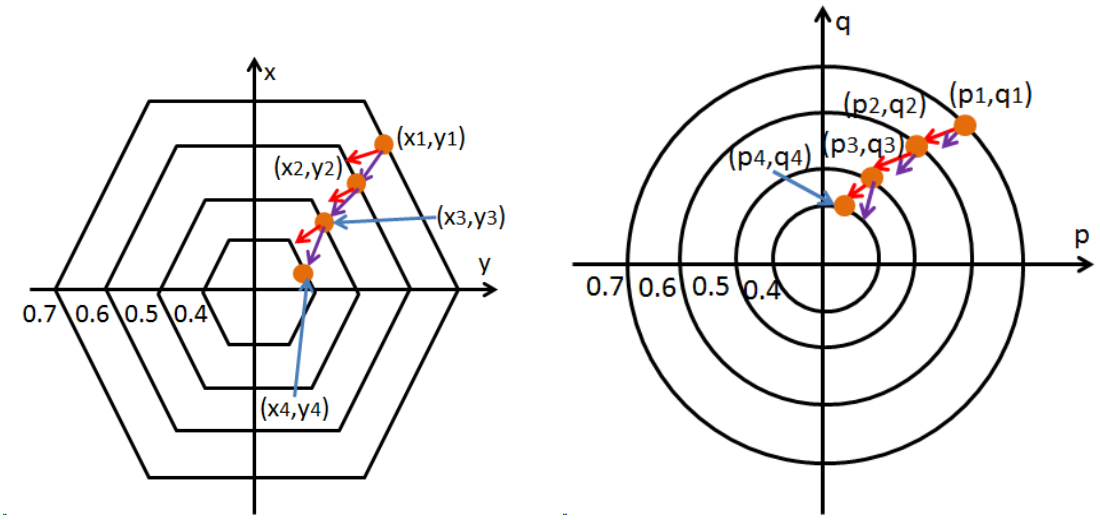

(a) Peak intensity map (b) Gradient space

Figure 3.3: Example of estimation using the characteristic expansion method. (a) the image which is mapped peak intensity to each pixel. (b) shows contour line in the gradient space.

, then the surface normal vector is defined by Eq. (3.8).

$$(p, q, -1) = \left[\frac{\delta f(x,y)}{\delta x}, \frac{\delta f(x,y)}{\delta y}, -1\right] \tag{3.8}$$

, where p and q are the parameters of the surface normal. The quantity (p, q) is the gradient of (x, y) and is called the "gradient space".

Normalizing Eq. (3.8) as 1, the z component of the surface normal becomes

$$z = \frac{1}{\sqrt{p^2 + q^2 + 1}} \tag{3.9}$$

This component is also equal to the cosine of the incident angle. Setting $x^2 + y^2 + z^2 = 1$, the existence domain of f (p, q) is on the circumference defined as Eq. (3.10).

$$p^2 + q^2 = \frac{1}{\cos^2 \theta_1} - 1 \tag{3.10}$$

By Eq. (3.10), the existence domain of gradients corresponds to the peak intensity. The peak intensity is determined uniquely by the incident angle. Also the existence domain is defined uniquely by the incident angle as shown in Eq. (3.10). This correspondence make it possible to apply the characteristics strip expansion method to the thin film objects.

We describe the estimation procedure with Fig. 3.3. Red arrows are steepest ascents in the peak intensity map. Purple arrows are steepest ascent in the gradient space.

1. Drawing contour lines by sampling the peak intensity per 0.1
2. Start from the pixel (x_1, y_1) in captured image which gradient $(p_1, q1)$ is known
3. Moving to the steepest ascent direction of (p_1, q_1) in captured image and determining (x_2, y_2) as the next pixel where intersect with contour line of the peak intensity
4. Moving to the steepest ascent direction of (x_1, y_1) in gradient space and determining (p_2, q_2) as the next gradient where intersect with contour line of the gradient
5. Repeating steps 3 and 4 until the whole surface normal is estimated

3.3 Optical Parameters Estimation

We focus on the peak wavelength as shown in Fig. 2.2 on spectrum generated by interference to estimate the refractive index and film thickness. The peak wavelength becomes an integral multiple of the optical path difference which includes refractive index and film thickness as parameters. Using this feature, we can narrow down combinations of parameters and reduce computational cost compared to a full search. The optical path difference Eq. (2.4) at the peak wavelength is as Eq. (3.11).

$$2n_2 d \cos\theta_2 = m\lambda_t \tag{3.11}$$

Using Eq. (3.11) and Snell's law, $n_1 sin\theta_1 = n_2 sin\theta_2 = n_3 sin\theta_3$,film thickness d is rewritten as Eq. (3.12).

$$d = \frac{m\lambda_t}{2\sqrt{n_2^2 - \sin\theta_1}} \tag{3.12}$$

In Eq. (3.12), a natural number m and a refractive index n_2 are unknown parameters. We determine these parameters by the least square between the observed reflectance and reflectance model.

$$Arg\min_{m,n_2} \left| \sum_{\lambda} (R_O(\lambda) - R_M(\lambda))^2 \right| \tag{3.13}$$

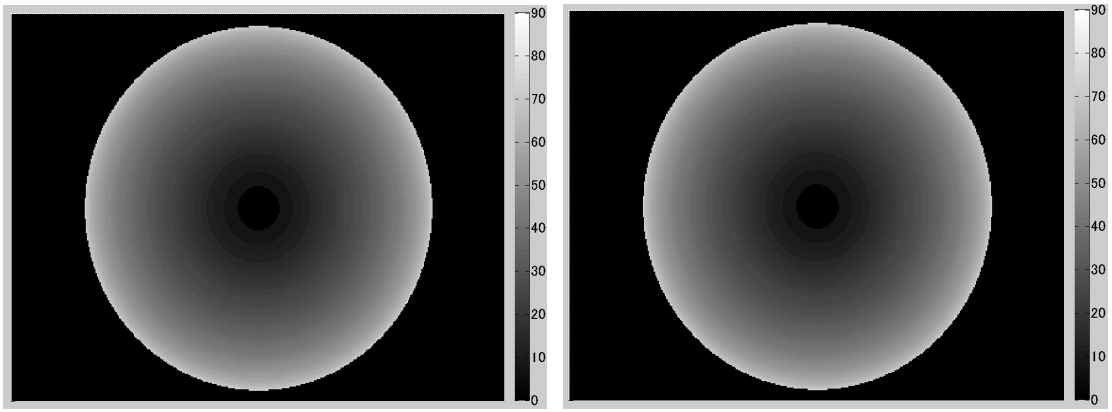

(a) The result of incident angle derived by using S-wave

(b) The result of incident angle derived by using P-wave

Figure 3.4: Estimated incident angle derived by using our method. (a) and (b) is the result of incident angle derived by using S-wave and P-wave, respectively. The right side bar indicates the relation between the color values and incident angle. The gray scale varies in increments of 10 degrees.

3.4 Experiment

In this section, we demonstrate the effectiveness of our method using simulation and real data. First, we confirm that our method can be applied to non-planar objects by simulation in Section 3.4.1. Second, we verify the estimation accuracy of the incident angle, the refractive index, and the film thickness by experimental data in Section 3.4.2. Next, we confirm the effect of measurement noise in Section 3.4.3. Finally, we use hyper-spectral images to estimate the incident angle and film thickness, and compare captured image with reconstructed image.

3.4.1 Simulation Results

We set the parameters as follows. The target object is a hemispherical object. Refractive index of the thin film is 1.36 for S- and P-wave, respectively, and the thickness is 630nm. Here, we determine $R_O(\lambda_t)$ by using real material data instead of observed data (spectrum).

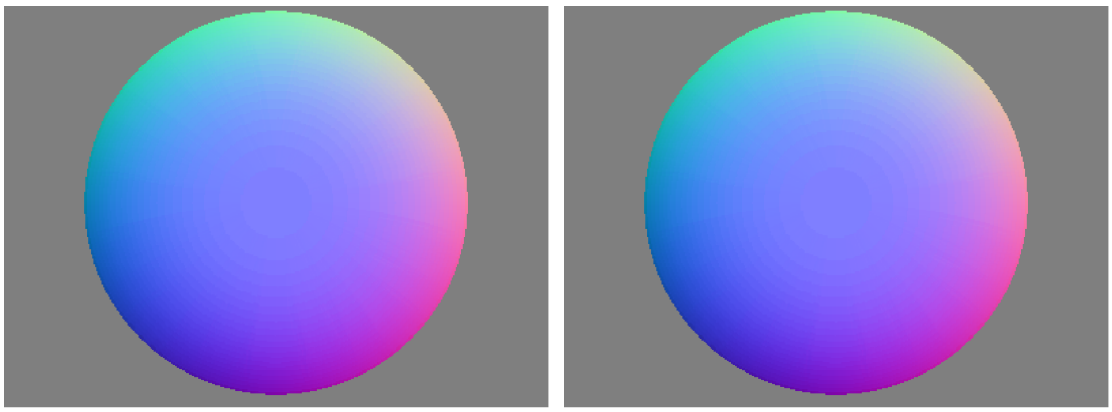

(a) The result of incident angle derived by using S-wave

(b) The result of incident angle derived by using P-wave

Figure 3.5: Estimated incident angle derived by using our method. (a) and (b) is the result of incident angle derived by using S-wave and P-wave, respectively. The right side bar indicates the relation between the color values and incident angle. The gray scale varies in increments of 10 degrees.

First, we determine $R_O(\lambda_t)$ by substituting the real material data described above, into Eq.(3.4) and eq.(3.5) for S- and P- waves, respectively. Next, $R_M(\lambda_t)$ is already given as real material data for both S- and P-waves. Finally, we can estimate the incident angle by using Eq.(3.6) for both S- and P-waves.

Fig. 3.5 shows the estimated incident angle derived by using our method, where (a) and (b) are those from S-wave and P-wave, respectively. The right side bar depicts the relation between the incident angles and gray values, which vary every 10 degrees. The incident angle was calculated by using set parameter data for S and P-waves; we assume the object's shape is a hemisphere. Fig. 3.5 shows the estimated surface normals derived by the characteristic strip expansion method, where (a) and (b) are those from S-wave and P-wave, respectively. The surface normals are calculated from estimated incident angle. The contour of estimated surface normals is caused by setting interval of the characteristic strip expansion method.

Fig. 3.6 shows the estimated film thickness on the hemisphere from the incident angles obtained from S and P waves. Here, the right side bar shows a rainbow color scale indicating thickness. The color changes according to every 10 nm. In Fig. 3.6, the

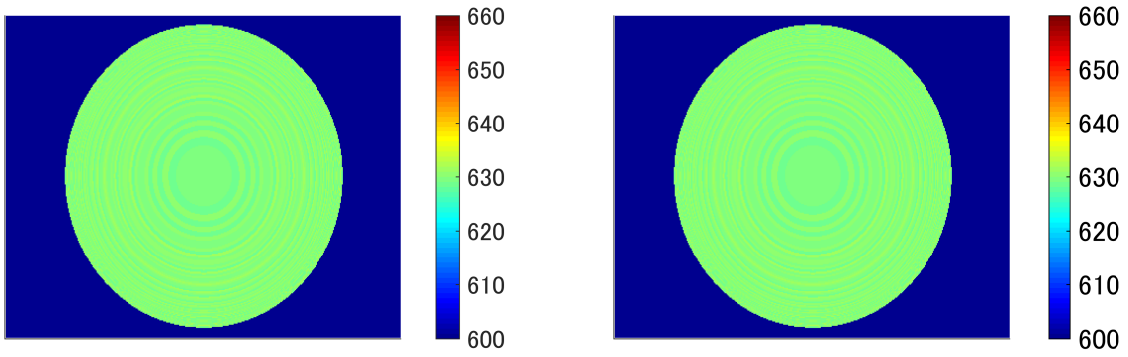

(a) The film thickness derived by using S-wave

(b) The film thickness derived by using P-wave

Figure 3.6: Film thickness on hemisphere estimated from calculated incident angle. (a) and (b) are the result of film thickness derived by using S-wave and P-wave. The right side bar indicates the relation between the color values and film thickness. The color scale varies in increments of 10 nm.

error for both (a) and (b) was within 5nm.

3.4.2 Real Data by Spectrometer

The thin film on non-planar objects, such as status or architecture, is approximated by a thin film plate microscopically. This is possible because the film thickness, in the order of 0.4-1 μm, is much smaller than the size of the object. Therefore, we evaluated the effectiveness of the estimated optical parameters by using the thin film plate.

Fig. 3.7 shows the schematic diagram of our experimental setup. In our experiment using real data, we selected PET film as the transparency object, which is difficult for us to measure. Because PET film is flexible, it was set on a rigid black plate. The black backside also provided the strong reflection for the normally transparent film. A diffuser was placed in the position of the hyper-spectral sensor in Fig. 3.1 to avoid detecting strong reflections directly. The refractive index of MgF_2 is 1.36. The film thickness was 630 nm as measured by IfS. The substrate of the thin film is a PET film whose refractive index is 1.6. To avoid the interference between the light source and hyper-spectral sensor (we use diffuser in this case.), we set the incident angle from 10 to

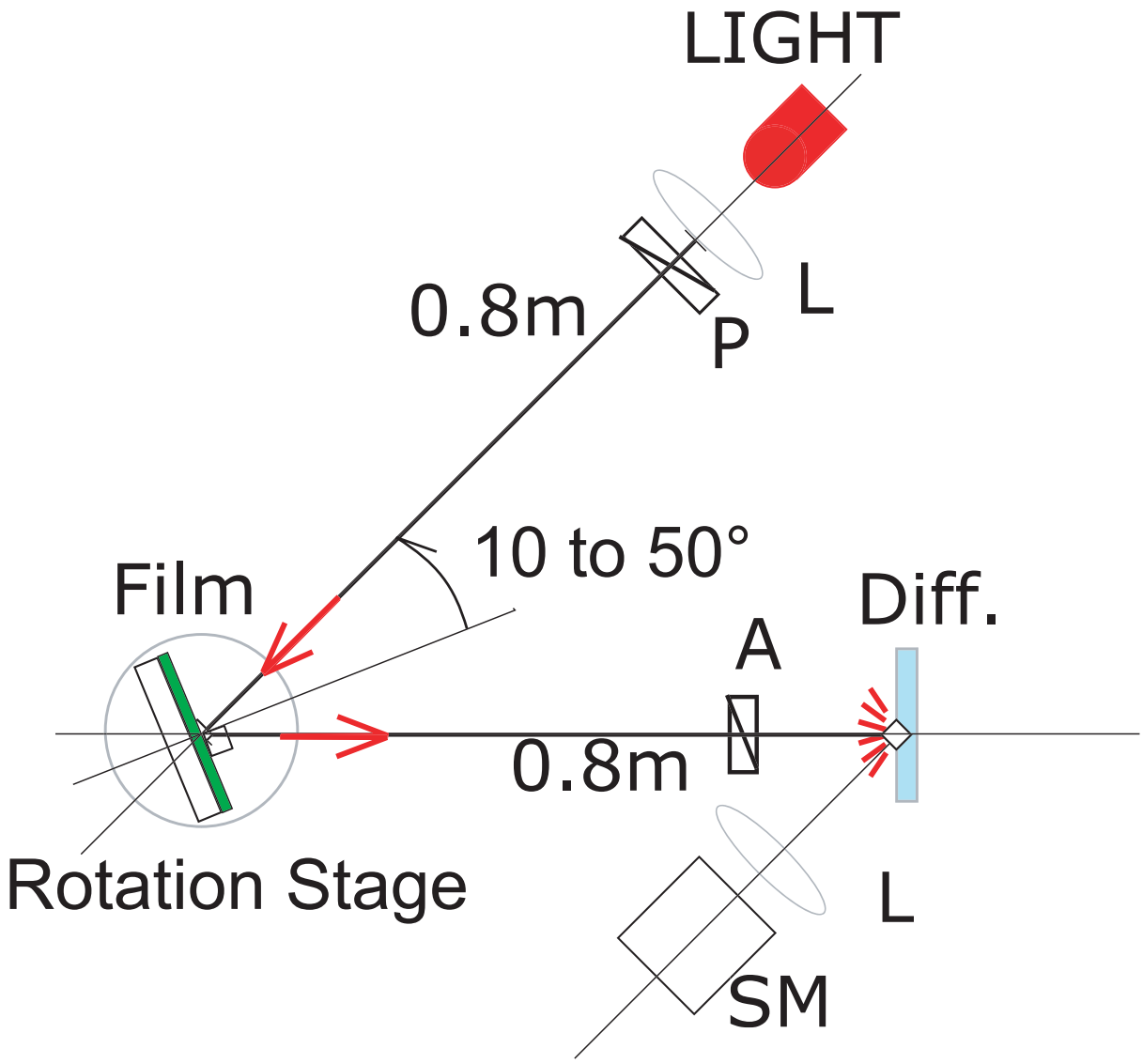

Figure 3.7: Schematic diagram of experimental setup. Here, Film is a target thin lm of object. L means a lens. P is a polarizer. A is an analyzer. SM is a spectrometer. Di is a diuser.

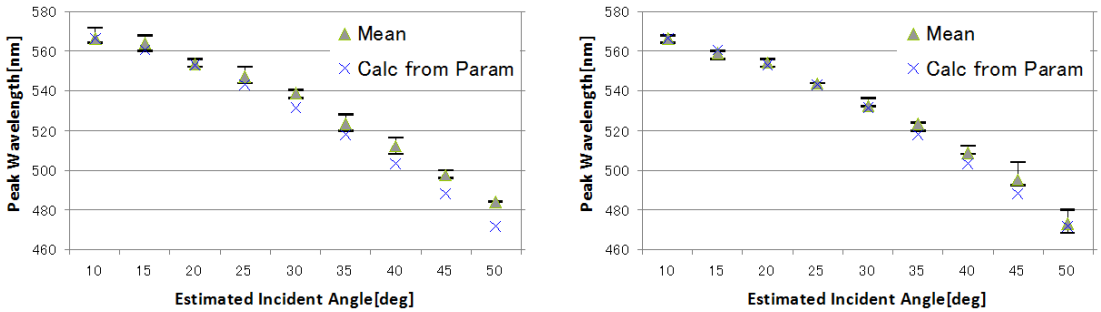

(a) S-wave (b) P-wave

Figure 3.8: Peak wavelengths in the visual region along estimated incident angle. Triangle point (Mean) is the average wavelength from measured reflectance. X-mark is the calculated incident angle from peak wavelength measured by interference spectroscopy. (a) shows S-wave peak wavelength. (b) shows P-wave peak wavelength.

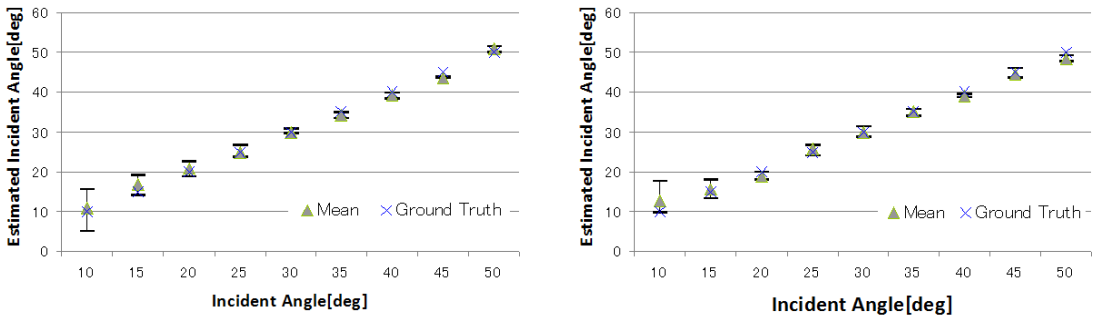

(a) Measurement results for S-wave (b) Measurement results for P-wave

Figure 3.9: Estimated incident angles versus ground truth. Fig. (a) and (b) are results for S-wave and P-wave, respectively. The ground truth is the preset angle of our experimental setup. Mean is the average of estimated incident angles.

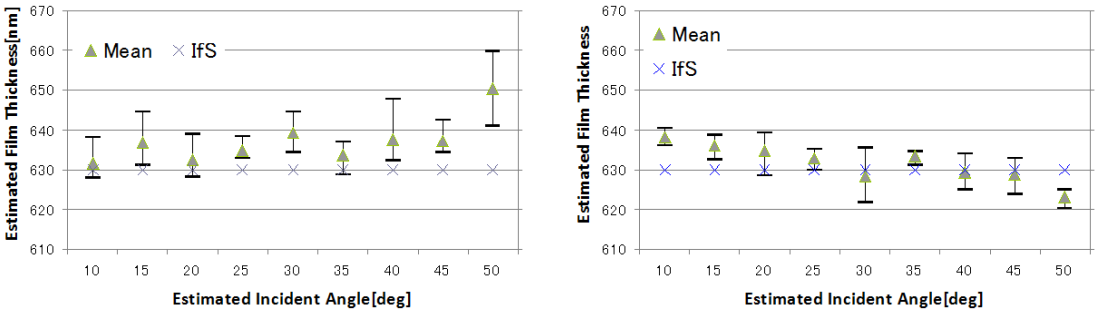

(a) S-wave (b) P-wave

Figure 3.10: Estimated film thickness versus estimated incident angle. Fig (a) and (b) are estimated film thickness derived by measurement for S-wave and P-wave, respectively. Regulated setting Angle is rotation angle of light source when rotation axis is Y-axis. Mean is average of estimated film thicknesses. IfS is film thickness measured by interference spectroscopy on 0 degree.

50 degrees, by each 5 degree steps. We measured these samples 5 times at each angle. We estimated the incident angle and optical parameters for each measurement.

First, the incident angle θ_1 was estimated from the observed intensity $R_O(\lambda_t)$ and model intensity $R_M(\lambda_t)$ using Eq. (3.6). Next, the reflective index n_2 and film thickness d were estimated using Eq. (3.13). Therefore, we confirmed the observed spectrum data in order to determine the accuracy of the measurement.

Fig. 3.8 shows peak wavelengths in the visual region along the estimated incident angle, where values marked X indicate those theoretical values given by the model.

Considering Eq. (3.12), m must be a natural number larger than 1. When θ is 0, the denominator of Eq. (3.12) is maximum.

$$d_{min} > \frac{\lambda_t}{2\sqrt{n_2^2 - 1}} \tag{3.14}$$

In our experiment, the natural number m is equal to 1 since we could find two peak wavelengths from 380 nm to 780 nm. If the target material is MgF_2, the possible value of estimated minimum thickness $d_p = 213$ nm, since $n_2 = 1.36$ and $\lambda_t = 580$. Therefore, we can estimate the thickness larger than 213 nm. On the other hand, when the thickness is $d = 630nm$, the estimated peak wavelength must be less than 1713 nm. The measured

peak wavelengths have been satisfied with the condition. Moreover, the average error of the peak wavelength was less than 6nm. The result shows the error is sufficiently close to the band width (4 nm) of the spectrometer.

Fig. 3.9 shows the estimated incident angles versus the ground truth. The ground truth is the preset angle of our experimental setup. Fig. 3.9 (a) and (b) are the estimated incident angles derived by the measurement for S-wave and P-wave, respectively. The mean is the average of the estimated incident angles. The incident angle change is from 10 degrees to 50 degrees as shown in Fig. 3.7. The angle between the light source and diffuser varies from 20 degrees to 100 degrees. The average errors of S- and P-waves are 0.84 and 0.92 degrees, respectively. The results showed that the estimated incident angle coincided with the ground truth.

Fig. 3.10 shows the estimated film thickness versus the estimated incident angle. Fig. 3.10 (a) and (b) are the estimated film thickness derived by measurement for S-wave and P-wave, respectively. The mean is the average of the estimated film thicknesses. IfS is the film thickness measured by the interference spectroscopy on 10 degrees. Here, we assume the film thicknesses are the same values even if the incident angle increases. First of all, the average errors of S- and P-waves were 7 nm and 4 nm, respectively. These errors are close to the band width of the spectrometer (4 nm). Futhermore, the errors of P-wave are stable in all estimated incident angles. However, the errors of S-wave gradually increase depending on increasing incident angles.

The refractive index was estimated together with thin film thickness. The range of the refractive index was from 1.34 to 1.37 and the average refractive index was 1.36 for S-wave. On the other hand, the range of the refractive index was from 1.34 to 1.36 and the average refractive index was 1.35 for P-wave. We believe the anisotropy of the estimated refractive index is within the range of the error.

3.4.3 Measurement Error of Spectrometer

It is thought that the factor of the estimation error is caused by the setup error of the optical system, the noise of light power, and error of the measurement. We evaluated the measurement noise of spectrometer.

Fig. 3.11 shows the experimental setup for verifying variance of the spectrometer. MC, L, SM, and Light indicate a Macbeth Color chart, a lens, a spectrometer, and a

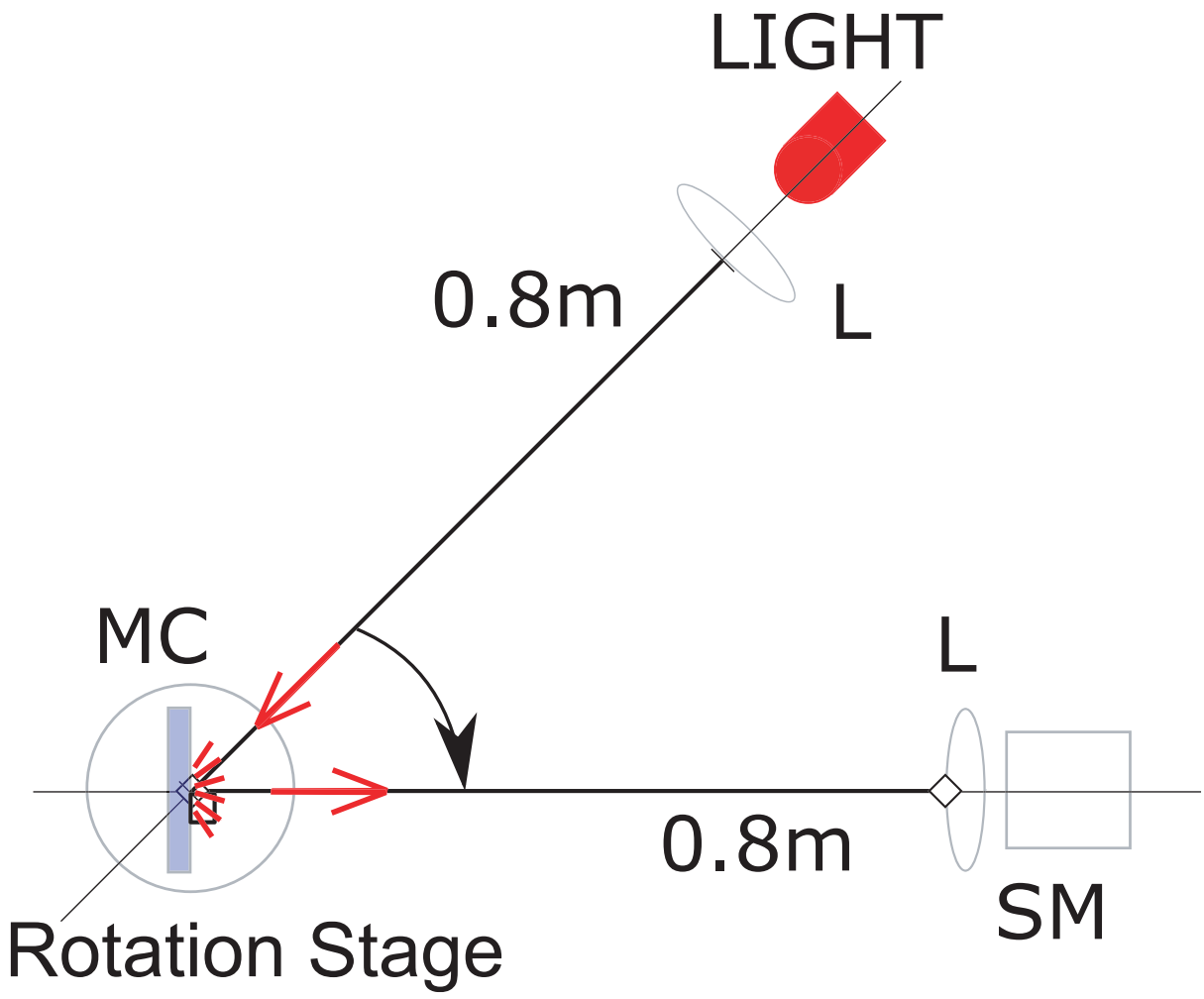

Figure 3.11: Experimental setup for verifying variance of the spectrometer. MC is Macbeth Color Chart. L is a lens. SM is a spectrometer. LIGHT is an LED light source. To detect diuser light on MC, the SM is placed in a vertical position.

Figure 3.12: Macbeth Color Chart used for measuring the variance of a spectrometer. White and gray patches enclosed in the Red rectangle are measured. W, G1, G2, G3 and G4 are standard for the chart. They represent reflection intensities of 100 %, 80 %, 60 %, 40 % and 20 %,respectively.

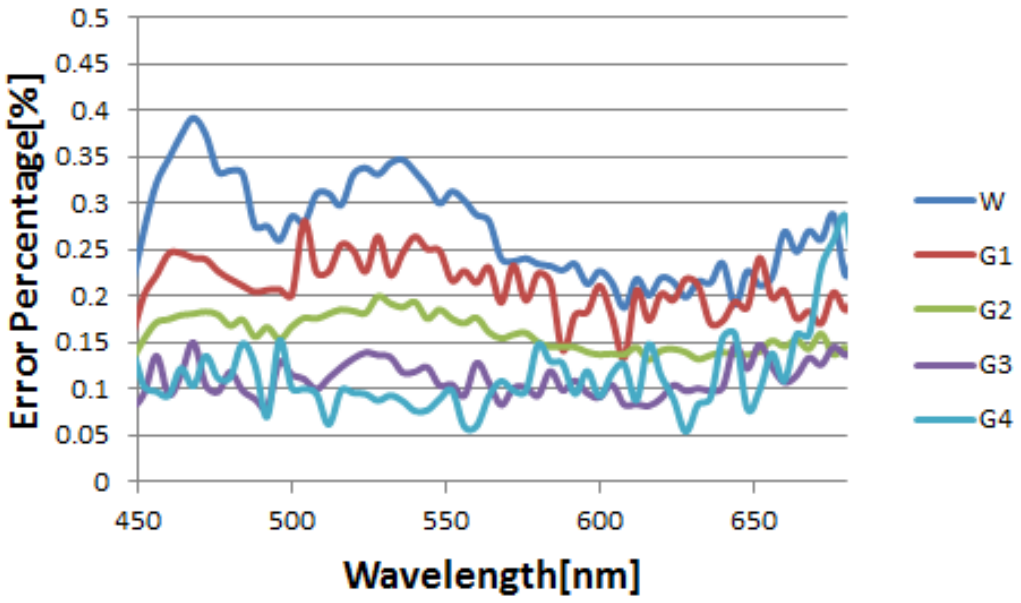

Figure 3.13: Noise of reflection intensity (%) on Macbeth Color versus each wavelength. W, G1, G2, G3 and G4 are standard for the chart and represent reflection intensities of 100 %, 80 %, 60 %, 40 % and 20 %,respectively. Noise of reflection intensity (%) is the deviation from average spectrum.

LED light source, respectively. The Macbeth Color Chart (MC) was illuminated from an oblique direction as shown in Fig. 3.11 and diffused light on the chart advance to spectrometer. Reflectance of ”W” is 100 %. Reflectance of ”G1”, ”G2”, ”G3” and ”G4” is 80 %, 60 %, 40 % and 20 %, respectively. We used a white LED as the light source.

Fig. 3.13 shows the variance of reflection intensity (%) on Macbeth Color versus each wavelength. Noise of reflection intensity (%) is the deviation from the average spectrum. Here, we measured the spectrum of MC 10 times and the value of noise shows the variation from the average spectrum. Under the range of wavelength from 450 to 670 nm, the noise (%) was within 0.4 %. This means that the measurement noise was within 0.4 %. As the reflectance increased, the noise became smaller; this is thought to be a result of the S/N ratio increasing as reflectance decreased. The average noise (%) on each reflectance was 0.168 %.

3.4.4 Real Data by LCTF

In this section, we conducted an experiment of real data by hyper-spectral images. Fig. 3.14 shows the setup for the thin film reflectance measurement to acquire the real data. A light source was attached to the rotation table to adjust the incident angle. The target thin film was MgF_2 whose refractive index is 1.37. The film thickness was 400 nm. The refractive index of the bottom layer was 1.6, made of polyethylene terephthalate. We varied the incident angle from 10 to 42.5 degrees by 2.5 degrees.

The measurement device was a hyper-spectral camera, which consists of a liquid crystal tunable filter (Vari Spec CRI) and a monochrome camera. The liquid crystal tunable filter (LCTF) can change its transmitted wavelengths electrically. The viewing angle of the camera is approximately 30 degrees. The band width in this experiment was 4 nm. We putted a linear polarizer, which transmits S-wave. LCTF also transmits linearly polarized light, so we can capture S-wave reflectance. The transmittance of LCTF is only 4 % around 400 nm. The brightness of S-wave is stronger than that of P-wave, therefore we measure S-wave.

Fig. 3.15 shows the captured reflectance and the estimated result of the real data. The error increased around 0 to 20 degrees. The error was approximately 9 degrees in this area. At other incident angles, the error was less than 5 degrees.

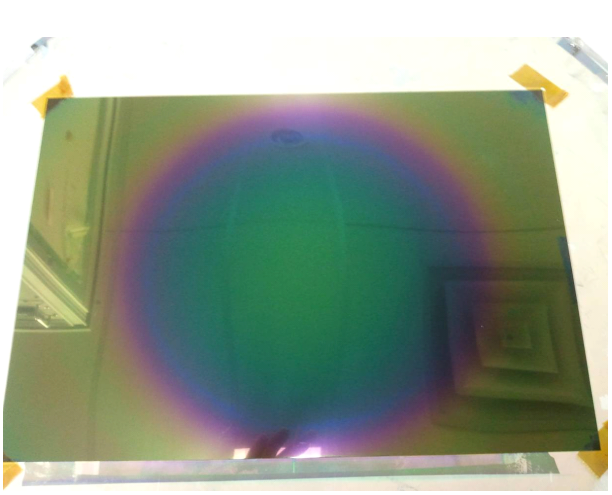

(a) Target thin film

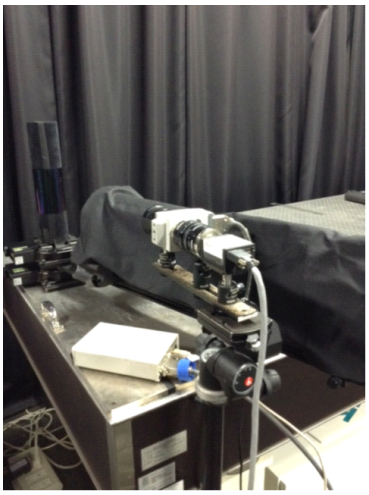

(b) Actual setup

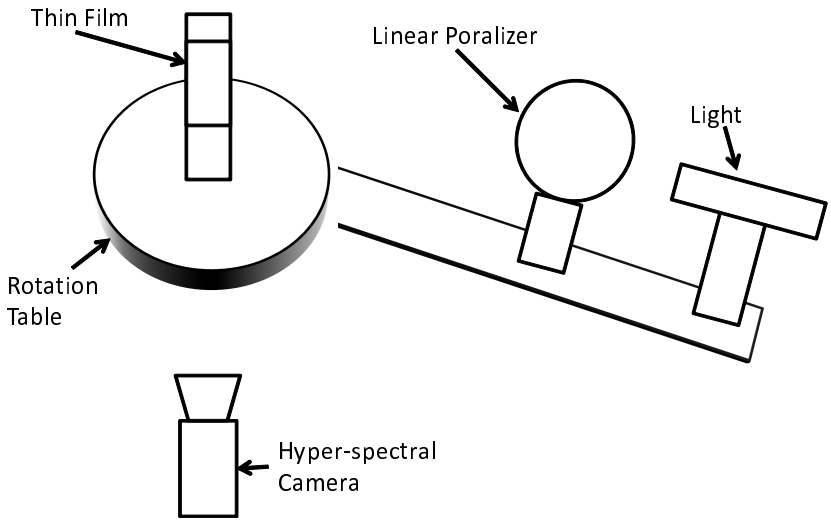

(c) Schematic diagram of setup

Figure 3.14: Experimental setup for measuring thin film reflectance. (a) shows target thin film. (b) shows schematic diagram of setup. (c) shows actual setup. Distance between light source and the thin film was 0.8 m. Distance between the camera and the thin film was 0.6 m.

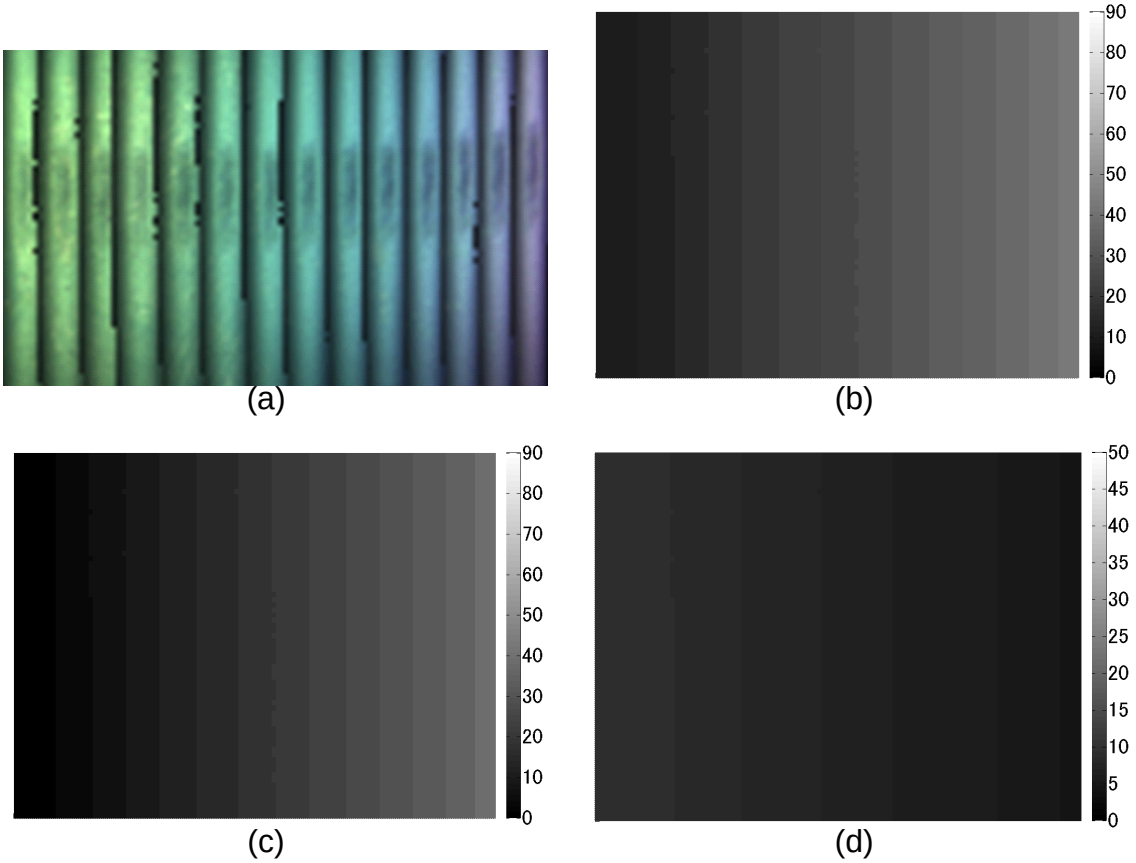

Figure 3.15: Incident angle estimation results of real data. (a) shows input reflectance image. (b) shows ground truth incident angle. (c) shows estimated incident angle. (d) shows estimation error.

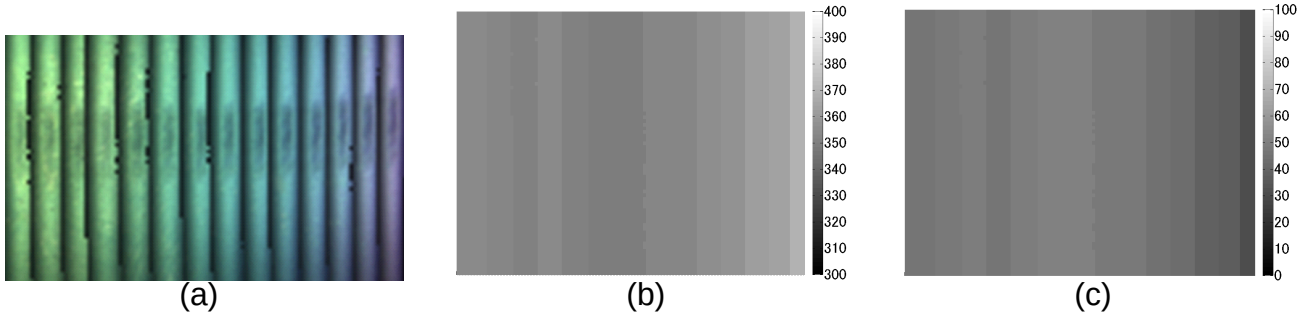

Figure 3.16: Film thickness estimation result of real data. (a) shows input reflectance image. (b) shows estimated film thickness. (c) shows estimation error.

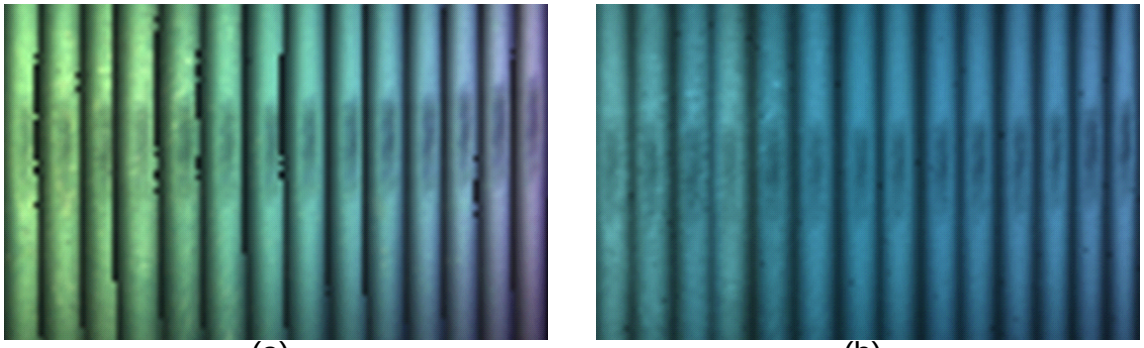

Figure 3.17: Image synthesized with estimated surface normal, refractive index, and lm thickness. (a) and (b) are results for simulation data. (c) is reectance image captured by the hyper-spectral camera. (d) is synthesized reectance image for real data.

We estimated the refractive index and film thickness, by using the estimated incident angle. The estimated refractive index was 1.41. Fig. 3.16 (b) shows the estimated thickness. Fig. 3.16 (c) shows the estimation error. The average error was 45 nm.

We calculated the average color difference and root mean square error (RMSE) between the measured reflectance and the reflectance with estimated parameters. The color difference was calculated using Eq. (3.15).

$$\Delta E^*ab = \sqrt{(\Delta L^*)^2 + (\Delta a^*)^2 + (\Delta b^*)^2} \tag{3.15}$$

The RMSE is defined as Eq. (3.16).

$$RMSE = \sqrt{\sum_{\lambda} (R_o(\lambda) - R_e(\lambda))^2 / N} \tag{3.16}$$

$R_o(\lambda)$ is the measured reflectance. $R_e(\lambda)$ is the reflectance calculated by using the estimated parameters. The color difference was approximately 3.33, which can be perceived as a slight difference from the levels given in Table 2.2. The RMSE was about 2 % for each wavelength intensity. Fig. 3.17 shows the rendering results with the estimated surface normal, refractive index and film thickness.

3.5 Discussion

In the experiment, we show how accurate our method is in simulation and real data. The simulation results has almost no error, and then it shows that our method theoritically work well. However we have some errors in real data. Therefore, we discuss what causes experimental errors of the incident angle and film thickness in this section.

3.5.1 Experiment with Spectrometer

First of all, we discuss the error of the incident angle. The error of the incident angle is affected by the error of peak intensity since we estimate directly from the peak intensity curve as shown in Fig.3.2. When we have some errors of peak intensity α, the estimation error changes as β in Fig.3.18. Verifying in the previous section, the measurement noise of the real data experiment is 0.168 % which is caused by light noise, sensor noise of the spectrometer. Therefore, we have ± 0.168 % as average measurement noise in real data experiment.

We calculate the error of an incident angle when we add ± 0.168 % to S/P peak intensity in Fig.**??**. The average error of the incident angle becomes 1 degree for S/P polarization respectively. This error is almost as same as the real data experiment. Therefore, the error in real data experiment is due to the measurement noise, and then our method does work well on the incident angle estimation.

Finally, we discuss the error of the film thickness. In our method, we squeeze candidates of the film thickness from the optical path difference since it becomes an integral multiple of peak wavelength. Fig. 3.8 shows detected the peak wavelength and ground truth peak wavelength. The average error of peak wavelength becomes 3 nm for S-wave, and 6 nm for P-wave. These results are closer to film thickness error, then the detection error causes the thickness error. Therefore, it also indicates that the film thickness estimation does work well.

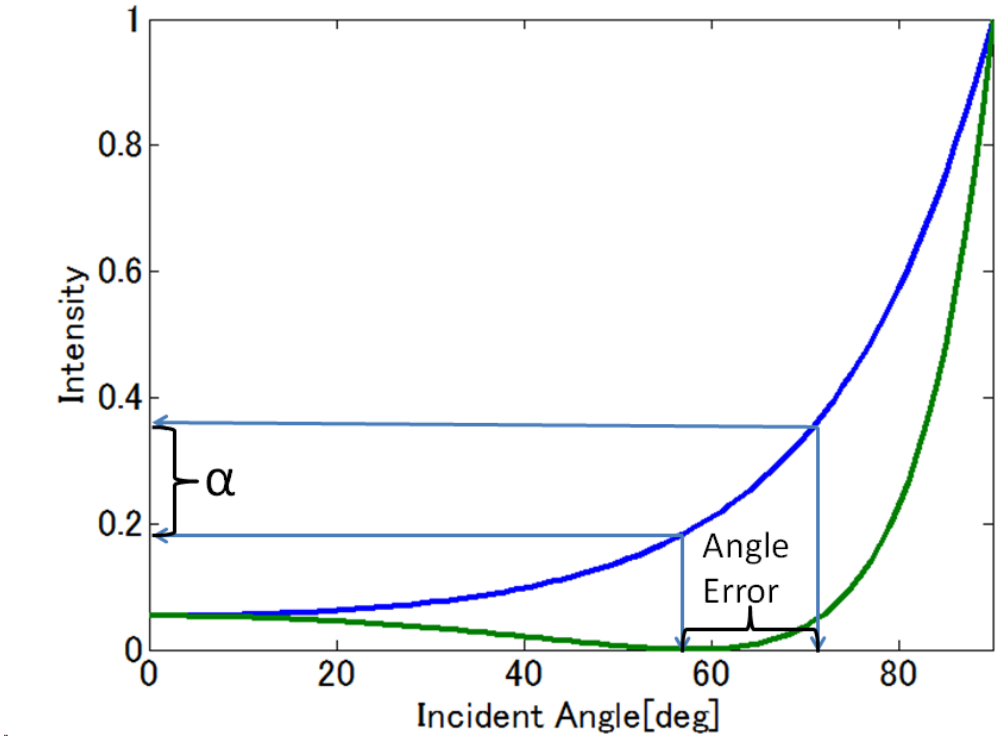

Figure 3.18: Relation between input noise α of reflectance and incident angle error. The extremal value is S-wave reflectance. The refractive index of the bottom layer is 1.6.

3.5.2 Experiment with LCTF

In this section, we discuss estimation results with LCTF. The error of the incident angle became larger around 0 to 20 degrees. In these areas, the peak wavelengths were close to each other. This is very close to the sampling interval of the simulation data and the band width of the hyper-spectral camera, so intensity detection became difficult. The error of the surface normal and optical parameters became large in the same area where the error of the incident angle became large. This error occurred because of the incident angle estimation error. The error of the optical parameters error of the real data becomes large outside these areas. The measured reflectance included noise which make the detection accuracy of the peak wavelength lower. Therefore, we can avoid these errors by using a high wavelength resolution and hyper-spectral camera with less noise.

Comparing the synthesized image Fig. 3.17 (d) and real image Fig, 3.17 (c), we can perceive the difference. The color difference occurs by the error of the incident angle and rounding error of captured reflectance spectra around 430 nm. Over 40 degree, the sample MgF_2 has the peak intensity around 430 nm, but hyper-spectral camera could not capture it with enough brightness because of its low transmittance. The low transmittance cause the rounding error which effects as noise, so we have the difference. The wavelength dependency of the refractive index is also considerable. However, we experimentally verified it does not effect to the estimated appearance for this sample.

We could estimate the incident angle and optical parameters even in darker areas in Fig. 3.17 (c). In darker areas, just the intensity of the measured reflectance is small, and we could measure reflectance spectra correctly. Therefore, estimated results of Fig. 3.15 (c) and 3.16 (b) had parameters in darker areas in Fig. 3.17 (c).

3.6 Summary

We proposed a method to estimate incident angle and optical parameters of non-planar objects with thin film. We focus on the peak intensity to estimate incident angle since the peak intensity only depends on the refractive index of bottom layer and incident anlge. To estimate optical parameters, we squeeze candidates of film thickness focusing on the peak wavelength and minimize the least square error between mea-

sured and model reflectance. In the experiment, we showed an accuracy of estimated incident angles and optical parameters. We also showed that estimation errors was caused by measurement noise of spectrometer and detection error of peak wavelength. This result showed that our method theoritically work well for real data objects.

Chapter 4

Measurement Equipment for Thin Film Objects with Non-Planar Surfaces

4.1 Overview

In Chapter 3, we introduced a method to estimate the incident angle and optical parameters. We also showed that our method works well in the real data experiment. However, we apply our method to planar objects because of the limitation of the measurement equipment. To solve this problems, first of all, we develop novel equipment to measure the reflectance of non-planar objects. Finally, we propose a method to estimate azimuth angles to reconstruct shapes: zenith and azimuth angles are parameters of surface normals.

The rest of this chapter is as follows. In Section 4.2, we explain novel equipment to measure the reflectance of non-planar objects at once. We also propose a method to estimate azimuth angles and estimate shapes of thin film objects. In Section 4.3, we conduct experiments by the real data to show the effectiveness of our methos. In Section 4.4, we discuss experimental errors. In Section 4.5, we summarize this chapter.

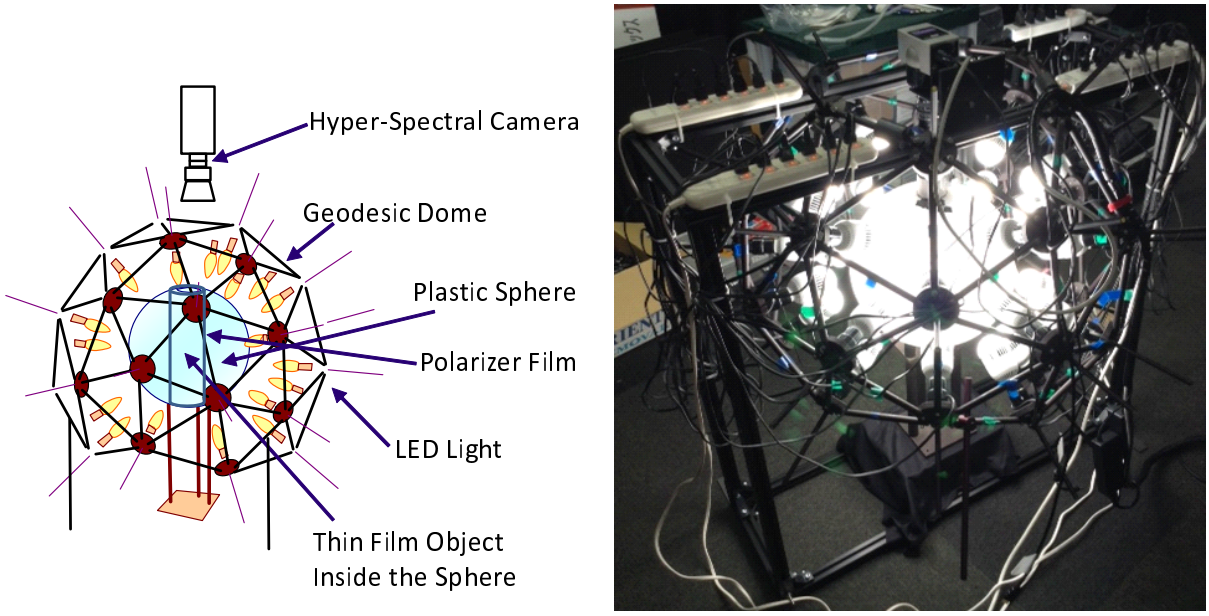

(a) Device diagram (b) Actual setup

Figure 4.1: Measurement equipment illuminating target objects omni-directionally. (a) shows diagram of equipment. (b) shows actual setup.

4.2 Measurement Equipment and Shape Estimation

In this section, we introduce equipment to measure the reflectance of thin film objects, and a method to reconstruct shapes. For reconstruction of shapes, we estimate zenith and azimuth angles. The incident angle estimation is the same as Chapter 3. Therefore, we introduce a method to estimate azimuth angles.

4.2.1 Measurement Equipment

The reflectance of thin film objects can be observed when incident and reflection angles become equal. Therefore, we acquire the reflectance of a non-planar objects with a thin film by illuminating from various directions. However, it is time consuming to measure the reflectance moving sequentially around objects. To reduce measurement time, we develop a device which have omnidirectional illumination environment.

Fig. 4.1 shows our measurement equipment. We use a geodesic dome which has an icosahedron. We put a LED light at the vertex of the dome, and illuminate the white

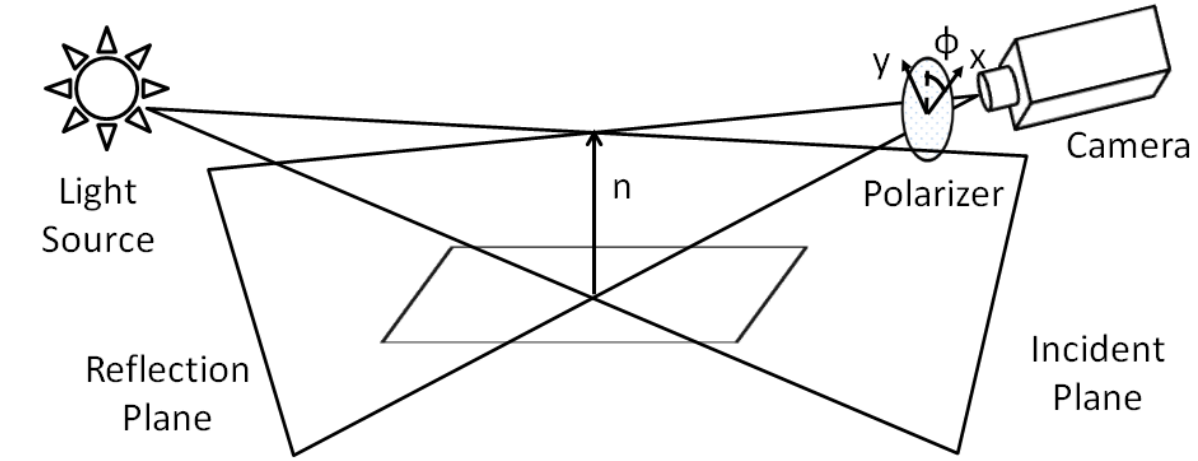

Figure 4.2: Relation between incident plane and azimuth angle.

plastic sphere in the geodesic dome omini-directionally. We put a target object in the white plastic sphere. Therefore, the target object is illuminated omni-directionally, and then we can acquire the reectance at once. We also set a polarizer lm in the white plastic sphere, then we acquire the reectance of perpendicular polarization.

4.2.2 Azimuth Angle Estimation

In this section, we introduce a method to estimate azimuth angles of a thin film object. Generally, light has characteristics of electromagnetic wave which is called polarization in physics. When the light reflects on object's surface, reflected light is divided into parallel and perpendicular polarization. The parallel polarization is parallel light to the incident plane. The perpendicular polarization is vertical light to the incident plane. As shown in Fig. 4.2, the azimuth angle is vertical to the incident plane, and then the perpendicular polarization is parallel to the azimuth angle. Therefore, we can estimate the azimuth angle by detecting perpendicular polarization.

We detect perpendicular polarization by a rotating polarizer in front of a camera. When the polarizer is rotated, the intensity of captured images is changed from bright to dark among 180° rotation of the polarizer. The azimuth angle is parallel to perpendicular polarization, then, the rotation angle is equal to azimuth angle when we observe maximum the intensity. However, there are two maximum intensities. If we

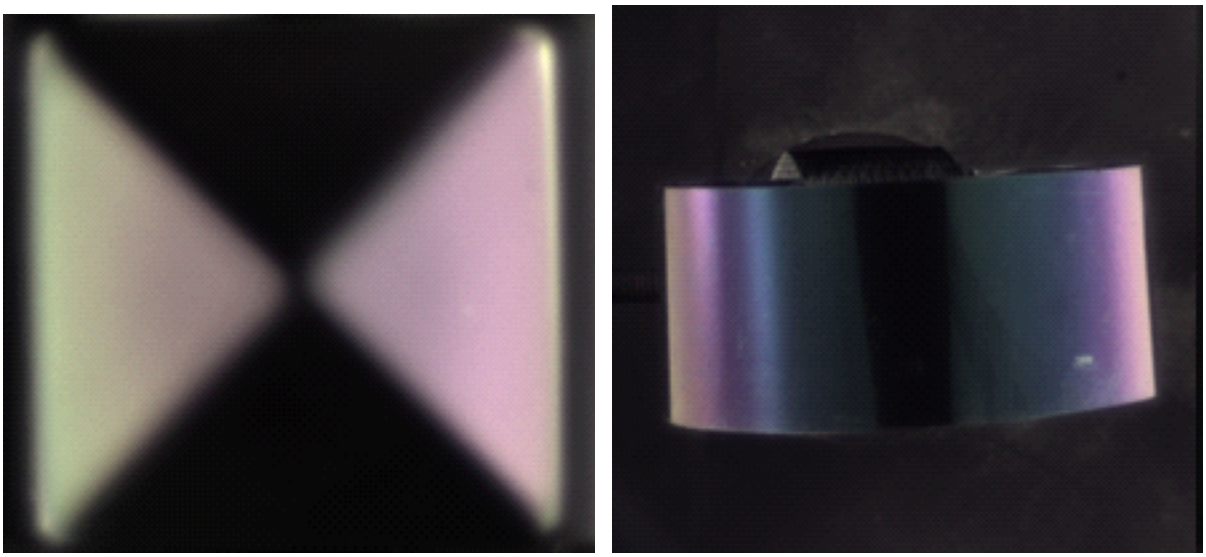

(a) Reflectance image of cylindrical object (b) Reflectance image of quadrangular pyramid object

Figure 4.3: One of reflectance images captured by our measurement equipment.

define one angle as ϕ, the other one becomes $\phi + 180°$. We solve this ambiguity using occluding boundaries of the target object as follows.

We assume that the surface normal directs outwards. When the boundary is closed, the integrated value of the surface normal in a small region becomes 0[25].

$$\iiint_C f(x, y, z)dxdydz = 0 \tag{4.1}$$

where C is the area of the small region in tje target objects. We estimate azimuth angles of the whole objects by following steps.

1. Estimate azimuth angles having ambiguities around occluding boundaries satisfying Eq. (4.1).
2. Estimate azimuth angles in near regions of 1 in the same way iteratively.
3. Estimate azimuth angles in the whole region of target objects.

4.3 Experiment

In this section, we conduct experiments only with real data because we already evaluated the simulation in Chapter 3. The target objects are cylindrical object and quadrangular pyramid object. For the cylindrical object, MgF_2 is evaporated on a PET film. We set the thickness as 400 nm on physical vapor deposition. We roll up this film and make a cylindrical object. For a quadrangular pyramid object, MgO is evaporated on quadrangular pyramid button which is consisted of ABS resin. We set the thickness as 560 nm on physical vapor deposition. Fig. 4.3 shows one of reflectance images of cylindrical object and quadrangular pyramid.

Fig. 4.4 shows the estimated incident angle and its errors. The average error of the incident angle is 8.62 degree for the quadrangular pyramid object and 1.10 for the cylindrical object. Fig. 4.5 shows estimated surface normals. The average error of surface normals is same as incident angle. Fig. 4.6 shows the spatially varying film thickness. Estimated refractive index becomes 1.39 for the cylindrical object and 1.76 for the quadrangular pyramid object. Fig. 4.7 shows synthesized images by the estimated parameters which are the incident angle, refractive index, and film thickness. The average color difference in ab space is 8.15 for the cylindrical object, and 4.34 for the quadrangular pyramid object. The difference is calculated between the captured reflectance and reflectance by the estimated parameters. The level of color difference is ”much” for the cylindrical object, and ”appreciable” for the quadrangular pyramid object.

4.4 Discussion

In this section, we discuss the estimation results of the incident angle, surface normal, and optical parameters. The average error of the incident angle becomes about 8 degrees for the quadrangular pyramid object. The error becomes about 30 degrees around the corner because the acquired reflectance around the corner includes much noise to estimate stably. Outside the corner, the error is close to the simulation result in the previous section. The average error of cylindrical object is also the same as the simulation result.

The estimated thickness becomes smaller than setting the thickness on physical vapor deposition. The estimated thickness also distributed from 400 nm to 480 nm for the quadrangular pyramid object. The thickness becomes thinner concentrically away from the center of the physical vapor deposition. We do not measure accurate distance between the objects in this experiment and the center of the equipment. Therefore, we could not determine the distribution of the estimated thickness is caused by this phenomena, but it has high probability to cause the distribution of the estimated thickness.

4.5 Summary

We developed an equipment to measure the reflectance of thin film interference. The reflectance of thin film can be observed only when incoming and reflection angle become equal. Using this feature, we can acquire the reflectance of non-planar objects at once by omni-directional illumination environment. Therefore, we put light sources around white plastic sphere, and set the target thin film object in the sphere, then we acquired reflectance at once. In the experiment, we measured the reflectance and estimated shapes and optical parameters. We also reconstructed the images and showed that our method works well.

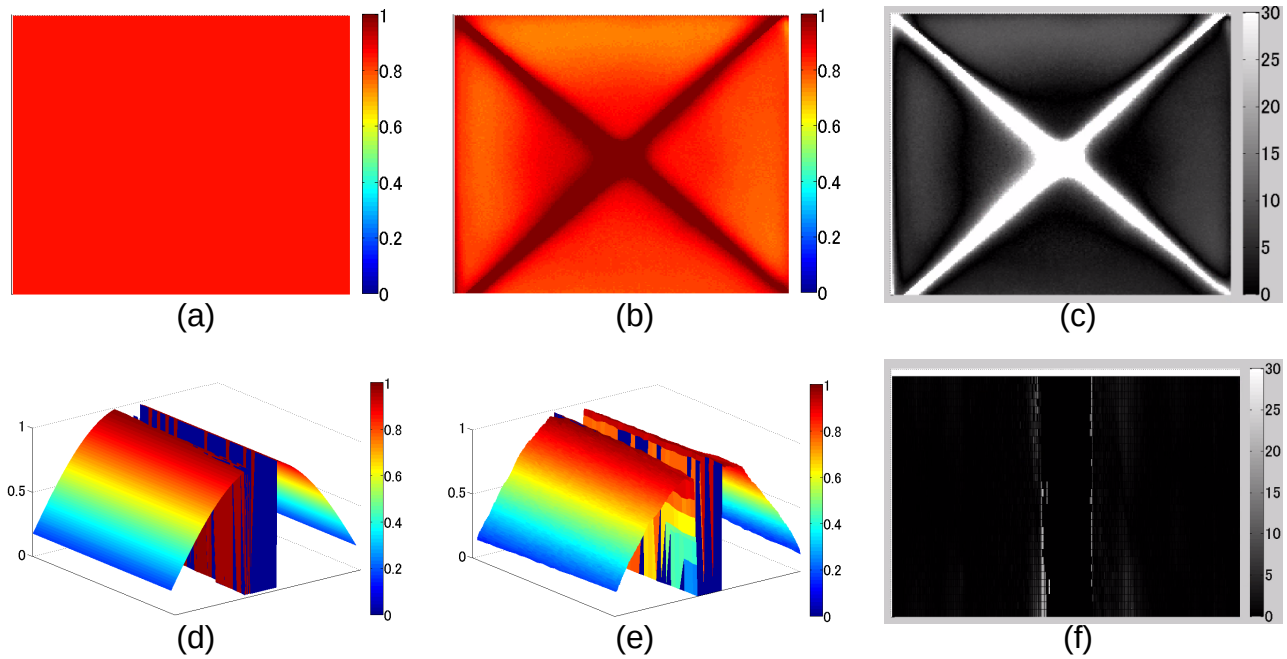

Figure 4.4: Incident angle estimation results. Upper images are results of quadrangular pyramid object. Bottom images are results of cylindrical object. (a) and (d) show ground truth of incident angle in polar coordinate. (b) and (d) show estimated incident angle in polar coordinate. (c) and (e) show estimated error in degree.

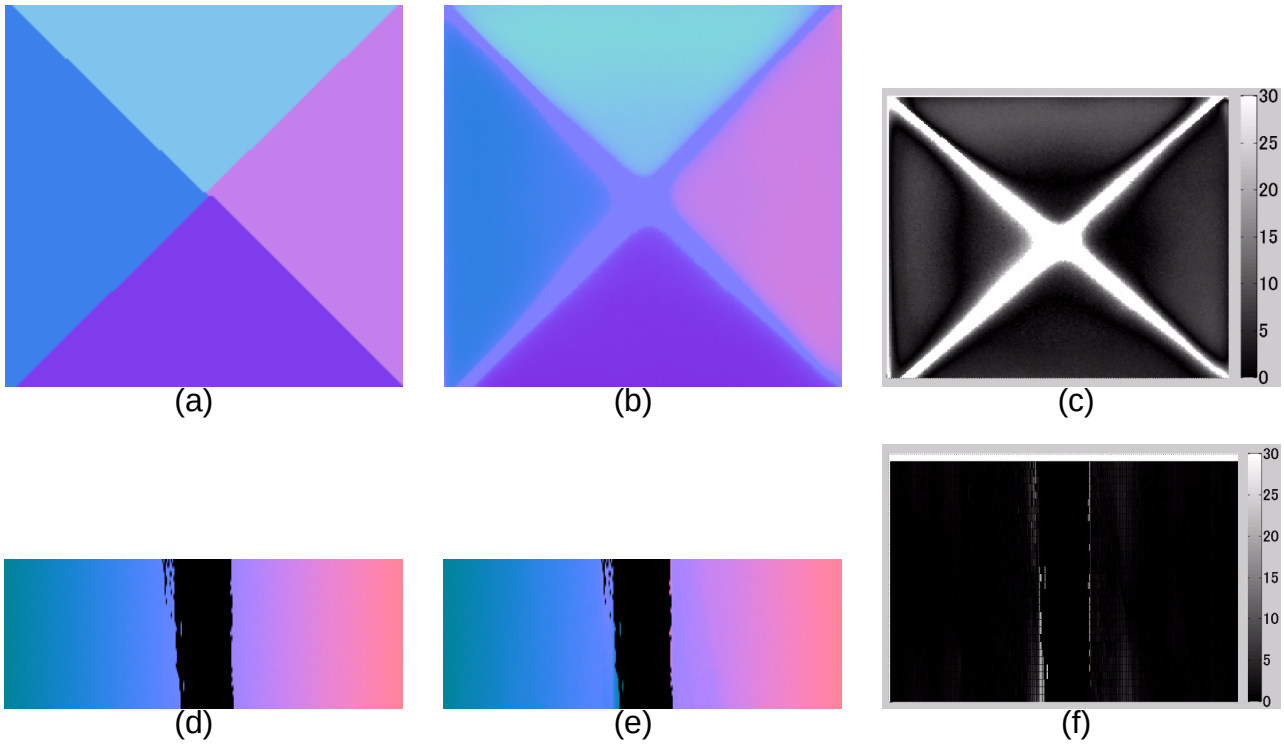

Figure 4.5: Surface normal estimation result. Upper images are results of quadrangular pyramid object. Bottom images are results of cylindrical object. (a) and (d) show ground truth of surface normal. (b) and (d) show estimated surface normal. (c) and (e) show estimated error in degree.

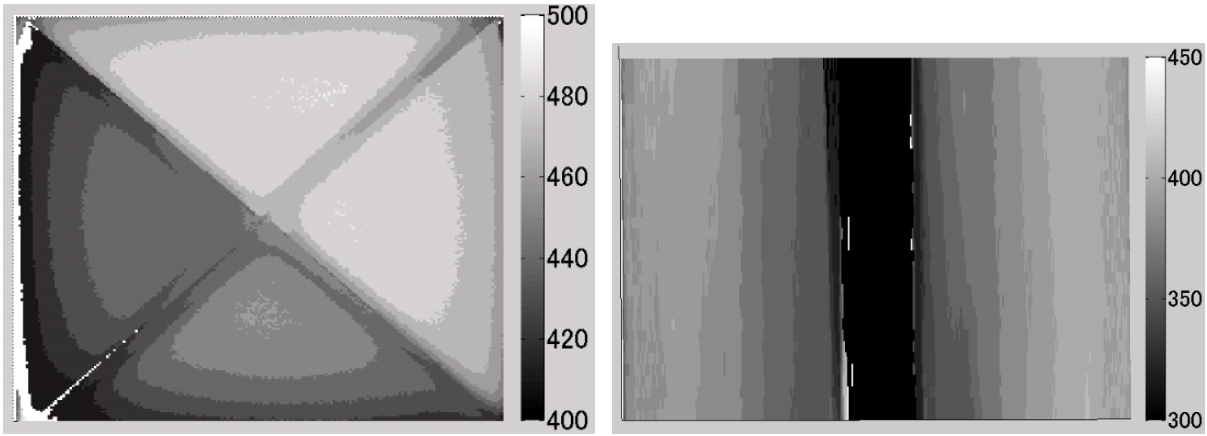

(a) Estimated film Thickness of cylindrical object

(b) Estimated film Thickness of quadrangular pyramid object

Figure 4.6: Film thickness estimation results.

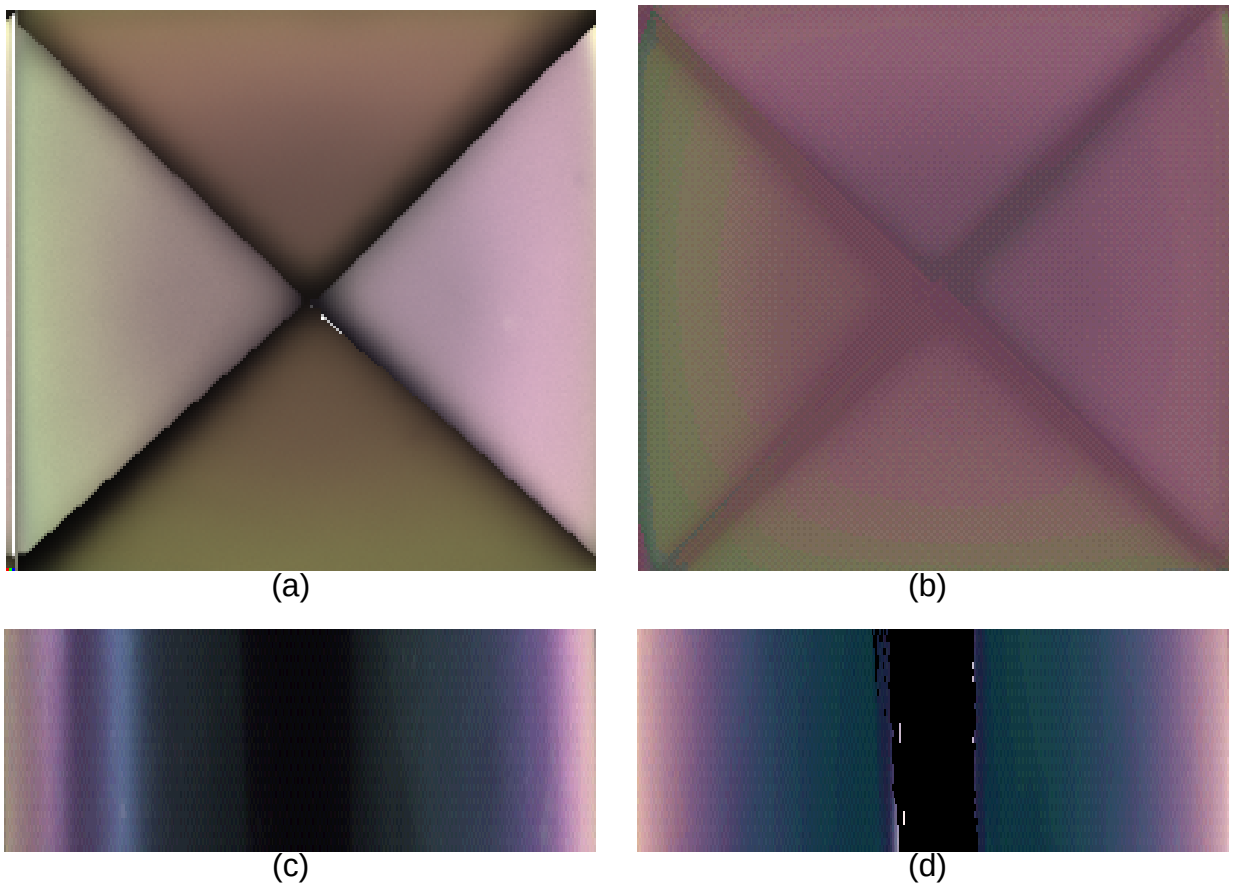

Figure 4.7: Captured images and reconstructed images. (a) and (c) show reflectance images captured by a hyper-spectral camera. (b) and (d) show reconstructed images by estimated incident angle, refractive index and film thickness.

Chapter 5

Shape and Film Thickness Estimation of Non-Planar Objects by RGB images

5.1 Overview

In Chapter 4, we developed equipment to acquire the reflectance spectra of thin film objects at once. We also proposed a method to estimate shapes of thin film objects with non-planar surfaces. This equipment needs a polarizer film in front of objects and a hyper-spectral camera. This has two problems. First, setting a polarizer needs severe setup. Second, a hyper-spectral camera is usually too expensive. Solving these problems, we propose a novel method to reconstruct the shapes and appearances of thin film objects using conventional digital still camera without a polarizer film in front of a target object.

The rest of this chapter is as follows. In Chapter 5.2, we propose a method to estimate shapes by RGB images. In Chapter 5.3, we summarize the procedure of estimation method and introduce a method to estimate film thickness. In Chapter 5.4, we conduct experiments by the simulation and real data to evaluate our method. In Chapter 5.5, we summarize this chapter.

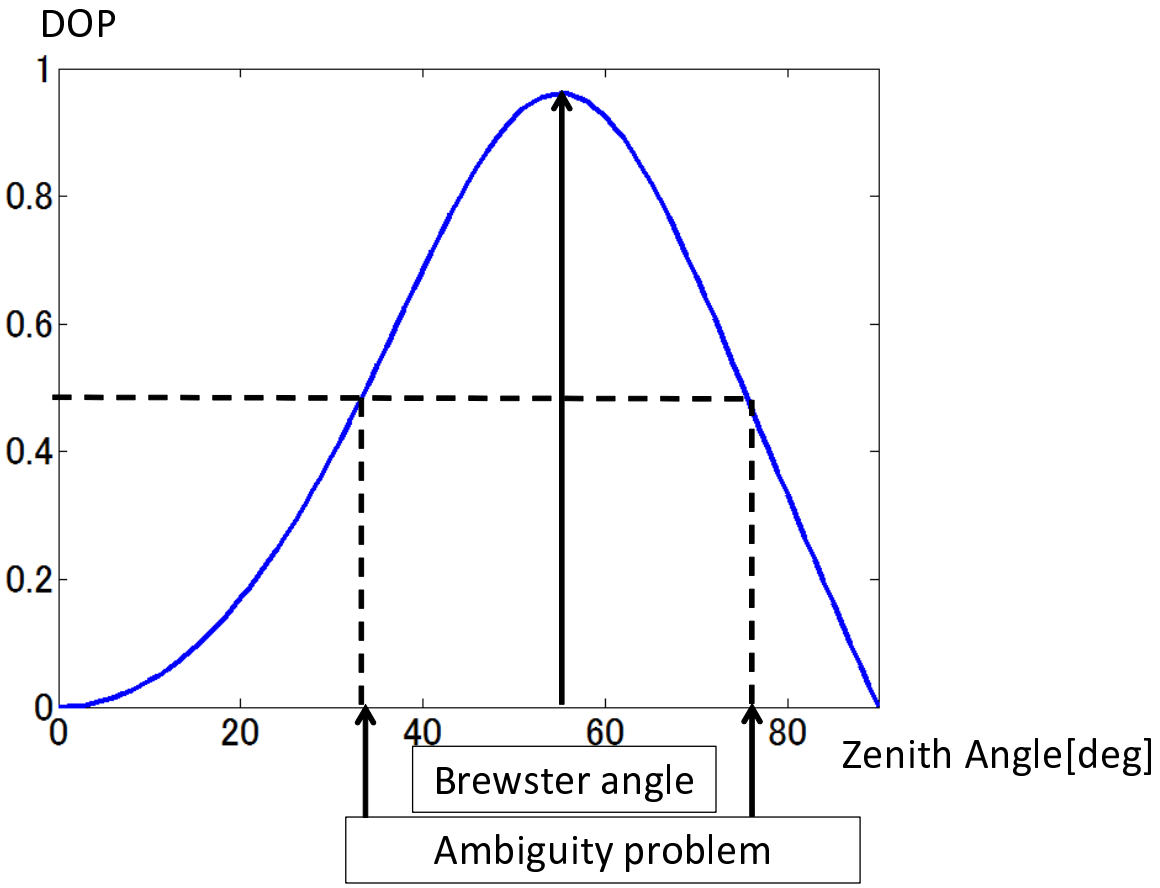

Figure 5.1: Degree of polarization. Refractive index of thin film and bottom layer is 1.36 and 1.6 respectively.

5.2 Shape Estimation

In this section, we describe the shape estimation method using the polarization and intensity of reflectance. Our method has two steps to estimate the surface orientation whose parameters are zenith and azimuth angles. The method to estimate azimuth angles is the same as mentioned in Section 4.

5.2.1 Polarization

The Light has characteristics of electromagnetic wave. The polarization of reflected light can be divided into the parallel and perpendicular polarization. The parallel

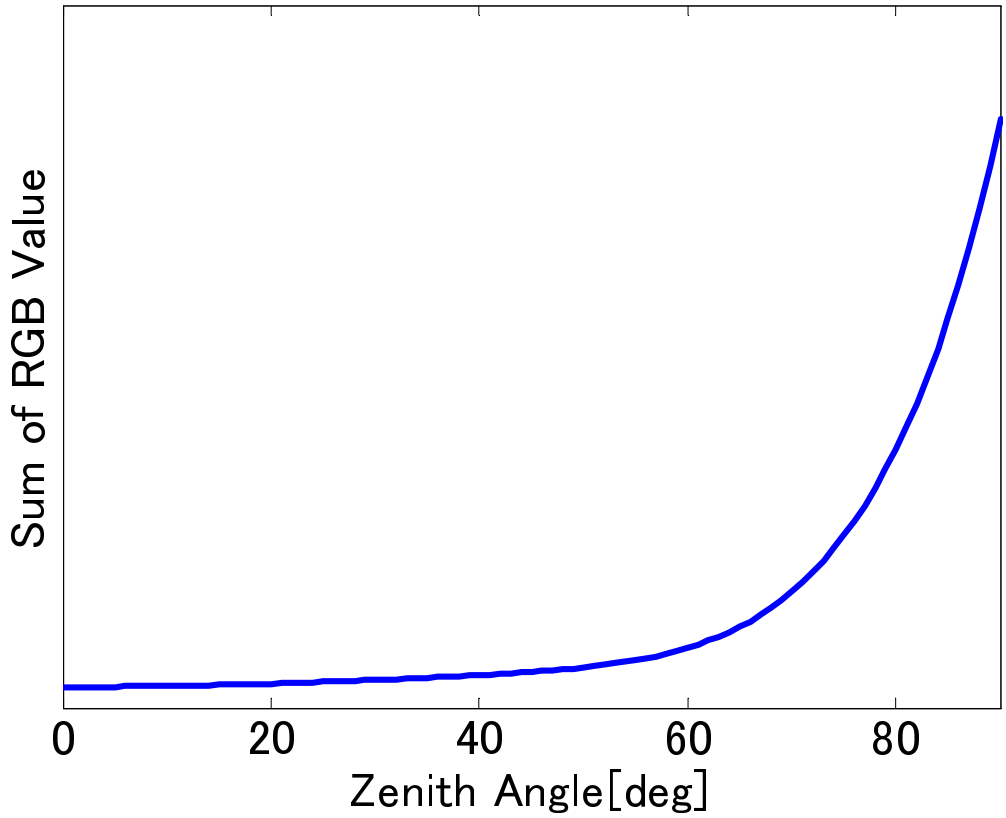

Figure 5.2: Sum of RGB values along zenith angle. The refractive index of thin film is 1.36. That of bottom layer is 1.6. The film thickness is 400 nm. The sensitivity of camera is EOS 5D[60].

polarization is parallel light along the incident plane. The perpendicular polarization is vertical light along the incident plane. As shown in Fig. 4.2, the azimuth angle is vertical along the incident plane, and then the perpendicular polarization is parallel to the azimuth angle.

5.2.2 Zenith Angle

We focus on two features to estimate zenith angles. The first feature is the degree of polarization (DOP) that can narrow down candidates in two zenith angles. The second feature is that the intensity of perpendicular polarization monotonically increases. In this section, we describe a method to estimate zenith angles using them.

When the polarizer is rotated, the observed intensity is changed in the rotating angle. DOP is defined by the maximum intensity and minimum intensity among polarized images. Fig. 4.2 shows a graph of DOP, which is captured by rotating polarizer. DOP is represented by the following equation.

$$\rho = \frac{I_{max} - I_{min}}{I_{max} + I_{min}} \tag{5.1}$$

The I_{max} and the I_{min} can be theoretically defined by the amplitude of Fresnel reflection and transmittance. Considering the effect of the reflection at the bottom layer as shown in Fig. 2.1, I_{max} and I_{min} are as follows.

$$\begin{aligned} I_{max} &= I_S \\ &= (R(T)_s + T(T)_s R(B)_s T(B)_s) I \end{aligned} \tag{5.2}$$

$$\begin{aligned} I_{min} &= I_P \\ &= (R(T)_p + T(T)_p R(B)_p T(B)_p) I \end{aligned} \tag{5.3}$$

where $R(T)_s$, $R(T)_p$ are the reflection of the top layer, $R(B)_s$, $R(B)_p$ are the reflection of the bottom layer. And $T(T)_s$, $T(T)_p$ are the transmittance coefficients of the top layer, $T(B)_s$, $T(B)_p$ are the transmittance coefficients of bottom layer.

The amplitude of the Fresnel reflection and transmittance at the top layer are represented as Eq. (5.4), (5.5), (5.6), and (5.7). In the case of the bottom layer, the equations can be similar with top layer's equations. n_1, n_2 and n_3 are the refractive indexes of incoming medium, thin film and outgoing medium respectively. θ_1 is the zenith angle. θ_2 is the refracting angle. θ_3 is the angle of outgoing light transmitting to the thin film.

$$R(T)_s = \left| \frac{n_1 \cos\theta_1 - n_2 \cos\theta_2}{\cos\theta_1 + n_2 \cos\theta_2} \right|^2 \tag{5.4}$$

$$R(T)_p = \left| \frac{n_2 \cos\theta_1 - \cos\theta_2}{n_2 \cos\theta_1 + \cos\theta_2} \right|^2 \tag{5.5}$$

$$T(T)_s = \frac{\tan\theta_1}{\tan\theta_2} \left| \frac{2 \sin\theta_2 \cos\theta_1}{\sin(\theta_1 + \theta_2)} \right|^2 \tag{5.6}$$

$$T(T)_p = \frac{\tan\theta_1}{\tan\theta_2} \left| \frac{2 \sin\theta_2 \cos\theta_1}{\sin(\theta_1 + \theta_2)\cos(\theta_1 - \theta_2)} \right|^2 \tag{5.7}$$

Here, we can calculate the DOP along the zenith angle if we know the refractive index of thin film and bottom layer.

Fig. 5.1 shows the DOP of the thin film, whose refractive indexes of the thin film and bottom layer are 1.36 and 1.6 respectively. The vertical axis shows the value of DOP. The horizontal axis is the zenith angle from 0 to 90 degrees. As shown in Fig. ¥ reffig:dop, the DOP has two solutions across Brewster angle.

Solving before ambiguity, we come up with the following method. We segment two regions which are divided by ”Brewster angle” in Fig. 5.1. ”Larger region” has larger angle than ”Brewster angle”. ”Smaller region” has smaller angle than ”Brewster angle”. The intensity of perpendicular polarization monotonically increases along zenith angles from Eq. (5.2), (5.4) and (5.6). When the intensity becomes larger than that of ”Brewster angle”, we can determine that region as ”Larger region”. Then, we can detect the zenith angle in ”Larger region”. When the intensity is smaller than that of ”Brewster angle”, we can determine in the similar way.

5.3 Shape and Appearance Estimation

In this section, we introduce novel measurement equipment for measuring the appearance of thin film objects. And, we also explain the procedure of the estimation method of both shape and film thickness using the equipment and our proposed method.

5.3.1 Measurement Equipment

Fig. 5.3 shows the measurement equipment for polarized images of thin film objects. The setup of our measurement equipment consists of a geodesic dome, a LED light, a white plastic sphere as a diffuser, an RGB camera, and a linear polarizer. The spectrum of an LED light is similar with the spectrum of daylight illumination. We use Canon EOS 5D Mark2 as a conventional RGB camera, whose sensitivity is measured by Kawakami et al.[60].

Using this equipment, we can capture the reflectance images of the whole surface at once. Because the interference light can be observed when the incident angle of

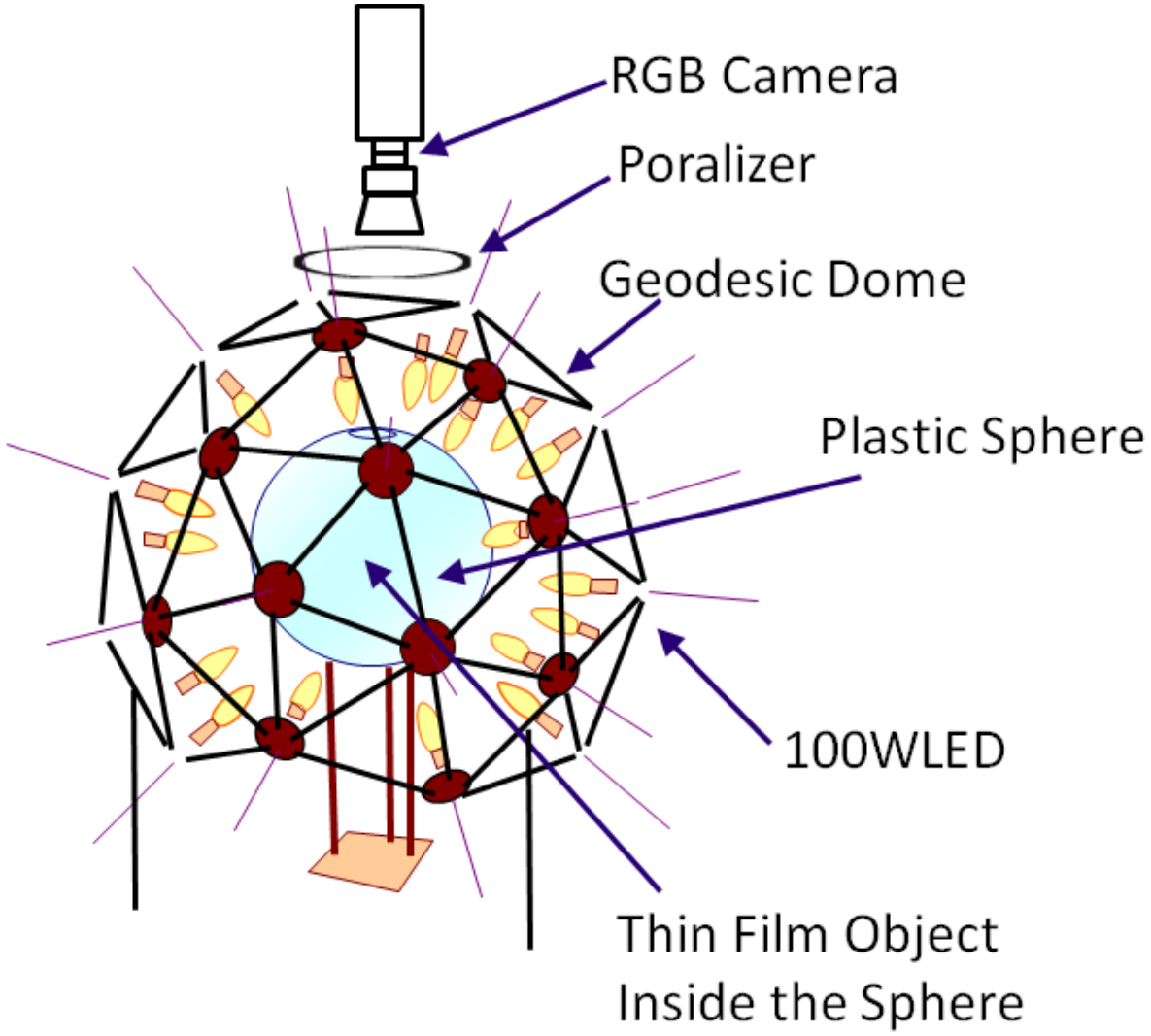

Figure 5.3: Measurement equipment of our method. We put LED light on top of icosahedron and white plastic sphere inside it to make omnidirectional light environment. We also put RGB camera on top of sphere and capture polarized image.

light and the observed angle on normal are only the same. Therefore, we develop the illumination environment for observing interference light on whole surface. We put LED light on the vertex of the geodesic dome, then we put a plastic sphere for diffusing the light. Then, we can illuminate a target object omnidirectionally.

5.3.2 Procedure of Shape Estimation

Fig. 5.4 shows the procedure to estimate the shape of thin film objects. The estimation method is roughly divided into three steps. First, we capture polarized images by rotating the polarizer from 0 to 180 degrees by 10 degrees. Other two steps are for estimating the zenith and azimuth angles. These two steps are independent each other, and then we can estimate zenith or azimuth angle independently.

The steps of the zenith angle estimation are as follows. First, we store pixel intensities in captured image sequence. Second, we detect the maximum and minimum intensity in captured image sequence and calculate DOP in each pixel. Third, using the calculated DOP, we determine two candidates of the zenith angles. Finally, we estimate the zenith angle using Section 5.2.2.

The azimuth angle estimation is as follows. First, we detect the angle of the maximum intensity in each pixel of captured image sequence. Next, the azimuth angles in the whole region can be estimated using the method in section 4.2.2.

5.3.3 Procedure for Appearance Reconstruction

We propose a method to estimate the film thickness in this section. If we know the refractive index of both thin film and bottom layer, we can simulate the color along the zenith angle and the film thickness as shown in Fig. 5.5. We can estimate the film thickness detecting the correspondence between the simulated RGB value and observed RGB value. Here, there are some ambiguities since the similar color repeats along the film thickness in Fig. 5.5. Therefore, we assume that the rough range of the film thickness is known.

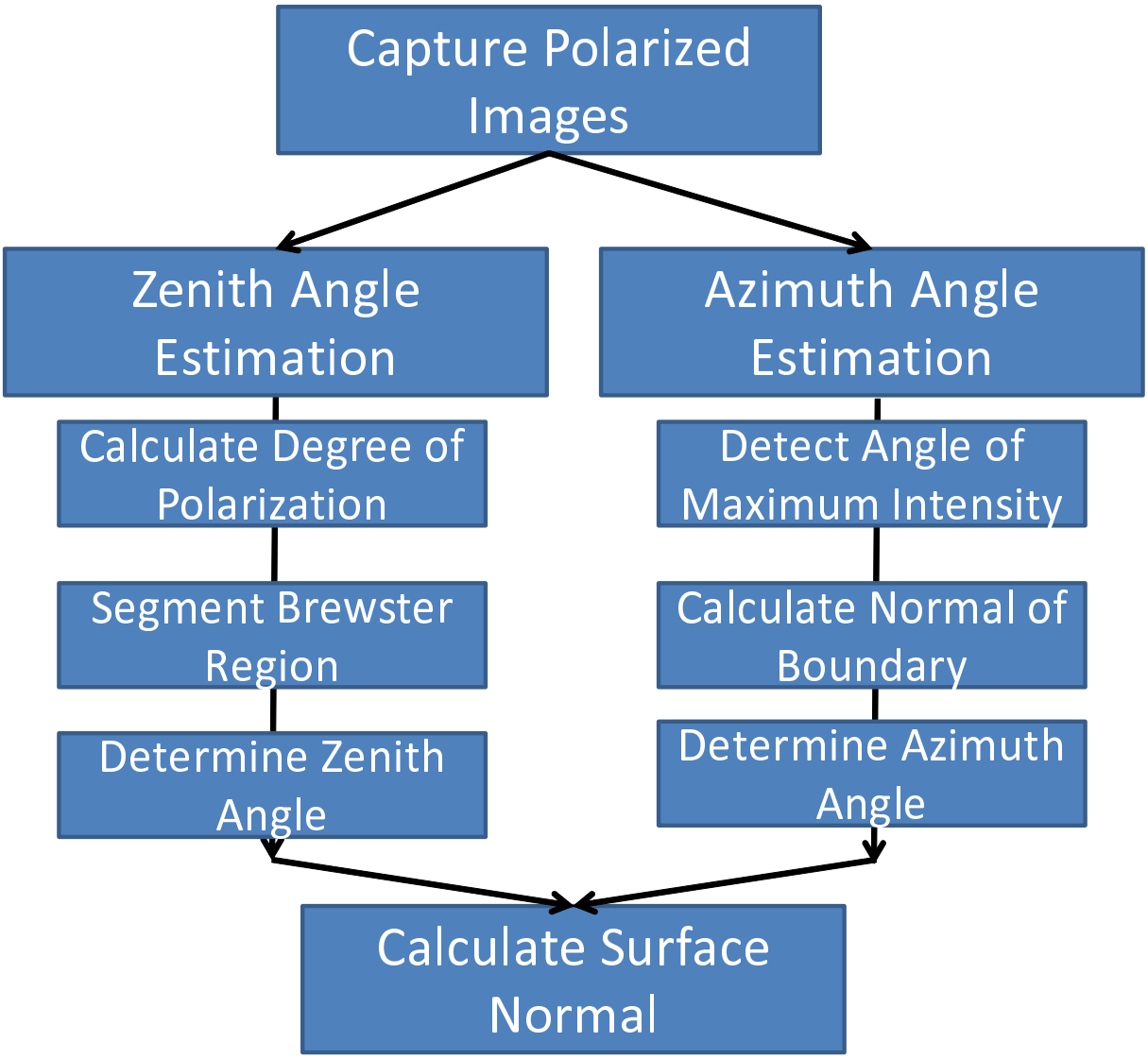

Figure 5.4: Flow chart of our method

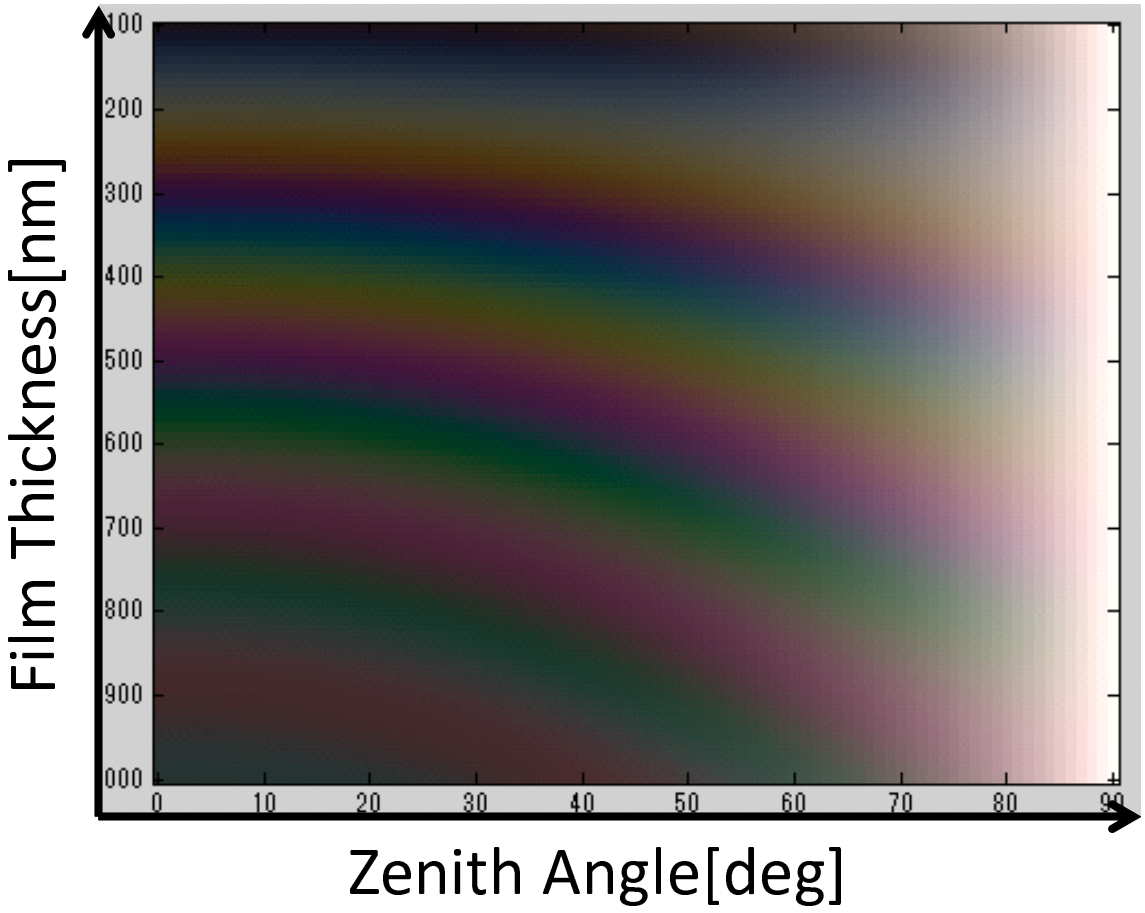

Figure 5.5: Simulated appearance along zenith angle and film thickness. Zenith angle is from 0 to 90 degrees. Film thickness is from 100 nm to 1000 nm. The refractive index of thin film is 1.36. That of bottom layer is 1.6.

Table 5.1: Estimated Thickness and RMSE of Measured Reflectance

Zenith Angle [deg]	Estimated Thickness [nm]	RMSE[%]
10	629	1.20
15	618	1.44
20	630	1.05
25	632	0.87
30	628	0.99
35	624	1.45
40	626	1.18
45	639	1.13
50	661	1.31

5.4 Experiment

In this Section, we investigate the validity of our method by simulation. Furthermore, we verify the effectiveness of our method to real objects.

5.4.1 Simulation

We use the reflectance spectra measured by the spectrometer as input data. We put the target object and light source on the rotation table and change the zenith angle. We change zenith angle from 10 to 50 degrees by 5 degrees. The material of the thin film is MgF_2 whose refractive index is 1.36. The material of the bottom layer is a PET film whose refractive index is 1.6. The ground truth of the film thickness is 630 nm. We calculate RGB by Canon EOS 5D Mark2 sensitivity measured by Kawakami et al. [60].

Tab. 5.1 shows the estimated film thickness. The average error is 6.56 nm. At 15 and 50 degrees, the error is over 10 nm.

In this section, we verified the accuracy of the estimated film thickness. For shape estimation the accuracy depends on a method of zenith and azimuth angles estimation. As mentioned in Section 5.2, we use DOP to estimate these angles. Several methods [51][11][12] use the DOP for shape estimation, then they already evaluate the accuracy

of DOP. Therefore, in this section, we verify the accuracy of film thickness estimation.

5.4.2 Real Data Experiment

In this experiment, we used a cylindrical object, and a quadrangular pyramid button on which MgF2 are evaporated. The bottom layer of the cylindrical object is a PET lm whose refractive index is 1.6, and whose lm thickness is 400nm. It was a rolled-up evaporated planar lm using an accurate cylinder object.

The quadrangular pyramid object is made of ABS resin whose refractive index is 1.5. MgF2 was directly evaporated on their surfaces whose lm thickness is 630 nm. The physical vapor deposition is generally used for a planar object, and then it is not guaranteed that the evaporated lm thickness is uniform on non-planar objects. However, our method can measure the spatial normal on a non-planar object.

First, we show the estimated results of the zenith angle in Figs. 5.6. Fig. 5.6.(b) shows the estimated zenith angle. The middle area of Fig. 5.6 is faced to the hole of the plastic sphere of the geodesic dome. We captured images thorough this hole, then we got empty results in this area for the cylindrical object.

Second, we show the estimated surface normal and its error in Fig. 5.7. The top bottom of Fig. 5.7 shows the results of the cylindrical object. The average error becomes 4.48 degrees. The lower bottom of Fig. 5.9 shows the results of the quadrangular pyramid object. The average error is 2.82 degrees. Fig. 5.7.(c) show the errors of the angles between the ground truth and estimated surface normals.

Third, Fig. 5.8 show the results of the estimated lm thickness. The thickness is around 400 nm for the cylindrical object. However, the thickness of the quadrangular pyramid object varied greatly from 400 nm to 690 nm.

Finally, we show the reconstructed images using our method in Fig. 5.9. Then, we evaluated the color difference between the captured and reconstructed images. The color difference is dened by Eq. (2.20) in CIE LAB color space. Tab 2.2 represents the dierence in human perception between two colors. The color difference in the cylindrical object is 0.64, perceived as "Slight". The color difference in the quadrangular pyramid becomes 3.0, perceived as "Noticeable".

5.4.3 Discussion

In this section, we discuss errors of the simulation and real data experiment. First of all, we discuss the thickness error in simulation. We calculate RMSE between the input reectance spectra and spectra with the ground truth lm thickness. RMSE becomes larger at 15 and 50 degrees. This result represents that the input reectance is aected by some noise.

Next, we discuss the errors of the real data experiment. First, we consider that the errors are cause by the zenith angle errors and azimuth angle errors. The zenith angle errors in Fig. 5.6 are similar with the surface normal in Fig. 5.7. Hence the error of azimuth angle is almost zero.

Second, we consider that the error of the zenith angles is caused by the stability of intensity in the lower angle as shown in Fig. 5.10. In this area, if the incident angle changes largely, the intensity is stable. For that, the estimated zenith angle would be sensitive to the change by noise.

Third, we cannot know the ground truth of the thickness in Figs. 5.8. However, we can recognize the smooth spatial thickness of both objects.

Finally, we discuss the dierence of the reconstructed appearances. In our method, we achieve the estimation of the optical parameters of the thin lm, such as the spatial normal and thickness using a conventional digital still camera. As a result, Fig. 5.9 (c) represents the complex appearance change of the thin lm. However, we must discuss the improvement method for more accurate reconstruction.

5.5 Summary

We proposed a novel method to estimate shapes and appearances of thin lm objects using RGB images. By our method, we can reconstruct thin lm objects as CG more easily because our method use conventional a digital still camera whose data size is smaller than a spectral sensor. Furthermore, we developed the measurement equipment to capture the whole reectance images of thin lm objects at once. In our experiment, we showed the accuracy of the estimated shapes and appearances by our method.

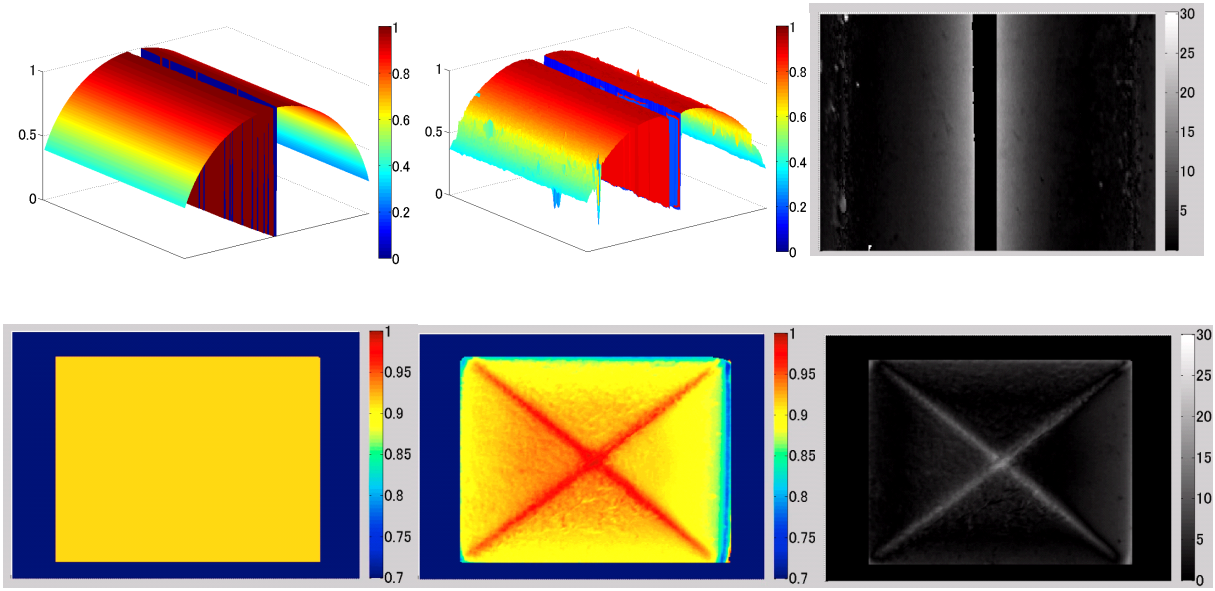

Figure 5.6: Estimated results of zenith angle. (a) is ground truth in polar coordinates. (b) is estimated zenith angle in polar coordinates. (c) is estimation error in degrees.

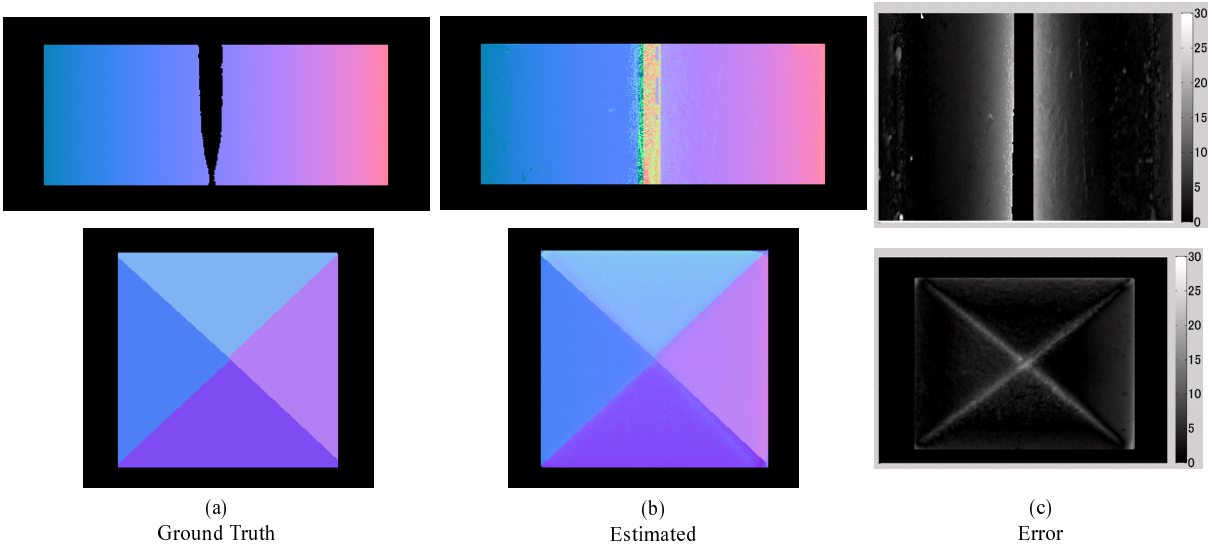

Figure 5.7: Estimated results of surface normal. (a) is ground truth. (b) is estimated surface normal. (c) is estimation error in degrees.

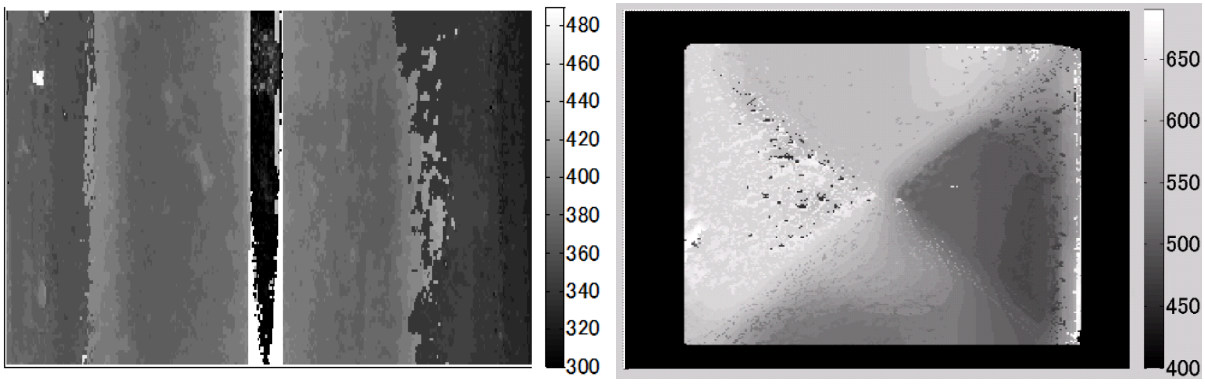

(a) Cylinder (b) Quadrangular pyramid

Figure 5.8: Estimated results of film thickness. (a) and (b) are results of cylindrical object and quadrangular pyramid respectively.

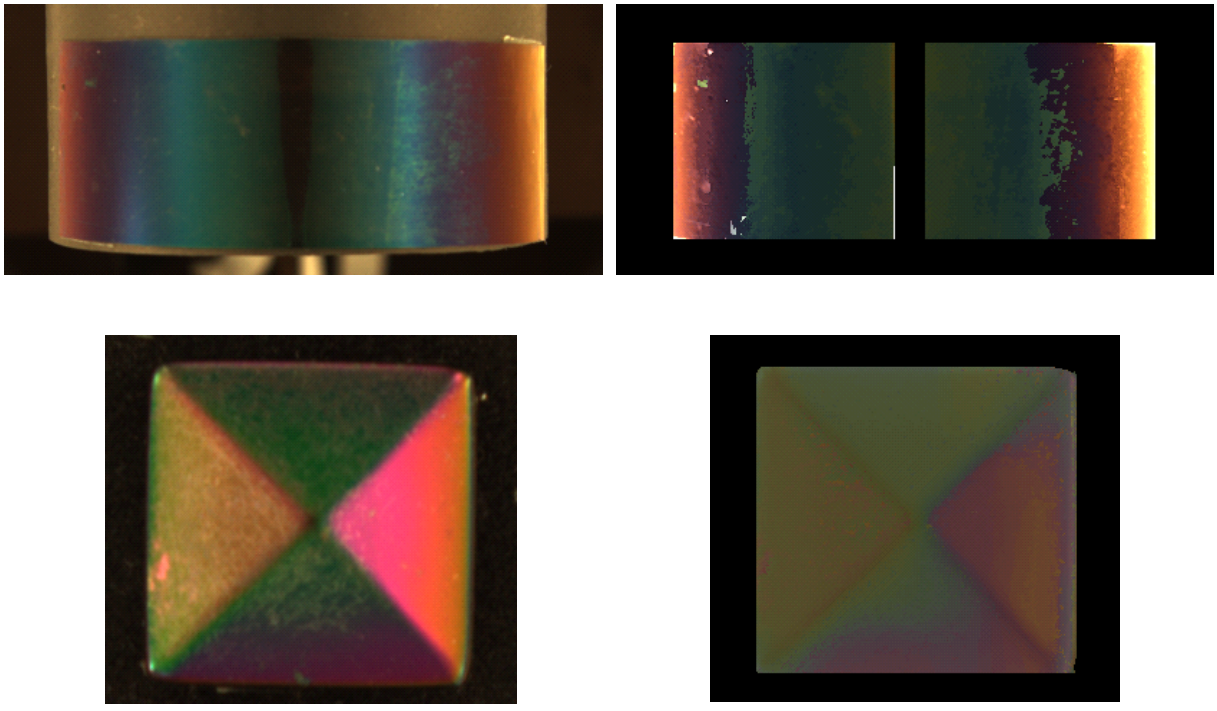

(a) Captured Polarized Image (b) Synthesized Image

Figure 5.9: Captured polarized image and reconstructed image with estimated shapes and film thickness.

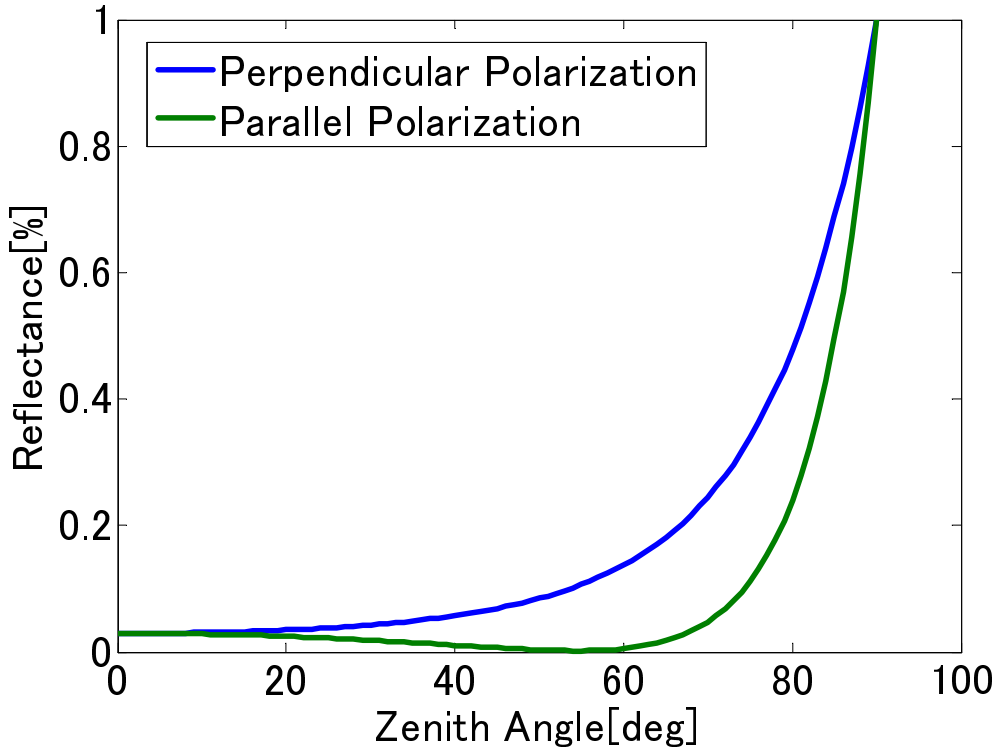

Figure 5.10: Reflectance of perpendicular and parallel polarization. Reflectance is percentage of reflected light from object. The refractive index of film is 1.36. That of bottom layer is 1.6.

Chapter 6

Conclusions

6.1 Summary

The ultimate goal of this dissertation is to model real objects with thin film coating on its surface and reconstruct modeling result as CG. To achieve this goal, we proposed following methods.

Firstly, we proposed a method to estimate a refractive index and film thickness from hyper-spectral images. The refractive index and film thickness are parameters of reflectance model of a thin film. Therefore, we need them to reconstruct appearances of a thin film.

Secondly, we proposed a novel method to estimate shapes of thin film objects using hyper-spectral images. To simplify, we also introduced a shape estimation method using RGB images.

Finally, we developed equipment to measure reflectance of non-planar objects with a thin film coating. We also applied our methods to real objects with thin film coating.

6.1.1 Refractive Index and Film Thickness Estimation of Planar Objects

We proposed a method to estimate a refractive index and film thickness simultaneously. We focused on the peak wavelength where the optical path difference is equal to

an integral multiple. With the peak wavelength, the refractive index can be defined in a compact way. Using the peak wavelength and the estimated refractive index, we can narrow down the candidates of the film thickness, and easily estimate the film thickness with them by the least square error between measured reflectance and reflectance model.

The conventional methods such as ellipsometry or interference spectroscopy can only measure one point at once. Therefore, they can not represent spatially varying appearances which are caused by changing of film thickness.

In the experiment, we estimated refractive index and film thickness of planar objects. The reconstructed results showed that our method work well. However, the result also showed the limitation of our method that we could not estimate well with larger refractive index. The results also shows the limitation of our method that we can not estimate with high accuracy with larger refractive index which make the interval of the nearby peak wavelength smaller than wavelength sampling rates. However, this can be solved by using small interval of spectrum sampling.

6.1.2 Shape, Refractive Index, and Film Thickness Estimation of Non-Planar Objects Using Hyper-Spectral Images

We proposed a method to estimate shapes and optical parameters of non-planar objects with a thin film. We focus on the peak intensity to estimate incident angle since the peak intensity only depends on the refractive index of a bottom layer and an incident anlge. To estimate optical parameters, we squeeze candidates of film thickness focusing on the peak wavelength and minimize the least square error between measured and model reflectance. In the experiment, we showed an accuracy of estimated incident angles and optical parameters. We also showed that estimation errors were caused by measurement noise of spectrometer and detection errors of peak wavelength. This result showed that our method theoritically work well for real data objects.

6.1.3 Measurement Equipment for Thin Film Objects with Non-Planar Surfaces

We developed equipment to measure reflectance of thin film interference. The reflectance of thin film can be observed only when incoming and reflection angle becomes equal. Using this feature, we can acquire the reflectance of non-planar objects at once by omni-directional illumination environment. Therefore, we put light sources around white plastic sphere, and set target thin film object in the sphere, then we acquired reflectance at once. In the experiment, we measured reflectance and estimated shapes and optical parameters. We also reconstructed images and showed that our method works well.

6.1.4 Shape and Film Thickness Estimation of Non-Planar Objects by RGB images

We proposed a novel method to estimate shapes and appearances of thin film objects using RGB images. By our method, we can reconstruct thin film objects as CG more easily because our method use a conventional digital still camera whose data size is smaller than spectral sensor. Furthermore, we developed measurement equipment to capture whole reflectance images of thin film objects at once. In our experiment, we showed the accuracy of estimated shapes and appearances of our method.

6.2 Contribution

In this dissertation, we have proposed a framework for modeling thin film objects. The framework includes both acquisition of shapes and appearances, and measurement equipment of reflectance. For acquisition of shapes and appearances, we have proposed two methods: One method is based on hyper-spectral images. The other one is based on RGB images. For measurement equipment, we developed equipment to measure reflectance of non-planar objects at once. We summarize our contributions as follows.

1. Development of a method to estimate optical parameters by hyper-spectral images

In optics fields, several methods were proposed to estimate film thickness which is the appearance parameter of a thin film. However, these methods assume that refractive index is known. Furthermore, they can only measure one point at once, and then it is time consuming to acquire spatially varying film thickness of a target object. We focused on the peak wavelength which can represent the refractive index in a compact way. In addition, we can narrow down the candidates of film thickness by the peak wavelength and reduce the computational cost to estimate spatially varying film thickness.

2. Development of a method to estimate shapes and appearances of thin film objects by hyper-spectral images

In computer vision fields, there are various methods to acquire object shapes. However, it is difficult to apply to thin film objects because of complicated reflectance of them. We proposed a novel method to estimate shapes of thin film objects focusing on extremal intensity of reflectance. We have found that extremal intensity is only dependent on the refractive index of a bottom layer and an incident angle. Furthermore, we found that we can apply the characteristics strip expansion method and polarization analysis to thin film objects, then we can estimate an azimuth angle. By the estimated incident angle and azimuth angle, we can acquire the surface normal of the target thin film object. We also estimate the refractive index and film thickness by calculating the least square error between measured reflectance and reflectance model. By this estimated results of shapes,the refractive index, and the film thickness, we reconstruct appearances of thin film objects.

3. Development of an equipment for measuring thin film reflectance

The reflectance of a thin film is observed when incoming and reflection angle become equal. Therefore, we must illuminate thin film objects from several directions to measure reflectance. However, it is time consuming to change illumination directions

and measure reflectance one by one. So we developed an omnidirectional illumination environment equipment. Using this equipment, we can measure reflectance of thin film objects at once.

4. Development of a method to estimate shapes and film thickness by RGB images

The measurement method using hyper-spectral images needs complicated setting of a polarizer both in front of a camera and an object. To simplify this method, we use RGB images without polarizer in front of object. By this simplification, we can reduce data of measured reflectance and measuring time comparing with the spectral method.

6.3 Future Work and Discussion

In this dissertation, we have proposed some techniques for modeling thin film objects. In this section, we describe future work of our approach, and improvement of our method.

6.3.1 Expansion of Shapes and Appearances Estimation using RGB Images

Currently, shapes and appearances estimation method by RGB images assume that the refractive index of a thin film is known. However, it is not easy to acquire refractive index from an unknown material without destroying or deforming original objects. The method by using RGB images uses the degree of polarization which is defined by the incident angle and refractive index of a thin film. If we can acquire some degrees of polarization with known lighting directions, and incident angles, we are probably able to estimate the refractive index of a thin film. Expanding the measurement equipment to control lighting directions, we might be able to estimate the refractive index of a thin film by a non-destructive way.

6.3.2 Shapes and Appearances Estimation of Multi-Layer Film Object by Expanding Our Method

The proposed method is only for one layer, however we have much more objects which has multi-layer structure especially for cultural heritages. The multi-layer film has close structure to a thin film. Therefore, the basic idea of our method can be applied to multi-layer film objects. Using methods in this dissertation as basic idea, we will be able to expand our method for multi-layer film objects.

6.3.3 Reflectance Analysis and Estimation of Thin Film Objects with Concave Shape

Proposed techniques in this dissertation assume that a target object has convex shapes. If the thin film object has a concave shape, the reflected light on the object's surface has interreflection effects at surfaces face each other. The interreflection of the reflected light makes reflectance of a thin film more complicated because it might be caused interference again on the surface face each other. Therefore, we need to observe and analyze the interreflection of a thin film to acquire shapes and appearances of thin film objects with concave shapes.

6.3.4 Fabrication from estimated shapes and optical parameters

By proposed methods, we can fabricate thin film objects close to the target thin film objects. Recently, 3D objects can be acquired by a 3D printer. We can coat thin film to 3D objects by physical vapor deposition. Therefore, we can make an accurate imitation of the target objects by these equipment.

Appendix A

Polarization

A.1 Overview

We use the knowledge of polarization in this dissertation. However, we do not explain the detail of polarization because this is not the essence of our proposed methods. In this chapter, we explain polarization as a physical phenomena.

A.2 Polarization

The polarization is the electro magnetic light wave which vibrates to specific directions. In nature world, the light wave vibrates to all directions, thus the light is called unpolarized light or natural light. Usually, the vibrated direction of light wave is divided into two orthogonal directions. We can acquire polarized light from natural light through a crystal or optical filter called polarizer.

We have three types of polarization, linear polarization, circular polarization, and elliptically polarization. The vibrating directions of light wave is shown in Fig. A.1. The magnetic field of linear polarization vibrates to only one direction. The magnetic field of circular polarization is in a circle by propagation of vibrating. The elliptically polarization is most general polarization type. It draws ellipse in the magnetic field and has right and left optical rotation.

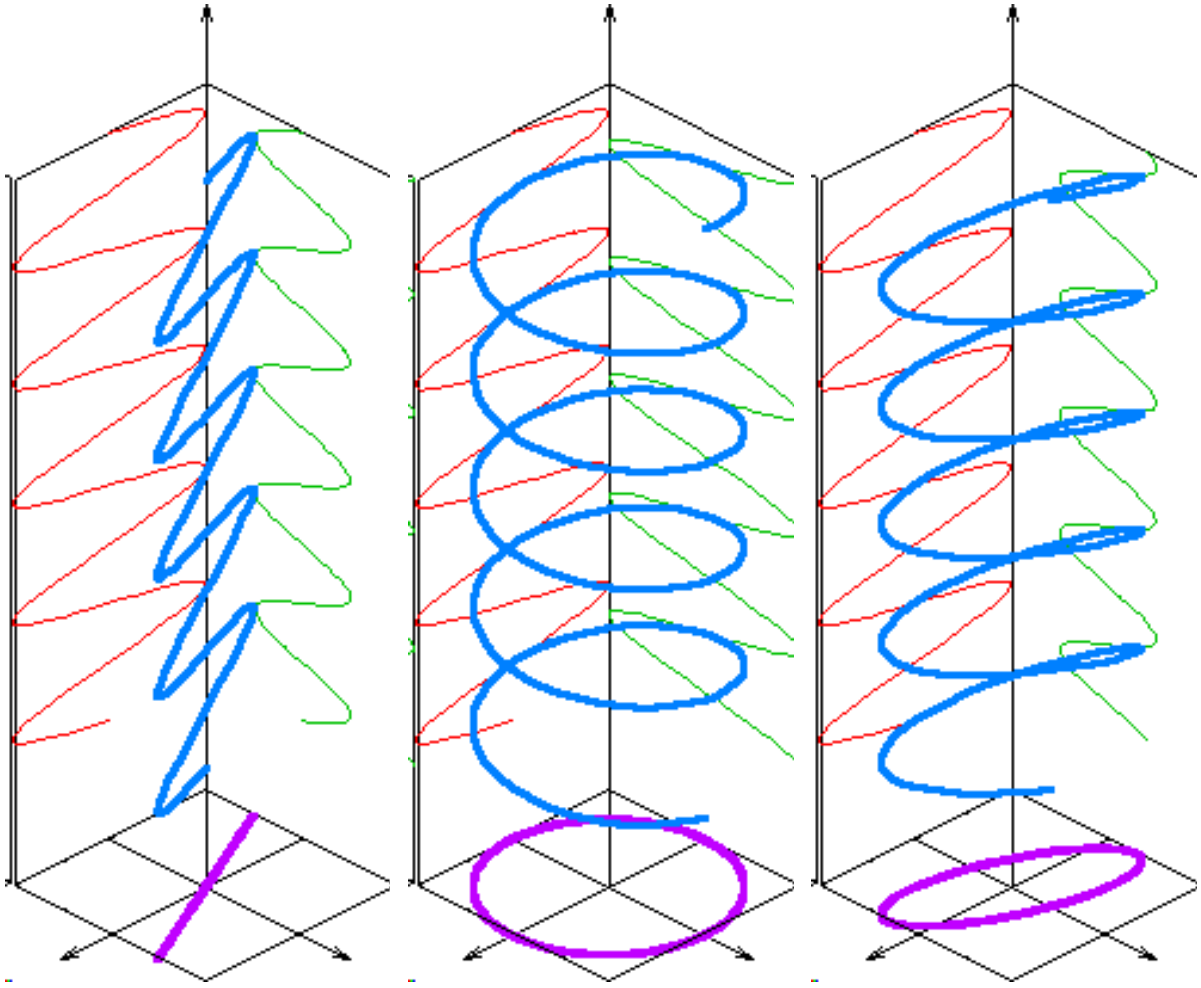

Figure A.1: Three types of polarization.

Among these types of polarization, we focus on the linear polarization. The linear polarization can be described by two components: perpendicular polarization and parallel polarization. The perpendicular polarization is vertical to plane of incidence between incoming lighting and z-axis as shown in Fig. A.2. The parallel polarization is parallel to plane of incidence. These components can be observed when incoming light reflects on object surface. Therefore, the linear polarization is used to shape reconstruction with complicated reflectance property in computer vision fields.

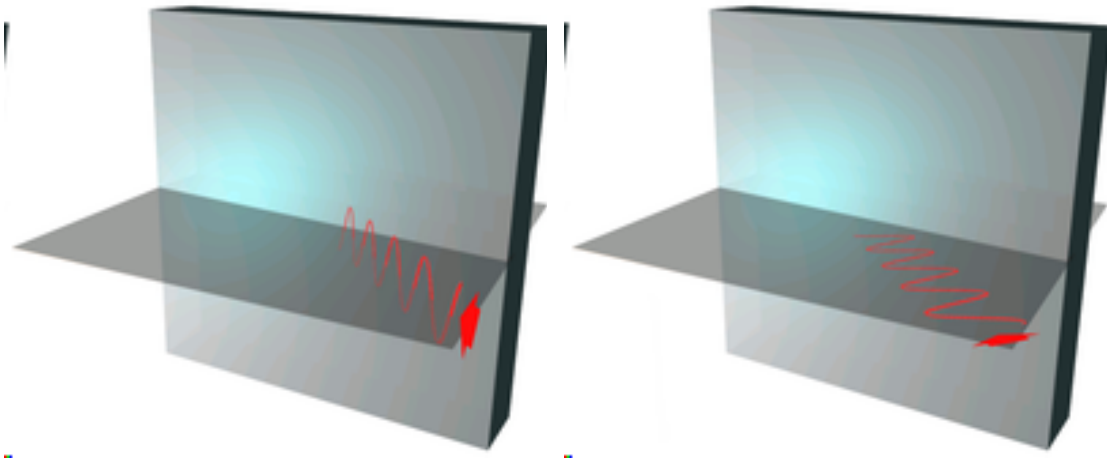

(a) Perpendicular Polarization (b) Parallel Polarization

Figure A.2: Relation between perpendicular and parallel polarization and plane of incidence.

References

[1] C. Hawley A. Abrams and R. Pless. Heliometric stereo: Shape from sun position. In P. Perona Y. Sato C. Schmid A. Fitzgibbon, S. Lazebnik, editor, *Computer Vision ECCV 2012*, volume 7573 of *Lecture Notes in Computer Science*, pages 357–370. Springer Berlin Heidelberg, 2012.

[2] M. Ashikhmin and P. Shirley. An anisotropic phong brdf model. *Journal of Graphics Tools*, 5:25–32, 2000.

[3] R. M. A. Azzam and N. M. Bashara. *Ellipsometry and polarized light*. North-Holland personal library. North-Holland Pub. Co., 1977.

[4] C. M. Herzinger R. Synowicki B. Johs, J. A. Woollam and C. L. Bungay. Overview of variable angle spectroscopic ellipsometry (vase) part 2: Advanced applications. In *Proc. SPIE CR72 (Optical Metrology)*, pages 29–58, 2000.

[5] J. F. Blinn. Seminal graphics. chapter Models of Light Reflection for Computer Synthesized Pictures, pages 103–109. ACM, New York, NY, USA, 1998.

[6] G. Borshukov and J. P. Lewis. Realistic human face rendering for "the matrix reloaded". In *ACM SIGGRAPH 2003 Sketches &Amp; Applications*, SIGGRAPH '03, pages 1–1, New York, NY, USA, 2003. ACM.

[7] G. Vogiatzis C. Hernandez and R. Cipolla. Multi-view photometric stereo. *EEE Transactions on Pattern Analysis and Machine Intelligence (TPAMI)*, 2008.

[8] P. R. Chang and T. H. Hsieh. Constrained nonlinear optimization approaches to color-signal separation. *Image Processing, IEEE Transactions on*, 4(1):81–94, Jan 1995.

[9] R. L. Cook and K. E. Torrance. A reflectance model for computer graphics. *ACM Trans. Graph.*, 1(1):7–24, January 1982.

[10] K. Hara D. Miyazaki and K. Ikeuchi. Median photometric stereo as applied to the segonko tumulus and museum objects. *International Journal of Computer Vision*, 86(2-3):229–242, 2010.

[11] M. Kagesawa D. Miyazaki and K. Ikeuchi. Determining shapes of transparent objects from two polarization images. In *in IAPR Workshop on Machine Vision Applications*, pages 26–31, 2002.

[12] M. Kagesawa D. Miyazaki and K. Ikeuchi. Transparent surface modeling from a pair of polarization images. *IEEE Trans. Pattern Analysis and Machine Intelligence*, 26:73–82, 2004.

[13] K. J. Dana. Brdf/btf measurement device. In *Computer Vision, 2001. ICCV 2001. Proceedings. Eighth IEEE International Conference on*, volume 2, pages 460–466 vol.2, 2001.

[14] K. J. Dana and J. Wang. Device for convenient measurement of spatially varying bidirectional reflectance. *J. Opt. Soc. Am. A*, 21(1):1–12, Jan 2004.

[15] M. S. Drew and G. D. Finlayson. Analytic solution for separating spectra into illumination and surface reflectance components. *J. Opt. Soc. Am. A*, 24(2):294–303, Feb 2007.

[16] K. E. Torrance E. P. F. Lafortune, S. C. Foo and D. P. Greenberg. Non-linear approximation of reflectance functions. In *Proceedings of the 24th Annual Conference on Computer Graphics and Interactive Techniques*, SIGGRAPH '97, pages 117–126, New York, NY, USA, 1997. ACM Press/Addison-Wesley Publishing Co.

[17] B. V. Funt G. D. Finlayson and K. Barnard. Color constancy under varying illumination. In *Computer Vision, 1995. Proceedings., Fifth International Conference on*, pages 720–725, Jun 1995.

[18] P. H. S. Torr G. Vogiatzis and R. Cipolla. Multi-view stereo via volumetric graph-cuts. In *Computer Vision and Pattern Recognition, 2005. CVPR 2005. IEEE Computer Society Conference on*, volume 2, pages 391–398 vol. 2, June 2005.

[19] M. Gong and Y. H. Yang. Fast unambiguous stereo matching using reliability-based dynamic programming. *Pattern Analysis and Machine Intelligence, IEEE Transactions on*, 27(6):998–1003, June 2005.

[20] H. Yamashita H. Hirayama, K. Kaneda and Y. Monden. An accurate illumination model for objects coated with multilayer films. *Computers and Graphics*, 25(3):391–400, 2001.

[21] K. Kaneda H. Yamashita H. Hirayama, Y. Yamaji and Y. Monden. Rendering iridescent colors appearing on natural objects. In *Computer Graphics and Applications, 2000. Proceedings. The Eighth Pacific Conference on*, pages 15–433, 2000.

[22] M. Haindl and J. Filip. *Visual Texture: Accurate Material Appearance Measurement, Representation and Modeling*, chapter Spatially Varying Bidirectional Reflectance Distribution Functions, pages 119–145. Springer London, London, 2013.

[23] H. Hirschmuller and D. Scharstein. Evaluation of cost functions for stereo matching. In *Computer Vision and Pattern Recognition, 2007. CVPR '07. IEEE Conference on*, pages 1–8, June 2007.

[24] B. K.P. Horn. A problem in computer vision: Orienting silicon integrated circuit chips for lead bonding. *Computer Graphics and Image Processing*, 4(3):294 – 303, 1975.

[25] B. K.P. Horn. A problem in computer vision: Orienting silicon integrated circuit chips for lead bonding. *Computer Graphics and Image Processing*, 4(3):294 – 303, 1975.

[26] B.K.P. Horn and K. Ikeuchi. The mechanical manipulation of randomly oriented parts. *Scientific American*, 251(2):100 – 109, August 1984.

[27] P. Laven W. Jarosz F. Seron D. Gutierrez I. Sadeghi, A. Muñoz and H. W. Jensen. Physically-based simulation of rainbows. *ACM Transactions on Graphics (Presented at SIGGRAPH)*, 31(1):3:1–3:12, February 2012.

[28] Y. Qiong I. Sato, T. Okabe and Y. Sato. Shape reconstruction based on similarity in radiance changes under varying illumination. In *Computer Vision, 2007. ICCV 2007. IEEE 11th International Conference on*, pages 1–8, Oct 2007.

[29] K. Ikeuchi. Determining a depth map using a dual photometric stereo. *lnternational Journal of Robotics Research*, 6(1):15 – 31, 1987.

[30] K. Ikeuchi and B. K.P. Horn. Numerical shape from shading and occluding boundaries. *Artificial Intelligence*, 17(1):141 – 184, 1981.

[31] C. M. Herzinger R. Synowicki J. A. Woollam, B. Johs and C. L. Bungay. Overview of variable angle spectroscopic ellipsometry (vase) part 1: Basic theory and typical applications. In *Proc. SPIE CR72 (Optical Metrology)*, pages 3–28, 2000.

[32] S. Fuhrmann J. Ackermann, F. Langguth and M. Goesele. Photometric stereo for outdoor webcams. In *Computer Vision and Pattern Recognition (CVPR), 2012 IEEE Conference on*, pages 262–269, June 2012.

[33] B. V. Funt J. Ho and M. S. Drew. Separating a color signal into illumination and surface reflectance components: theory and applications. *Pattern Analysis and Machine Intelligence, IEEE Transactions on*, 12(10):966–977, Oct 1990.

[34] G. W. Meyer J. S. Gondek and J. G. Newman. Wavelength dependent reflectance functions. In *Proceedings of the 21st Annual Conference on Computer Graphics and Interactive Techniques*, SIGGRAPH '94, pages 213–220, New York, NY, USA, 1994. ACM.

[35] N. N. Zheng J. Sun and H. Y. Shum. Stereo matching using belief propagation. *Pattern Analysis and Machine Intelligence, IEEE Transactions on*, 25(7):787–800, July 2003.

[36] J. Takamatsu R. Sagawa A. Nakazawa R. Kurazume K. Nishino M. Kamakura K. Ikeuchi, T. Oishi and Y. Okamoto. The great buddha project: Digitally archiving, restoring, and analyzing cultural heritage objects. *International Journal of Computer Vision*, 75(1):189–208, 2007.

[37] K. Matsuzawa K. Iwasaki and T. Nishita. Real-time rendering of soap bubbles taking into account light interference. In *Proceedings of the Computer Graphics International*, CGI '04, pages 344–348, Washington, DC, USA, 2004. IEEE Computer Society.

[38] Bram S. K. Nayar K. J. Dana, B. van Ginneken and J. J. Koenderink. Reflectance and texture of real-world surfaces. *ACM Trans. Graph.*, 18(1):1–34, January 1999.

[39] S. Kinoshita. *Structural Colors in Biological Systems - Principle and Applications*. 大阪大学出版会, 2005.

[40] S. Kinoshita. *Structural Colors in the Realm of Nature*. World Scientific, 2008.

[41] S. Kinoshita and S. Yoshioka. Structural colors in nature: the role of regularity and irregularity in the structure. *ChemPhysChem*, 2005.

[42] K. Kitagawa. Transparent film thickness measurement by three-wavelength interference method: An extended application of global model fitting algorithm. In *Mechatronics (MECATRONICS) , 2012 9th France-Japan 7th Europe-Asia Congress on and Research and Education in Mechatronics (REM), 2012 13th Int'l Workshop on*, pages 94–100, Nov 2012.

[43] K. Kitagawa. Thin-film thickness profile measurement by three-wavelength interference color analysis. *Appl. Opt.*, 52(10):1998–2007, Apr 2013.

[44] A. Hertzmann L. Zhang, B. Curless and S. M. Seitz. Shape and motion under varying illumination: unifying structure from motion, photometric stereo, and multiview stereo. In *Computer Vision, 2003. Proceedings. Ninth IEEE International Conference on*, pages 618–625 vol.1, Oct 2003.

[45] J. H. LAMBERT. *Photometria sive de mensura et gradibus luminis, colorum et umbrae*. Augsburg ("Augusta Vindelicorum"), Germany: Eberhardt Klett, 1760.

[46] M. Levoy. The digital michelangelo project. In *in proceedings of SIGGRAPH*, 2000.

[47] B. Curless M. Goesele and S. M. Seitz. Multi-view stereo revisited. In *Computer Vision and Pattern Recognition, 2006 IEEE Computer Society Conference on*, volume 2, pages 2402–2409, 2006.

[48] B. Curless H. Hoppe M. Goesele, N. Snavely and S.M. Seitz. Multi-view stereo for community photo collections. In *Computer Vision, 2007. ICCV 2007. IEEE 11th International Conference on*, pages 1–8, Oct 2007.

[49] J. Lawrence M. Holroyd and T. Zickler. A coaxial optical scanner for synchronous acquisition of 3d geometry and surface reflectance. *ACM Trans. Graph.*, 29(4):99:1–99:12, July 2010.

[50] M. Saeki Y. Manabe K. Chihara M. Imura, O. Oshiro and Y. Yasumuro. A generic real-time rendering approach for structural colors. In *Proceedings of the 16th ACM Symposium on Virtual Reality Software and Technology*, VRST '09, pages 95–102, New York, NY, USA, 2009. ACM.

[51] K. Ikeuchi M. Saito, Y. Sato and H. Kashiwagi. Measurement of surface orientations of transparent objects by use of polarization in highlight. *J. Opt. Soc. Am. A*, 16(9):2286–2293, Sep 1999.

[52] L. T. Maloney and B. A. Wandell. Color constancy: a method for recovering surface spectral reflectance. *J. Opt. Soc. Am. A*, 3(1):29–33, Jan 1986.

[53] K. W. Meinster. Interference spectroscopy. part i. *J. Opt. Soc. Am.*, 31(6):405–426, Jun 1941.

[54] I. D. Reid O. J. Woodford, P. H. S. Torr and A. W. Fitzgibbon. Global stereo reconstruction under second order smoothness priors. In *Computer Vision and Pattern Recognition, 2008. CVPR 2008. IEEE Conference on*, pages 1–8, June 2008.

[55] Y. Ohta and Y. Hayashi. Recovery of illuminant and surface colors from images based on the cie daylight. In *Proceedings of the Third European Conference on Computer Vision (Vol. II)*, ECCV '94, pages 235–246, Secaucus, NJ, USA, 1994. Springer-Verlag New York, Inc.

[56] M. Oren and S. K. Nayar. Generalization of lambert's reflectance model. In *In SIGGRAPH 94*, pages 239–246. ACM Press, 1994.

[57] R. P. Labatut, J. P. Pons and Keriven. Efficient multi-view reconstruction of large-scale scenes using interest points, delaunay triangulation and graph cuts. In *Computer Vision, 2007. ICCV 2007. IEEE 11th International Conference on*, pages 1–8, Oct 2007.

[58] M. Pharr and G. Humphreys. *Physically Based Rendering from Theory to Implementation*. Morgan Kaufmann, 2004.

[59] B. T. Phong. Illumination for computer generated pictures. *Commun. ACM*, 18(6):311–317, June 1975.

[60] R. T. Tan R. Kawakami, H. Zhao and K. Ikeuchi. Camera spectral sensitivity and white balance estimation from sky images. *International Journal of Computer Vision*, 105(3):187–204, 2013.

[61] S. Yoshioka S. Kinoshita and K. Kawagoe. Mechanisms of structural color in the morpho butterfly:cooperation of regularity and irregularity in an iridescent scale. *Proceedings of Royal Society of London B*, 2002.

[62] A. Laskarakis C. Koidis S. Logothetidis, D. Georgiou and N. Kalfagiannis. In-line spectroscopic ellipsometry for the monitoring of the optical properties and quality of roll-to-roll printed nanolayers for organic photovoltaics. *Solar Energy Materials and Solar Cells*, 112:144 – 156, 2013.

[63] A. Chatterjee S. M. Haque and V. M. Govindu. High quality photometric reconstruction using a depth camera. In *Computer Vision and Pattern Recognition (CVPR), 2014 IEEE Conference on*, pages 2283–2290, June 2014.

[64] E. P. F. Lafortune S. R. Marschner, S. H. Westin and K. E. Torrance. Image-based bidirectional reflectance distribution function measurement. *Appl. Opt.*, 39(16):2592–2600, Jun 2000.

[65] E. Nakamura S. Yoshioka and S. Kinoshita. Origin of two-color iridescence in rock dove's feather. *Journal of the Physical Society of Japan*, 2007.

[66] S. M. Seitz and C. R. Dyer. Photorealistic scene reconstruction by voxel coloring. *International Journal of Computer Vision*, 35(2):151–173, 1999.

[67] W. M. Silver. Determining shape and reflectance using multiple images. *Master's thesis Massachusetts Institute of Technology*, 1980.

[68] J. Diebel D. Scharstein S.M. Seitz, B. Curless and R. Szeliski. A comparison and evaluation of multi-view stereo reconstruction algorithms. In *Computer Vision and Pattern Recognition, 2006 IEEE Computer Society Conference on*, volume 1, pages 519–528, June 2006.

[69] Jos Stam. Multiple scattering as a diffusion process. In P. M.Hanrahan and W. Purgathofer, editors, *Rendering Techniques ' 95*, Eurographics, pages 41–50. Springer Vienna, 1995.

[70] P. Bekaert S. B. Oh T. Cuypers, T. Haber and R. Raskar. Reflectance model for diffraction. *ACM Trans. Graph.*, 31(5):122:1–122:11, September 2012.

[71] R. Kawakami T. Morimoto, R. T. Tan and K. Ikeuchi. Estimating optical properties of layered surfaces using the spider model. In *Computer Vision and Pattern Recognition (CVPR), 2010 IEEE Conference on*, pages 207–214, June 2010.

[72] S. Tominaga and B. A. Wandell. Standard surface-reflectance model and illuminant estimation. *JOSA A*, 6(4):576–584, 1989.

[73] K. E. Torrance and E. M. Sparrow. Theory for off-specular reflection from roughened surfaces*. *J. Opt. Soc. Am.*, 57(9):1105–1114, Sep 1967.

[74] P. Labatut V. H. Hiep, R. Keriven and J. P. Pons. Towards high-resolution large-scale multi-view stereo. In *Computer Vision and Pattern Recognition, 2009. CVPR 2009. IEEE Conference on*, pages 1430–1437, June 2009.

[75] G. J. Ward. Measuring and modeling anisotropic reflection. *SIGGRAPH Comput. Graph.*, 26(2):265–272, July 1992.

[76] J. Wassermen. Michelangelo's florence pieta. In *Princeton University press*, 2003.

[77] Y. Wei and L. Quan. Region-based progressive stereo matching. In *Computer Vision and Pattern Recognition, 2004. CVPR 2004. Proceedings of the 2004 IEEE Computer Society Conference on*, volume 1, pages I–106–I–113 Vol.1, June 2004.

[78] L. B. Wolff and T. E. Boult. Constraining object features using a polarization reflectance model. *Pattern Analysis and Machine Intelligence, IEEE Transactions on*, 13(7):635–657, Jul 1991.

[79] R. J. Woodham. Photometric method for determining surface orientation from multiple images. *Optical Engineering*, 19(1):191139–191139–, 1980.

[80] X. Tong J. Snyder Y. Lan M. Ben-Ezra Y. Dong, J. Wang and B. Guo. Manifold bootstrapping for svbrdf capture. *ACM Trans. Graph.*, 29(4):98:1–98:10, July 2010.

[81] S.M. Seitz Y. Furukawa, B. Curless and R. Szeliski. Towards internet-scale multi-view stereo. In *Computer Vision and Pattern Recognition (CVPR), 2010 IEEE Conference on*, pages 1434–1441, June 2010.

[82] K. Sumino Y. Mukaigawa and Y. Yagi. Rapid brdf measurement using an ellipsoidal mirror and a projector. *Information and Media Technologies*, 4(2):451–462, 2009.

[83] Y. Ishii Y. Mukaigawa and T. Shakunaga. Analysis of photometric factors based on photometric linearization. *Journal of Optical Society of America A*, 24(10):3342–3334, 2007.

[84] F. David Fracchia M. S. Drew Y. Sun, Yinlong and T. W. Calvert. Rendering iridescent colors of optical disks. In *Rendering Techniques 2000*, Eurographics, pages 341–352. Springer Vienna, 2000.

[85] T. W. Calvert Y. Sun, F. David Fracchia and M. S. Drew. Deriving spectra from colors and rendering light interference. *IEEE Comput. Graph. Appl.*, 19(4):61–67, July 1999.

[86] B. Wilburn Y. Taguchi and C. L. Zitnick. Stereo reconstruction with mixed pixels using adaptive over-segmentation. In *Computer Vision and Pattern Recognition, 2008. CVPR 2008. IEEE Conference on*, pages 1–8, June 2008.

[87] Md A. Haque T. Nakajima T. Nonoyama X. Li I. Kajiwara J. P. Gong Y. Yue, T. Kurokawa. Mechano-actuated ultrafast full-colour switching in layered photonic hydrogels. *Nature Communications*, 2014.

[88] H. Lin L. Li L. Moreel J. Zhou Q. Du O. Ogbuu S. Danto J. D. Musgraves K. Richardson K. D. Dobson R. Birkmire Y. Zou, D. Zhang and J. Hu. High-performance, high-index-contrast chalcogenide glass photonics on silicon and unconventional non-planar substrates. *Advanced Optical Materials*, 2(5):478–486, 2014.

[89] S. Yoshioka and S. Kinoshita. Effect of macroscopic structure in iridescent color of the peacock feathers. *FORMA*, 2002.

[90] S. Yoshioka and S. Kinoshita. Wavelength-selective and anisotropic light diffusing scale on the wing of the morpho butterfly. *Proceedings of Royal Society of London B*, 2004.

[91] S. Yoshioka and S. Kinoshita. Structural or pigmentary? origin of the distinctive white stripe on the blue wing of a morpho butterfly. *Proceedings of Royal Society of London B*, 2006.

[92] K. Ikeuchi Y.Sato. reflectance and analysis under solar illumination. *Physics-Based Modeling in Computer Vision*, pages 180–187, 1995.

[93] H. Yu. Edge-preserving photometric stereo via depth fusion. In *Proceedings of the 2012 IEEE Conference on Computer Vision and Pattern Recognition (CVPR)*, CVPR '12, pages 2472–2479, Washington, DC, USA, 2012. IEEE Computer Society.

[94] 向川 康博 松下 康之 八木 康史 井下, 智加. 単一散乱の減衰に基づく半透明物体の形状推定 (3 次元画像処理, 多視点画像処理,¡特集¿画像の認識・理解論文). **電子情報通信学会論文誌. *D*, 情報・システム**, 95(8):1598–1608, aug 2012.

[95] 木下修一. **モルフォチョウの碧い輝き**. 化学同人, 2005.

[96] 池内克史、大石岳史. *3* **次元デジタルアーカイブ**. 東京大学出版会, 2010.

[97] 池内 克史 肥後 智昭, 宮崎 大輔. センサフュージョンによる効率的な 3 次元モデルの推定と表現. **映像情報メディア学会誌**, 64(1):112–119, 2010.

[98] 齋藤　彰、米澤賢、村瀬淳一、赤井恵、桑原裕司. 生物に学ぶ特異な構造発色体の開発　～色素フリー・省材料・無退色・高効率・広視野角・単色の発色体～. **光アライアンス**, 2011.

List of Publications

International Conference

1. Yoshie Kobayashi, Tetsuro Morimoto, Imari Sato,Yasuhiro Mukaigawa, Katsushi Ikeuchi,”Reconstructing Shape and Appearance of Thin Film Objects with Hyper Spectral Sensor”, The 12th Asian Conference on Computer Vision (ACCV), 2014 Nov.

Workshop

1. Yoshie Kobayashi, Tetsuro Morimoto, Imari Sato,Yasuhiro Mukaigawa, Katsushi Ikeuchi, ”BRDF Estimation of the Structural Color Object by Using Hyper Spectral Image”, Proc. ICCV workshop of Color and Photometry in Computer Vision, Dec. 2013.

Domestic Conference

1. 小林由枝, 川上玲, 池内克史,”複数の入力スペクトルを用いた対数空間における光源と反射率推定のロバスト化の検証”MIRU,2010 年 7 月

2. Yoshie Kobayashi, Tetsuro Morimoto, Imari Sato,Yasuhiro Mukaigawa, Katsushi Ikeuchi,”Estimating Optical Properties of Thin Film Using Hyper-Spectral Images”, The 17th Meeting on Image Recognition and Understanding Jul. 2014.

3. 小林由枝, 川上玲, 池内克史,”屋外環境の拘束を用いての log 空間における反射率分布と光源の分離”, 情処研報 (CVIM),2010 年 3 月

4. 森本哲郎, 小林由枝, 宮崎大輔, 影沢政隆, 朽津信明, 池内 克史,”桜京古墳における高精細デジタルアーカイブ技術”, 日本文化財科学会，2011 年 6 月

5. 小林由枝, 川上玲, 池内克史,”対数空間における基底関数の線形従属性と推定精度の検証”,MIRU 2011 年 7 月

6. 森本哲郎, 猪瀬健二, 小林由枝, 影沢政隆, 朽津信明, 池内克史,”層状表面分解法による九州装飾古墳の壁画画像解析”, 日本文化財科学会， 2013 年 6 月

7. 小林由枝, 森本哲郎, 佐藤いまり, 向川康博, 池内克史,”薄膜干渉の画像ベース BRDF 推定”, 情処研報 (CVIM),2013 年 9 月

8. 小林由枝, 森本哲郎, 佐藤いまり, 向川康博, 池内克史,”ハイパースペクトル画像を用いた単層膜の BRDF 推定”, 情処研報 (CVIM)，2014 年 3 月

Patent

1. 「薄膜物体の計測装置および計測方法」2014 年 7 月出願済み

2. 「三次元形状計測装置、三次元形状計測方法及び薄膜計測装置」2015 年 5 月出願済み